A Higher-Order Panel Method for Third-Harmonic Diffraction Problems

by

Xuemei Zhu

BS, Electrical Engineering, Hefei University of Technology, 1988
MS, Hydrodynamics, Massachusetts Institute of Technology, 1994

Submitted to the Department of Ocean Engineering
in partial fulfillment of the requirements for the degree of

Doctor of Philosophy in Hydrodynamics

at the

MASSACHUSETTS INSTITUTE OF TECHNOLOGY

February 1997

Author .....
Department of Ocean Engineering
December 18th, 1996

Certified by .....
J. Nicholas Newman
Professor of Naval Architecture
Thesis Supervisor

Accepted by .....
J. Kim Vandiver
Chairman, Departmental Committee on Graduate Students

A Higher-Order Panel Method for Third-Harmonic Diffraction Problems

by

Xuemei Zhu

Submitted to the Department of Ocean Engineering
on December 18^{th}, 1996, in partial fulfillment of the
requirements for the degree of
Doctor of Philosophy in Hydrodynamics

Abstract

Ringing, the high-frequency response of a structure to relatively low-frequency waves, has been a great concern in offshore engineering. To investigate this phenomenon, we solve the third-harmonic diffraction problem using a three-dimensional higher-order panel method in the low-frequency range.

In this thesis, the boundary integral equations are derived from two different theories, based on complementary assumptions. For the long-wave approximation theory, the free surface condition is an inhomogeneous Neumann condition, satisfied on the moving first-order wave elevation. For the conventional perturbation theory, the free surface condition is satisfied on the mean free surface. Based on the long-wave assumption in both theories, the forcing function is assumed to be a localized function, and the contribution from the second-harmonic potential to the third-harmonic forcing function is neglected.

In the first theory, the second- and third-harmonic potentials are of the same order. The Green function $1/r + 1/r'$ is used. The integral equations have different forms for a body with a single column or multiple columns due to different first-order wave elevation. In the second theory, the second- and third-harmonic potentials are of different orders. The free surface Green function is used.

Due to the numerical limitations and the computational effort required in the low-order panel method, a higher-order panel method using B-splines is applied to the nonlinear problems. The geometry and the potential are represented by B-splines. A least-square procedure is used to evaluate the potential on the free surface and the forcing function in B-spline forms.

This thesis includes the numerical results of the second- and third-harmonic potentials and wave loads using the two theories. The results are obtained for a truncated cylinder and an array of four cylinders. The third-harmonic effects are significant in the numerical solutions.

Thesis Supervisor: J. Nicholas Newman
Title: Professor of Naval Architecture

Acknowledgments

I would like to express my greatest gratitude to my advisor, Professor Newman. His guidance and encouragement have motivated me in every way. His unparalleled experience and patience have taught me a great deal about hydrodynamics over the past five years.

I would like to thank my committee members, Professor Faltinsen, Dr. Korsmeyer and Professor Ogilvie, for giving me invaluable advice and suggestions. Working in CHF group has been a pleasant experience, and I really enjoy the friendship from this group. Special thanks to Dr. Lee, who helped me understand WAMIT, to Dr. Maniar, who answered my numerous questions about B-splines, and to Prof. Nielsen, who was on my thesis committee while on sabbatical leave at MIT, and whose constructive comments were very appreciated.

The financial support of this work was provided by the National Science Foundation, Grant 9416096-CTS. Additional support was provided by a Joint Industry Project "Water effects on offshore effects." The sponsors have included the Chevron Petroleum Technology Company, Conoco, David Taylor Research Center, Exxon Production Research Company, Mobil Oil Company, National Research Council of Canada, Norsk Hydro, Offshore Technology Research Center, Petrobras, Saga Petroleum, Shell Development Company, Statoil, and Det Norske Veritas.

Jianghong, who is always singing on our *small road*, is the harbor when I sail to my dreams and the light when my mind is drifted away. Thanks B!

For their love, trust and their own inspiring life, this thesis is dedicated to my parents.

Contents

List of Figures

List of Tables

Chapter 1

Introduction

Predicting the hydrodynamic interactions of ocean waves and floating offshore structures has long been an important subject in ocean engineering. The effective design of such structures depends on the reliable analysis of wave loads and motions. To describe motions and loads accurately, tremendous efforts have been devoted to the development of numerical hydrodynamic analysis. The assumption of ideal flow allows the introduction of a velocity potential, which satisfies the Laplace equation in the entire fluid domain. The wave-body problems can then be described as boundary-value problems, and these problems are usually nonlinear.

A general approach to these problems is the conventional perturbation method. In this scheme, the wave amplitude is assumed to be small, and the characteristic dimensional length of a structure is of the same order as the wavelength. The exact boundary-value problem is reformulated to different orders in the powers of a small parameter, the wave slope.

A boundary integral equation for the potential at each order can be obtained by distributing singularities over the body and on the free surface. Assuming harmonic time dependence, the 'frequency domain' analysis is carried out by an evaluation of motions and responses at a set of wave frequencies [30][11]. By casting the boundary-value problem from the initial state of rest, the 'time domain' analysis is carried out through a time history [5] [39]. The solution in the time domain is analogous to that in the frequency domain by a Fourier transformation.

In many cases, the boundary integral equation is solved numerically, using a three-dimensional panel method. The low-order panel method, also called the constant panel method, has been a commonly used numerical method since the work of Hess and Smith [14]. WAMIT (Wave Analysis MIT), a low-order panel program for the frequency domain analysis, has been developed at MIT during the past ten years [19][33]. This program computes the wave-body interactions for a three-dimensional floating or submerged body of arbitrary geometric form with the use of the free-surface Green function. The body surface, and in some cases the free surface also, is discretized into flat triangular or quadrilateral panels. The potential is assumed to be constant on each panel. Thus, a linear system is set up to be solved for the unknown potential numerically.

Many wave-body interaction problems can be analyzed by the linear potential theory. The potential is decomposed into radiation and diffraction components. The free-surface condition of the first-order potential is a homogeneous condition. Corresponding wave loads and motions are proportional to the amplitudes of incident waves with the same frequencies.

Second-order responses are usually of small magnitude, but are important in certain applications. Wave-drift motions are caused by low-frequency responses[7][10][36]. 'Springing' responses are steady state responses, and are caused by high-frequency excitation, in which the second-order potential is involved [28][35]. The second-order wave effects were summarized by Ogilvie in [40]. Since then, numerical methods to solve for second-order problems have been well established [21],[17], [18],[23]. The free-surface condition for the second-order potential is not homogeneous, and can be interpreted as an oscillatory pressure over the free surface. The main numerical difficulty in calculating the second-order potential is the integration of the slowly-convergent oscillatory forcing over the entire free surface [4] [23]. For structures with large draft, Newman derives [34] that the second-order component rather than the first-order component usually dominates at large depth.

In the past few years, it has been experimentally observed that large offshore platforms can experience resonant motions with frequencies three to five times higher

than the fundamental wave frequencies. The resonant motions occur when waves are steep and wave length is relatively long. This transient resonance, which builds rapidly and decays slowly (Jefferys and Rainey [8]), is analogous to the ringing of a church bell. This phenomenon, which is a serious concern in the field of offshore platform design, is called 'ringing'.

No strong evidence of flow separation and viscous effects has been observed in the ringing experiments by Grue *at el* [9], and so it is possible to use the potential theory to approach this problem. Significant nonlinear effects are indicated by two facts: the frequencies of resonant motions are three to five times higher than the fundamental wave frequencies; and the wave amplitudes are of the same order as the radius of the cylinders. Since the conventional linear and second-order potential theories can not explain ringing, it has been suggested that at least third-order solution is required.

There have been several attempts to predict ringing excitation. The long-wave approximation theory has been developed by Faltinsen, Newman and Vinje [12] ('FNV' hereafter). In this approach, it is assumed that the wave amplitude A and a dimensional length scale of the structure a (the radius of a vertical cylinder in [12]) are of the same order. Both A and a are small, compared to the wavelength. Based on these assumptions, a matched asymptotic expansion method is developed. The second- and third-harmonic time dependence terms are of the same order. The leading-order forcing function on the free surface is confined to the inner domain close to the body. The inhomogeneous Neumann free-surface condition cannot be expanded onto the mean free surface, but is imposed on the horizontal plane which moves up and down with the first-order incident wave elevation. The third-harmonic wave loads are derived analytically for a fixed infinitely deep cylinder in their paper.

Using the conventional perturbation expansion theory, Malenica and Molin [26] ('MM' hereafter) calculate the third-order sum-frequency wave loads for a bottom-mounted cylinder. The free-surface Green function and the potentials of different orders are expressed in terms of Fourier series, thus the third-order results can be computed semi-analytically. Their third-order solution agrees with the FNV's third-harmonic solution when $Ka \leq 0.05$, an unrealistically low-frequency range.

To understand more about ringing, both the long-wave approximation theory and the conventional perturbation theory are further investigated in the present work. The FNV asymptotic expansion applies to an infinitely deep cylinder, whereas the MM analysis is for a bottom-mounted cylinder. In order to provide a numerical tool to solve the third-order problems for a more general structure like a truncated cylinder or tension leg platform (TLP), a numerical method is required. Thus, in this thesis, the boundary integral equations are derived from both theories for the second- and third-harmonic potentials, and the integral equations are solved by a panel method.

We first use the low-order panel method to solve the integral equations, however, the results are affected by the limitations of this method. For example, the derivatives of the potential are required in the evaluation of the forcing function on the free surface. Using this method, the derivatives on the free surface near the waterline intersection cannot be evaluated in a robust way, nor can the derivatives of the second- and third-harmonic potentials on the body close to the waterline. Furthermore, the computational efforts required to solve the nonlinear problem is relatively great.

Following the work in two-dimensions by Hsin *et al* [16], a three-dimensional higher-order panel code based on B-splines has been developed by Maniar [27] to solve linear problems. In this method, the geometry and the unknown potential on the body are both represented by B-spline expansions in parametric space. If the B-spline for the potential is of order k, the potential has $(k-2)$ degrees of continuity everywhere on the body. The integral equation is solved numerically using a Galerkin procedure. For a given accuracy, the computational time is far less than the time required by the low-order panel method. Because of the fundamental numerical limitations of the low-order panel method, this higher-order panel method is adapted to solve the relevant nonlinear problems.

There are two concepts of 'higher-order' that need to be clarified in this thesis. For the numerical solution, the higher-order panel method refers to the degrees of the continuity in terms of approximation of the potential and the geometry. On the other hand, the higher-order potential refers to the order of the perturbation expansion in terms of the dimensional length of the geometry or the corresponding powers of the

wave slope. For the conventional perturbation theory, the potential with magnitude of order A^2 is the second-order potential, and the one with A^3 is the third-order. For the long-wave approximation theory, yet another perturbation method, the potentials with magnitude A^2a and A^3 are of the same third-order. The low- and higher-order panel methods are the different types of the numerical approximations used, whereas first- and higher-order, in other words linear and nonlinear, potentials and wave loads are the linear and the higher-order terms in the perturbation expansion series depending on the defined expansion parameters.

Since the ringing response frequencies are several times higher than the fundamental wave frequencies, we consider only the sum-frequency components in the analysis. This thesis contains the boundary conditions and integral equations of nonlinear diffraction problems in infinitely deep water and the development of numerical methods for these problems.

The exact boundary-value problem is introduced in Chapter 2, and the linear boundary condition and the integral equation are derived. Chapter 3 describes the mathematical formulations of nonlinear potentials and wave loads in the long-wave approximation method. In this method, the free-surface condition is an inhomogeneous Neumann condition and is satisfied on the first-order wave elevation. The Green function is defined to be $1/r + 1/r'$ in the integral equations for the nonlinear potentials. For a body with a single column, the first-order wave elevation is approximated to be a flat surface, so the integral equation does not have the integration over the free surface on the left-hand side. For a body with multiple columns, due to the variation of the first-order wave elevation, the integral equation has an integral over the free surface on both its right-hand side and its left-hand side.

By expanding the irregular waves into a superposition of a number of monochromatic waves with different frequencies, Newman [37] concludes that the leading-order sum-frequency nonlinear loads are due to the sum of the contribution from each individual wave. The interactions between these different waves can be neglected. For irregular waves, each wave spectrum component can be analyzed separately, and the sum-frequency results are the summation of the result from each monochromatic wave

component. Therefore, in this thesis, only monochromatic waves are considered.

Chapter 3 also contains the boundary conditions and integral equations for the second- and third-order problems using the conventional perturbation theory. We are interested in the solutions at the low-frequency range, since ringing happens when waves are relatively long. Thus, we neglect two contributions in the numerical calculation: the far field integration over the free surface, and the second-order potential contribution to the third-order forcing function.

Chapter 4 contains the numerical techniques used to solve the integral equations for nonlinear problems. This chapter presents the basic methodology of the low-order panel method and the higher-order panel method. The fundamental numerical difficulties using the low-order panel method for nonlinear problems are discussed. The procedure to evaluate the B-spline representation for the potential on the free surface and the forcing function is developed. The free surface is truncated at some finite distance away from the body, and the truncation radius is determined numerically.

In Chapter 5, we present the numerical results of the nonlinear potentials and wave loads, most of which are obtained by the higher-order panel method. For the long-wave approximation method, the results are obtained for a truncated cylinder and an array of four cylinders. For a single cylinder, the numerical results are compared with the FNV results, and some difference between the numerical results and the analytical ones are investigated. The explanation of the difference is presented in Appendix C. This chapter also presents the numerical results from the conventional perturbation method for a truncated cylinder. Chapter 6 draws conclusions, discusses some related work, and gives recommendations for further research.

Chapter 2

Basic Formulations

This chapter describes the exact boundary-value problem for the interaction between a floating body and surface waves. The exact boundary conditions can be linearized, and the boundary integral equation for the first-order problem is then presented.

Our interest is to analyze the response of a floating body in the presence of free-surface waves. In practical applications, we assume an irrotational flow without separation, and an incompressible, inviscid fluid. These assumptions allow us to introduce a velocity potential which satisfies the Laplace equation in the entire fluid domain.

In Figure 2-1, Cartesian coordinates are defined, with $z = 0$ on the undisturbed free surface and the z axis pointing upward. A body is fixed without any motion in water of infinite depth, with incoming waves propagating along the $+x$ axis. The presence of the body results in a disturbance to the incident waves. The wave slope KA is assumed to be small, with sinusoidal time dependence, where K is the wavenumber and A the wave amplitude. Actual irregular waves can be described through a linear superposition of sinusoidal components.

Polar coordinates (r, θ, z) are also used, where $re^{i\theta} = x + iy$. The notation for the mean submerged body surface is S_b, the mean free surface is S_f. The unit normal vector $\mathbf{n}$ points out of the flow.

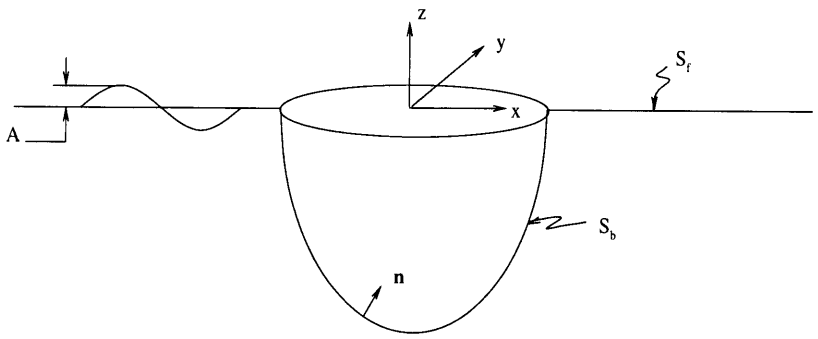

Figure 2-1: Cartesian coordinates for the wave-body interaction problem.

2.1 Exact Boundary-Value Problem

The total diffraction potential is defined as Φ, which satisfies the Laplace equation in the fluid domain,

$$\nabla^2\Phi = 0. \tag{2.1}$$

On the exact free surface, the dynamic boundary condition is obtained from the Bernoulli equation,

$$-\frac{1}{\rho}(p - p_a) = \frac{\partial\Phi}{\partial t} + \frac{1}{2}\nabla\Phi\cdot\nabla\Phi + gz = 0, \tag{2.2}$$

where g is gravity, ρ the fluid density, p the pressure, and p_a is the atmospheric pressure. The derivative of the pressure on the free surface is zero, $Dp/Dt = 0$. Operating on equation (2.2) with the substantial derivative (Newman [30], §3.5),

$$D/Dt = \partial/\partial t + \nabla\Phi\cdot\nabla, \tag{2.3}$$

gives the free surface condition,

$$\frac{\partial^2\Phi}{\partial t^2} + g\frac{\partial\Phi}{\partial z} + 2\nabla\Phi\cdot\nabla\frac{\partial\Phi}{\partial t} + \frac{1}{2}\nabla\Phi\cdot\nabla(\nabla\Phi\cdot\nabla\Phi) = 0. \tag{2.4}$$

The free surface condition (2.4) is nonlinear and is defined on the unknown wave elevation surface $z = \zeta$, which can be evaluated from equation (2.2),

$$\zeta = -\frac{1}{g}(\frac{\partial\Phi}{\partial t} + \frac{1}{2}\nabla\Phi\cdot\nabla\Phi). \tag{2.5}$$

On the submerged part of the body, the normal components of the fluid velocity must be zero for a fixed body, so

$$\frac{\partial\Phi}{\partial n} = 0. \tag{2.6}$$

The total force $\mathbf{F}$ acting on the body can be determined by the integration of the pressure over the submerged part of the body surface. Using the Bernoulli equation (2.2) gives

$$\begin{aligned}\mathbf{F} &= \iint_{S_b} p\mathbf{n}dS \\ &= -\rho\iint_{S_b}(\frac{\partial\Phi}{\partial t} + \frac{1}{2}\nabla\Phi\cdot\nabla\Phi + gz)\mathbf{n}dS.\end{aligned} \tag{2.7}$$

2.2 Linear Diffraction Problem

In the previous section, the exact boundary conditions described are nonlinear and satisfied on the unknown surface, which makes the problem difficult to analyze. With the assumption of small wave slope, $KA = O(\epsilon)$, the total potential can be expanded in powers of the small parameter ϵ.

For an infinitely deep fluid, the first-order incident wave Φ_I propagating along the $+x$ axis is defined as

$$\Phi_I = Re\{(\frac{gA}{\omega})e^{(Kz-iKx+i\omega t)}\}$$

$$= Re\{\phi_I e^{i\omega t}\}, \tag{2.8}$$

where ω is the wave frequency, and x and z are the horizontal and vertical positions of a point in the fluid. The dispersion relation in an infinitely deep fluid is

$$K = \omega^2/g. \tag{2.9}$$

The diffraction potential for a fixed body is expressed as the sum of the first-order diffraction potential $\Phi^{(1)}$ and the higher order terms

$$\begin{aligned} \Phi(\mathbf{x},t) &= \Phi^{(1)}(\mathbf{x},t) + O(\epsilon^2) \\ &= Re\{\phi^{(1)}(\mathbf{x})e^{i\omega t}\} + O(\epsilon^2) \\ &= Re\{[\phi_s^{(1)}(\mathbf{x}) + \phi_I(\mathbf{x})]e^{i\omega t}\} + O(\epsilon^2) \end{aligned} \tag{2.10}$$

where $\phi_s^{(1)}$ is the first-order scattering potential, which is the result of the disturbance of incident waves by the fixed body. The first-order diffraction potential is the sum of the scattering and the incident potentials. The symbol O denotes the magnitude of the higher-order terms.

Keeping the first-order terms in equation (2.4), the linearized free surface condition is

$$-K\phi^{(1)} + \frac{\partial \phi^{(1)}}{\partial z} = 0, \quad \text{on } S_f, \tag{2.11}$$

where the free surface condition is imposed on the mean free surface by the linearization. The scattering potential $\phi_s^{(1)}$ satisfies the radiation condition in the far field,

$$\phi_s^{(1)} \propto \frac{e^{-iKR}}{\sqrt{R}}, \quad R \to \infty, \tag{2.12}$$

where $R = \sqrt{x^2 + z^2}$, and $\phi_s^{(1)}$ decays to zero as $z \to -\infty$. From equation (2.5), the

first-order wave elevation is

$$\begin{aligned} \zeta^{(1)} &= -\frac{1}{g}\frac{\partial \Phi^{(1)}}{\partial t} \\ &= Re\{-\frac{i\omega}{g}\phi^{(1)}e^{(i\omega t)}\}. \end{aligned} \tag{2.13}$$

The body boundary condition for $\phi^{(1)}$ is satisfied on the mean submerged body surface. That is

$$\frac{\partial \phi^{(1)}}{\partial n} = 0, \quad \text{on } S_b, \tag{2.14}$$

or alternatively

$$\frac{\partial \phi_s^{(1)}}{\partial n} = -\frac{\partial \phi_I}{\partial n}, \quad \text{on } S_b. \tag{2.15}$$

The first-order boundary-value problem described above can be analyzed in a closed form in only a few cases. For most practical problems, a numerical method is required.

The boundary-value problem can be recast as a boundary integral equation to solve for the unknown potential. The free surface Green function G is used, in the form derived by Wehausen and Laitone [44],

$$G(\mathbf{x},\xi) = \frac{1}{r} + \frac{1}{r'} + \frac{2K}{\pi}\int_0^\infty dk \frac{e^{k(z+\varsigma)}}{k-K} J_0(kR), \tag{2.16}$$

where J_0 is the Bessel function of the zeroth order. $\mathbf{x} = (x, y, z)$ is the source point, while $\xi = (\xi, \eta, \zeta)$ is the field point. And

$$\begin{aligned} r^2 &= R^2 + (z-\zeta)^2, \\ r'^2 &= R^2 + (z+\zeta)^2, \\ R^2 &= (x-\xi)^2 + (y-\eta)^2. \end{aligned}$$

This function satisfies the first-order free surface condition and the far-field radiation condition. The first two terms in the Green function, $1/r + 1/r'$, are called the Rankine

part, and the integral is called the wave part.

In the vicinity where the source point and field point coincide on the free surface, the free surface Green function has a logarithmic singularity ([31]),

$$G(\mathbf{x},\xi) = \frac{1}{r} + \frac{1}{r'} - 2K\log(r' + |z+\zeta|) + O(1). \tag{2.17}$$

From the free-surface Green function, Green's theorem leads to the integral equation for $\phi_s^{(1)}$ on the body,

$$\begin{aligned} 2\pi\phi_s^{(1)}(\mathbf{x}) + \iint_{S_b} \phi_s^{(1)}(\mathbf{x})\frac{\partial G(\mathbf{x},\xi)}{\partial n}dS &= \iint_{S_b} \frac{\partial \phi_s^{(1)}(\mathbf{x})}{\partial n} G(\mathbf{x},\xi)dS \\ &= -\iint_{S_b} \frac{\partial \phi_I(\mathbf{x})}{\partial n} G(\mathbf{x},\xi)dS. \end{aligned} \tag{2.18}$$

Alternatively, the integral equation can be rewritten for the diffraction potential $\phi^{(1)}$ (Newman and Sclavounos [33], Korsmeyer *at el* [19])

$$2\pi\phi^{(1)}(\mathbf{x}) + \iint_{S_b} \phi^{(1)}(\mathbf{x})\frac{\partial G(\mathbf{x},\xi)}{\partial n}dS = 4\pi\phi_I(\mathbf{x}). \tag{2.19}$$

We use equation (2.19) to solve the diffraction problem to take the advantage of a simpler right-hand side. For a given source point and field point, the integral of the Green function and its derivatives can be obtained. Also, the right-hand side of (2.19) is a known function. The only unknown in the integral equation is the potential on the body, and the unknown can be solved for numerically by the methods described in Chapter 3. After the potential on the body is obtained, the potential in the fluid can be computed in the following form,

$$\phi^{(1)}(\mathbf{x}) = \phi_I(\mathbf{x}) - \frac{1}{4\pi}\iint_{S_b} \phi^{(1)}(\xi)\frac{\partial G(\mathbf{x},\xi)}{\partial n}dS. \tag{2.20}$$

For the low-order panel method discussed in Chapter 3, the source formulation is used to obtain the velocities on the body and in the fluid. The source formulation for the linear problem is presented in Appendix A.1.

Chapter 3

Formulations of Nonlinear Problems

This chapter discusses the boundary conditions and the integral equations for nonlinear potentials based on two different theories: the long-wave approximation theory and the conventional perturbation theory. Complete nonlinear solutions contain a variety of frequency components. Our concentration is in the regime where the response frequencies are several times higher than the fundamental frequencies, so we only consider the sum-frequency components in our analysis. For irregular waves, Newman [37] concludes that the leading-order contribution for sum-frequency components is the sum of each individual monochromatic wave. Since only sum-frequency components are considered in this thesis, the integral equation can be solved at each wave spectrum component. Therefore, we consider monochromatic waves. Thus, the nonlinear potentials and wave loads included in this thesis are sum-frequency components, specifically the second- and third-harmonics. In addition, the formulations for the nonlinear wave loads and the results obtained later in this thesis are the horizontal forces acting on the body.

Nonlinear diffraction potentials can be decomposed into incident and scattering parts. The former component persists over the far-field, while the later satisfies a suitable condition which ensures that this disturbance is due to the body, and that it tends to zero in the far field. In general, these two potentials are solved separately

due to their different far-field behaviors. However, the second- and third-harmonic incident potentials vanish in infinitely deep water for monochromatic waves (see §3.4). Therefore, these nonlinear diffraction potentials only contain scattering components, and it is not necessary to distinguish the diffraction and scattering components in formulations and calculations.

3.1 Long-Wave Approximation

In this theory, it is assumed that the wave amplitude A is comparable to a, the dimensional length of the cross section of a vertical structure. We consider a body either with a single column or with multiple columns, such as a vertical cylinder or a TLP, so a can be the radius of a cylinder. It is also assumed that the wave amplitude is small compared to the wave length. Thus,

$$A = O(a), \tag{3.1}$$

$$KA = O(\epsilon), \quad Ka = O(\epsilon), \tag{3.2}$$

where K is the wavenumber, and ϵ is a small parameter.

Figure 3-1 shows the relative magnitude of each parameter defined in this theory. In the figure, the radius of the cylinder is small compared to λ, the wavelength of the incoming wave. The radius of the cylinder is comparable to the wave amplitude, and is small compared to T, the draft of the cylinder. A matched asymptotic expansion developed by FNV based on these two assumptions is adopted in the analysis of this thesis.

In this long-wave regime, the boundary-value problem can be described in the *inner domain* and *outer domain* separately (Newman [30] chapter 7, Faltinsen *et al* [12] §3). In the inner domain close to the body, the length scale is comparable to a, the only relevant parameter in the inner domain; in the outer domain away from the body, the length scale is comparable to the wavelength λ, and the nonlinear effects vanish in this domain, which will be discussed in this chapter. The draft of the

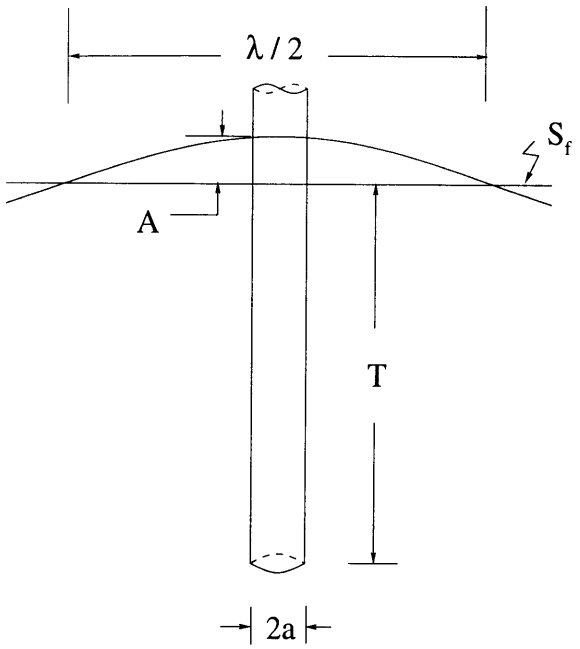

Figure 3-1: The wave-body profile in the long-wave approximation regime.

cylinder is not a relevant length here, since the draft is much larger than the radius.

3.1.1 First-Order Wave Elevation

The normal derivative of the diffraction potential vanishes on the body, so in the inner domain, $\partial\phi_s^{(1)}/\partial r = O(\partial\phi_I^{(1)}/\partial r)$. From equation (2.8), $\partial\phi_I^{(1)}/\partial r \propto \omega A$, thus $\partial\phi_s^{(1)}/\partial r \propto \omega A$. The only parameter in the inner domain is a, so the gradient of the scattering potential must be proportional to $1/a$. The corresponding scattering potential must be of order ωAa, and one order smaller than the incident potential.

From equation (2.13), the first-order free-surface elevation is proportional to the first-order diffraction potential. The scattering potential is one order smaller than the incident potential in the inner domain, therefore, the leading-order wave elevation $Z^{(1)}$ can be approximated as

$$\begin{aligned} Z^{(1)} &= -\frac{1}{g} Re\{\frac{\partial \Phi_I}{\partial t}\}_{z=0} \\ &= Re\{-iAe^{-iKx}e^{i\omega t}\} \\ &= Re\{\zeta^{(1)}e^{i\omega t}\}, \end{aligned} \tag{3.3}$$

where $\zeta^{(1)} = -iAe^{-iKx}$. For a single cylinder, in the inner domain, $Kx < O(1)$ and $e^{-iKx} \simeq 1$, so the above equation can be approximated as

$$Z^{(1)} \simeq Re\{-iAe^{i\omega t}\} = A\sin(\omega t). \tag{3.4}$$

For a cylinder, the first-order wave elevation in the inner domain can be approximated as a horizontal surface which moves up and down with time. This horizontal surface is referred to as the first-order wave elevation plane, where the free-surface condition is satisfied for a single cylinder later in this Chapter.

3.1.2 Exact Boundary Conditions

The nonlinear potential up to the third-order is defined to be ψ. The total potential Φ is the sum of the first-order diffraction potential $\Phi^{(1)}$ and ψ,

$$\Phi = \Phi^{(1)} + \psi(\mathbf{x}, t) + O(\epsilon^4). \tag{3.5}$$

By substituting the above equation into equations (2.6) and (2.4), and invoking the first-order boundary condition equations (2.15) and (2.11), the leading order boundary conditions for ψ are

$$\psi_n = 0, \quad \text{on } S_b, \tag{3.6}$$

$$\psi_{tt} + g\psi_z = -\nabla\Phi^{(1)} \cdot \nabla\Phi_t^{(1)} - \frac{1}{2}\nabla\Phi^{(1)} \cdot \nabla(\nabla\Phi^{(1)})^2, \quad \text{on } z = Z. \tag{3.7}$$

The magnitudes of the right-hand side terms in equation (3.7) can be estimated. In the inner domain, from §3.1.1, $\phi_s^{(1)} \propto \omega Aa$. In the far-field, the first-order scattering potential satisfies the radiation condition in equation (2.12). For the scattering potential, the far-field expansion and the inner expansion can be matched in the region that is far from the body in the inner domain but close to the body in the outer domain.

From the FNV analysis, $\partial\phi_s^{(1)}/\partial r \propto \omega Aa^2/r$ in the inner domain. Therefore,

on the right-hand side of (3.7), the leading order of the forcing function is proportional to several inverse powers of the radial coordinate in the inner domain, e.g. $1/r^2, a/r^3, a^2/r^4, \cdots$ etc.. Thus the forcing function can be neglected with increasing radial distance along the free surface. It should also be noted that on the right hand side of equation (3.7), the magnitude of the first term is proportional to A^2a, with second-harmonic time dependence; and the magnitude of the second term is proportional to A^3, with third-harmonic time dependence.

The forcing function tends to zero with increasing radial distance r on the free surface, and the contribution is of a higher order in the outer domain where $Kr = O(1)$. Thus, the forcing function is confined in the inner domain. Nonlinear effects exist in the inner domain close to the body, and the outer domain is governed by the linear theory.

In this theory, we refer to the order of long-wave approximation theory in terms of wave amplitude and dimensional length of the body. From equation (3.7), the nonlinear potential ψ contains a component of order A^2a with second-harmonic time dependence, and a component of order A^3 with third-harmonic time dependence. Both components are of the same order based on the long-wave approximation assumptions.

3.1.3 Simplified Free Surface Condition

Since the forcing function is only significant in the inner domain, for a single cylinder we define the same inner coordinates as FNV,

$$R = r/a, \quad Z = (-z + Z^{(1)})/a, \tag{3.8}$$

where $Z^{(1)} = A \sin \omega t$. The horizontal plane $Z(t) = 0$ coincides with the instantaneous first-order wave elevation at the intersection of the incident wave with the body axis. Z is positive in the fluid. On the side of the cylinder, $R = 1$. Both R and Z are

normalized coordinates. The corresponding inner nonlinear potential Ψ is

$$\Psi(R,\theta,Z) \equiv \psi(r,\theta,z). \tag{3.9}$$

In the inner domain,

$$(\Psi_R, \frac{1}{R}\Psi_\theta, \Psi_Z) = O(\Psi). \tag{3.10}$$

By substituting the inner coordinates (3.8) into the free-surface condition (3.7), and using the relation

$$\begin{aligned} \frac{d}{dt} &= \frac{\partial}{\partial t} + \frac{\partial}{\partial Z}\frac{\partial Z}{\partial t} \\ &= \frac{\partial}{\partial t} + \frac{1}{a}\frac{\partial Z^{(1)}}{\partial t}\frac{\partial}{\partial Z}, \end{aligned} \tag{3.11}$$

the corresponding inner free-surface condition can be obtained (equation (3.8) in FNV)

$$\begin{aligned} &\frac{a}{g}\Psi_{tt} + 2\frac{\omega A}{g}\cos\omega t\Psi_{Zt} - KA\sin\omega t\Psi_Z + KA\frac{A}{a}\Psi_{ZZ} - \Psi_Z \\ &\qquad = \frac{g}{a}(-\nabla\Phi^{(1)}\cdot\nabla\Phi_t^{(1)} - \frac{1}{2}\nabla\Phi^{(1)}\cdot\nabla(\nabla\Phi^{(1)})^2). \end{aligned} \tag{3.12}$$

In the inner domain,

$$\frac{a}{g}\Psi_{tt} = (Ka)\Psi, \quad \frac{\omega A}{g}\Psi_{Zt} = (Ka)\Psi_Z. \tag{3.13}$$

Therefore, on the left-hand side of equation (3.12), the coefficients of the first four terms are one order smaller than the coefficient of the last term. We neglect the first four terms on the left-hand side, so the inner free-surface condition becomes

$$\begin{aligned} \Psi_Z &= -\frac{g}{a}(-\nabla\Phi^{(1)}\cdot\nabla\Phi_t^{(1)} - \frac{1}{2}\nabla\Phi^{(1)}\cdot\nabla(\nabla\Phi^{(1)})^2) \\ &= f(\mathbf{x},t). \end{aligned} \tag{3.14}$$

The right-hand side of equation (3.14) can be evaluated on the mean free surface, the $z = 0$ plane. But the above free-surface condition is satisfied on the exact, unknown free surface. Using a Taylor expansion in powers of the small parameter ϵ, the free-surface condition can be expanded to some known surface. A simple, logical expansion would be to expand the exact free surface to the mean free surface $z = 0$,

$$\Psi_Z(R,\theta,Z) = \Psi_Z(R,\theta,0) + Z(\frac{\partial \Psi_Z}{\partial z})_{z=0} + \frac{1}{2}Z^2(\frac{\partial^2 \Psi_Z}{\partial z^2})_{z=0} + \cdots. \qquad (3.15)$$

However, according to the analysis of FNV, the vertical derivative of Ψ with respect to z is amplified by order $1/a$ in the inner domain, so $\Psi_{Zz} \propto \Psi_{ZZ}/a$. On the other hand, $\Psi_{ZZ} = O(\Psi)$, $\Psi_Z = O(\Psi)$. $Z = O(A)$, so $Z\partial\Psi_Z/\partial z = O(A/a)\Psi_Z$, and $Z^2\partial\Psi_z/\partial^2 z = O(A/a)^2\Psi_Z$, so the second and third terms are of the same order as the first term, since $A/a = O(1)$. Using the same analysis, all terms in this series are of the same order, therefore, the Taylor series in equation (3.15) does not converge. The free-surface condition in equation (3.14) cannot be expanded onto the mean free surface.

Alternatively, following the FNV analysis, Ψ_Z can be expanded onto the first-order wave elevation plane,

$$\begin{aligned} \Psi_Z(R,\theta,Z) &= \Psi_Z(R,\theta,Z^{(1)}) \\ &+ (Z - Z^{(1)})(\frac{\partial \Psi_Z}{\partial z})_{z=Z^{(1)}} + \frac{1}{2}(Z - Z^{(1)})^2(\frac{\partial^2 \Psi_Z}{\partial z^2})_{z=Z^{(1)}} + \cdots \qquad (3.16) \end{aligned}$$

Considering the first-order wave elevation plane, $Z^{(1)} = O(\epsilon)$, and $Z - Z^{(1)} = O(\epsilon^2)$, so $(Z - Z^{(1)})\Psi_{Zz} = O(\epsilon)\Psi_Z$, and $(Z - Z^{(1)})^2\Psi_{Zzz} = O(\epsilon^2)\Psi_Z$. The order of each following term in this series is increased by ϵ, thus the Taylor series in equation (3.16) converges. Keeping the leading-order term of the above Taylor series, we have

$$\begin{aligned} \Psi_Z &= -\frac{g}{a}(-\nabla\Phi^{(1)} \cdot \nabla\Phi_t^{(1)} - \frac{1}{2}\nabla\Phi^{(1)} \cdot \nabla(\nabla\Phi^{(1)})^2) \\ &= f(\mathbf{x},t), \qquad \text{on } z = Z^{(1)}. \qquad (3.17) \end{aligned}$$

The free-surface condition for Ψ is satisfied on the first-order wave elevation, the

horizontal plane defined in equation (3.4), and the forcing function is evaluated on the mean free surface.

The body boundary condition for a truncated cylinder is the same as equation (3.6), and the condition is satisfied on the submerged body surface under the first-order wave elevation. Hence, the boundary condition for Ψ is an inhomogeneous Neumann condition on the free surface $Z = 0$, and a homogeneous Neumann condition on the body.

3.1.4 Integral Equations

The boundary-value problem described above can be recast as an integral equation for the nonlinear potential Ψ on the body with the use of Green's theorem. We define the Green function as

$$G(\mathbf{x}, \xi, t) = \frac{1}{r} + \frac{1}{r'}, \tag{3.18}$$

and

$$r^2 = R^2 + (Z^{(1)} - \zeta)^2,$$
$$r'^2 = R^2 + (Z^{(1)} + \zeta)^2,$$

where R is defined in equation (2.16), and $Z^{(1)}$ is defined in equation (3.3). The image source is above the $Z^{(1)} = 0$ plane, different from the usual image source defined above the $z = 0$ plane in equation (2.16).

Applying Green's Theorem, the boundary integral equation for Ψ is

$$2\pi\Psi(\mathbf{x}, t) + \iint_{S_b(t)} \Psi(\xi, t) \frac{\partial G(\mathbf{x}, \xi, t)}{\partial n} dS = \iint_{S_Z(t)} f(\xi, t) G(\mathbf{x}, \xi, t) dS, \tag{3.19}$$

where $S_b(t)$ is the submerged body surface below $Z = 0$, and S_Z is the moving inner free surface $\zeta^{(1)}$. There is no integral over the free surface on the left side, since the normal derivative of $1/r$ and its image $1/r'$ cancel each other on the free surface. Due to the vanishing diffraction body condition, there is no integral over the body

surface on the right-hand side either. There is no integral over the infinite, since the derivative of te Green function and the forcing function vanish.

It appears that equation (3.19) should be solved in the time domain, since the free surface and the submerged body surface change with time for irregular waves. As mentioned earlier in this chapter, the solution will be obtained for each given wavenumber. For a given wave frequency, the first-order wave elevation as well as the submerged body surface are periodic. Therefore, the integral equation should be solved at different time steps within one wave period, and the body surface and the free surface in equation (3.19) should be the instantaneous surfaces of that time.

Since the integral equation (3.19) is solved at a set of frequencies, the forcing function and the unknown potential can be separated into second- and third-harmonic components,

$$\begin{aligned} f(\mathbf{x},t) &= Re\{f^{(2)}(\mathbf{x})e^{2i\omega t} + f^{(3)}(\mathbf{x})e^{3i\omega t}\}, \\ \Psi(\mathbf{x},t) &= Re\{\Psi^{(2)}(\mathbf{x},t)e^{2i\omega t} + \Psi^{(3)}(\mathbf{x},t)e^{3i\omega t}\}. \end{aligned} \tag{3.20}$$

$\Psi^{(2)}(\mathbf{x},t)$ and $\Psi^{(3)}(\mathbf{x},t)$ do not have harmonic time dependence, but these two potentials change with time within each given wave period due to the changing surfaces in the integral equation (3.19). The forcing function is evaluated on the mean free surface, and this function is the same all the time for a given wave period. According to the right-hand side of equation (3.17), we have

$$f^{(2)} = \frac{i\omega g}{2a}\nabla\phi^{(1)} \cdot \nabla\phi^{(1)}, \tag{3.21}$$

$$f^{(3)} = \frac{g}{8a}\nabla\phi^{(1)} \cdot \nabla(\nabla\phi^{(1)})^2. \tag{3.22}$$

Thus, instead of solving the integral equation (3.19), the second- and third-harmonic potentials are solved respectively,

$$2\pi\Psi^{(j)}(\mathbf{x},t) + \iint_{S_b(t)} \Psi^{(j)}(\mathbf{x},t)\frac{\partial G(\mathbf{x},\xi,t)}{\partial n}dS = \iint_{S_Z(t)} f^{(j)}(\xi)G(\mathbf{x},\xi,t)dS \tag{3.23}$$

where $j = 2, 3$.

In Appendix A.2, the source formulation for the nonlinear potentials is derived. This source formulation is used to obtain the derivatives of the nonlinear potentials in the low-order panel method in order to avoid the double derivatives of the Green function.

3.1.5 Formulations for a Body with Multiple Columns

For a body with multiple columns, such as an array of cylinders or a TLP, the formulations are different from those in the single cylinder case.

For a single cylinder, as discussed in §3.1.1, the inner domain close to the body can be approximated by a flat plane, since $Kx < O(1)$ in that region. For a body with multiple columns, the inner free surface could be divided into several local free surfaces. Each local free surface includes the waterline of one column. This local free surface can still be approximated as a flat plane, the intersection of the free surface with one column. However, due to the distances between these columns, the intersections of the free surface with different columns have different vertical displacement. Therefore, the complete inner free surface is not continuous at adjoining local free surfaces.

We define the inner free surface to include all the waterlines of the body. The inner free surface can not be approximated by a flat plane due to the distance between the columns, since the distance might be large or small compared to the wavelength. Therefore, the Kx term in equation (3.3) cannot be neglected as in a single cylinder case. The inner free surface for the body with multiple columns has a small wave slope defined in equation (3.3). The inner normal coordinates are defined as follows:

$$R = r/a, \quad Z = (-z + A\sin(\omega t - Kx))/a. \tag{3.24}$$

Using the same algebra as for the single cylinder case, we can obtain the same inhomogeneous free-surface condition as described in equation (3.17), but the free-surface condition is satisfied on the $Z = 0$ surface defined in equation (3.24) instead. Therefore, the free-surface condition for a body with multiple columns is also an

inhomogeneous Neumann condition satisfied on the first-order wave elevation, while the forcing function is evaluated on the mean free surface. The body boundary condition is a homogeneous condition.

Applying Green's theorem to the nonlinear potentials $\Psi^{(2)}$ and $\Psi^{(3)}$, the integral equations are derived

$$\begin{aligned}
2\pi\Psi^{(j)}(\mathbf{x},t) &+ \iint_{S_b(t)+S_Z(t)} \Psi^{(j)}(\xi,t)\frac{\partial G(\mathbf{x},\xi,t)}{\partial n}dS \\
&= \iint_{S_Z(t)} f^{(j)}(\xi)G(\mathbf{x},\xi,t)dS, \qquad \mathbf{x}\in S_b(t), \\
4\pi\Psi^{(j)}(\mathbf{x},t) &+ \iint_{S_b(t)+S_Z(t)} \Psi^{(j)}(\mathbf{x},t)\frac{\partial G(\mathbf{x},\xi,t)}{\partial n}dS \\
&= \iint_{S_Z(t)} f^{(j)}(\xi)G(\mathbf{x},\xi,t)dS, \qquad \mathbf{x}\in S_Z(t), \qquad (3.25)
\end{aligned}$$

where $j = 2, 3$. There is an integral over the free surface on the left-hand side of equation (3.25), since $\partial G/\partial n \neq 0$ on $S_Z(t)$ due to the non-flat free surface. A 4π factor in the second equation above is due to the integral of the normal derivative of both $1/r$ and its image $1/r'$ on the free surface, which are singular and have the same sign when $\mathbf{x}$ approaches ξ on $S_Z(t)$ ([46]).

3.1.6 Nonlinear Wave Loads

The horizontal sum-frequency wave loads F acting on the body due to the nonlinear potential Ψ can be obtained by integrating the pressure over the body surface,

$$\begin{aligned}
F &= -\rho\iint_{S_b(t)}(\frac{\partial\Psi}{\partial t} + \nabla\Psi\cdot\nabla\Phi^{(1)})n_x ds \\
&= -\rho\iint_{S_b(t)}(\frac{\partial\Psi}{\partial t} + \frac{1}{a}\frac{\partial Z^{(1)}}{\partial t}\frac{\partial\Psi}{\partial Z} + \nabla\Psi\cdot\nabla\Phi^{(1)})n_x ds \\
&= Re\{F^{(2)}e^{2i\omega t} + F^{(3)}e^{3i\omega t} + F^{(4)}e^{4i\omega t}\} \qquad (3.26)
\end{aligned}$$

where $F^{(2)}, F^{(3)}, F^{(4)}$ are the coefficients of the second-, third-, and fourth-harmonic components.

Upon obtaining $\Psi^{(2)}$, $\Psi^{(3)}$, and their gradients, the nonlinear wave loads for each

order can be computed,

$$F^{(2)} = -2i\rho\omega \iint_{S_b(t)} \Psi^{(2)} n_x ds, \tag{3.27}$$

$$\begin{aligned} F^{(3)} &= -\rho \iint_{S_b(t)} (3i\omega\Psi^{(3)} + \frac{i\omega}{2a}\zeta^{(1)}\frac{\partial\Psi^{(2)}}{\partial Z} + \frac{1}{2}\nabla\Psi^{(2)} \cdot \nabla\phi^{(1)}) n_x ds, \\ &= F_3^{(3)} + F_{21}^{(3)} + F_{22}^{(3)}, \end{aligned} \tag{3.28}$$

$$F^{(4)} = -\rho \iint_{S_b(t)} (\frac{i\omega}{2a}\zeta^{(1)}\frac{\partial\Psi^{(3)}}{\partial Z} + \frac{1}{2}\nabla\Psi^{(3)} \cdot \nabla\phi^{(1)}) n_x ds. \tag{3.29}$$

where $\zeta^{(1)} = -iA$, or $\zeta^{(1)} = -iAe^{-iKx}$ depending on whether the body consists of a single column or multiple columns. In equation (3.28), $F_2^{(3)}$ is the third-harmonic force due to the second-harmonic potential. $F_3^{(3)}$ is the third-harmonic force due to the third-harmonic potential. $F^{(4)}$ denotes the fourth-harmonic force due to the third-harmonic potential.

3.1.7 Analysis of FNV

In FNV, Ψ is obtained analytically by using the matched asymptotic method for the infinitely deep cylinder with long-waves. In equation (3.14) of their paper, Ψ is expressed in a Fourier series,

$$\Psi = \sum_{m=0}^{3} c_m(t)\Psi_m(R, Z)\cos m\theta, \tag{3.30}$$

where $c_0 = c_2 = \omega K A^2 a \sin 2\omega t$, and $c_1 = c_3 = \omega K A^3 \sin^3 \omega t$. $\sin^3 \omega t = \frac{1}{4}(3\sin\omega t - \sin 3\omega t)$. There are four Fourier components in the FNV analysis: two second-harmonic terms of order $A^2 a$, and two third-harmonic terms of order A^3.

For the infinitely deep cylinder, the normal in the x direction is $-\cos\theta$, so $\int\int_{s_b} n_x ds = -\int_0^{2\pi} \cos\theta d\theta \int_{-\infty}^{\zeta^{(1)}} dz$. Since the second-harmonic time dependence terms of Ψ have zero contribution to integral equation (3.27), that is, $F^{(2)} = 0$. In reference to the numerical results in Chapter 5, we define

$$F_2^{(3)} = F_{21}^{(3)} + F_{22}^{(3)}, \tag{3.31}$$

where $F_{21}^{(3)}$ comes from the contribution of the second term on the right-hand integral in equation (3.28), and $F_{21}^{(3)} = 0$ in the FNV analysis. $F_{22}^{(3)}$ coems from the contribution of the third term. The contribution from the integrals of the first and third terms in equation (3.28) are the same, and

$$F_2^{(3)} = F_3^{(3)} = -\frac{1}{2}\pi\rho g K^2 a^2 A^3 \tag{3.32}$$

Also, in the FNV analysis, $F^{(4)} = 0$ due to the cancelation of the first and second terms in equation (3.29).

3.2 Conventional Perturbation Expansion

In the conventional perturbation expansion, the wave amplitude A is assumed to be one order smaller than the dimensional length a of a body. The wavelength λ is the same order as a. Thus

$$KA = O(\epsilon), \quad Ka = O(1). \tag{3.33}$$

Figure 3-2 shows the relative magnitude of each parameter defined. The radius of the body is of the same order as the wavelength of the incoming wave, λ. The wave amplitude is small compared to the cross section of the structure. The draft of the cylinder is not a relevant parameter in this analysis.

In this regime, the boundary-value problem is reformulated into powers of wave slope, the small parameter ϵ. Due to the above assumptions, the nonlinear potential with magnitudes A^2a and A^3 are of different orders, which is different from the analysis in the long-wave approximation theory. The potential with magnitude A^2a is the second-order quantity, and the component with magnitude A^3 is the third-order quantity.

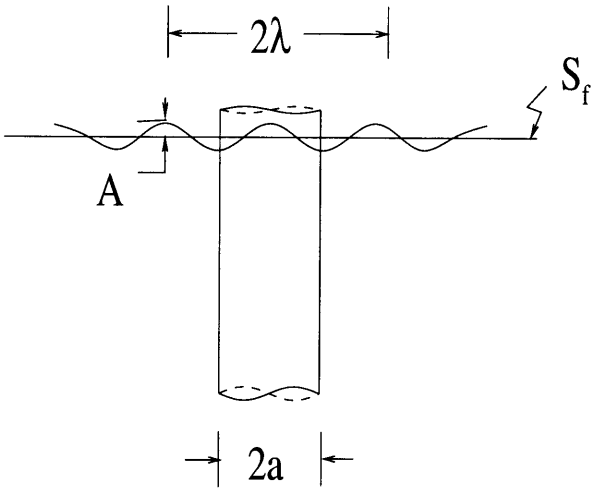

Figure 3-2: The wave-body profile in the conventional perturbation regime.

3.2.1 Boundary Conditions for Nonlinear Potentials

In the conventional perturbation theory, the total potential Φ can be expanded as the sum of the potentials of different orders,

$$\begin{aligned}\phi &= \Phi^{(1)} + \Phi^{(2)} + \Phi^{(3)} + O(\epsilon^4) \\ &= Re\{\phi^{(1)}e^{i\omega t} + \phi^{(2)}e^{2i\omega t} + \phi^{(3)}e^{3i\omega t} \\ &\quad +\bar{\phi}^{(2)} + \bar{\phi}^{(3)}e^{i\omega t}\} + O(\epsilon^4),\end{aligned} \tag{3.34}$$

where $\phi^{(2)}, \phi^{(3)}$ are the second- and third-order sum-frequency diffraction potentials, and $\bar{\phi}^{(2)}, \bar{\phi}^{(3)}$ are the second- and third-order difference-frequency diffraction potentials. Our objective is to solve for the sum-frequency components, $\phi^{(2)}$ and $\phi^{(3)}$.

Using the Taylor expansion, the complete free-surface condition can be expanded onto the mean free surface $z = 0$ (Newman [30], §6.4). By keeping the second-order

terms in equation (2.4), the free-surface condition for the second-order potential is

$$\begin{aligned} -4K\phi^{(2)} + \phi_z^{(2)} &= -\frac{i\omega}{g}\nabla\phi^{(1)} \cdot \nabla\phi^{(1)} + \frac{i\omega}{2g}\phi^{(1)}(-K\phi_z^{(1)} + \phi_{zz}^{(1)}), \\ &= q^{(2)}, \end{aligned} \tag{3.35}$$

where $q^{(2)}$ is the notation for the second-order forcing function. By keeping the third-order terms in equation (2.4), the free-surface condition for the third-order potential is

$$\begin{aligned} -9K\phi^{(3)} + \phi_z^{(3)} &= -\frac{1}{g}[K\phi^{(1)}\nabla\phi^{(1)} \cdot \nabla\phi_z^{(1)} + \frac{1}{8}\nabla\phi^{(1)} \cdot \nabla(\nabla\phi^{(1)} \cdot \nabla\phi^{(1)}) \\ &\quad + \frac{1}{4g}(K\phi^{(1)}\phi_z^{(1)} + \frac{1}{2}\nabla\phi^{(1)} \cdot \nabla\phi^{(1)})(-K\phi_z^{(1)} + \phi_{zz}^{(1)})] \\ &\quad + \frac{i\omega}{g}[-3\nabla\phi^{(2)} \cdot \nabla\phi^{(1)} + \frac{1}{2}\phi^{(1)}(\phi_{zz}^{(2)} - 4K\phi_z^{(2)}) + \phi^{(2)}(\phi_{zz}^{(1)} - K\phi_z^{(1)})] \\ &\quad - \frac{K}{8g}(\phi^{(1)})^2(K\phi_{zz}^{(1)} - \phi_{zzz}^{(1)}) \\ &= q^{(3)}, \end{aligned} \tag{3.36}$$

where $q^{(3)}$ is the notation for the third-order forcing function. The last group of terms of the forcing function in equation (3.36) vanishes, with the use of the Laplace equation and the first-order free-surface condition (2.11). The forcing function has triple products of the first-order quantities, and products of the first- and second-order quantities. The number of forcing terms increases rapidly with increasing the order of the potential.

It is well known that the second-order forcing function persists over the far field, but the far-field behavior of the third-order forcing function is less obvious.

The diffraction body boundary conditions are homogeneous conditions,

$$\frac{\partial\phi^{(2)}}{\partial n} = 0, \quad \text{on } S_b, \tag{3.37}$$

and

$$\frac{\partial \phi^{(3)}}{\partial n} = 0, \quad \text{on } S_b. \tag{3.38}$$

3.2.2 Boundary Integral Equations

Applying Green's theorem to the nonlinear potential, the boundary integral equation for $\phi^{(2)}$ is

$$2\pi\phi^{(2)} + \iint_{S_b} \phi^{(2)} \frac{\partial G(\mathbf{x},\xi)}{\partial n} d\xi = \iint_{S_f} q^{(2)} G(\mathbf{x},\xi) dS, \tag{3.39}$$

where the free-surface Green function defined in equation (2.16) satisfies the homogeneous free-surface boundary condition equation (3.35). S_f is the mean free surface, and S_b is the mean submerged body surface, which are defined in Figure 2.1 The boundary integral equation for $\phi^{(3)}$ is

$$2\pi\phi^{(3)} + \iint_{S_b} \phi^{(3)} \frac{\partial G(\mathbf{x},\xi)}{\partial n} dS = \iint_{S_f} q^{(3)} G(\mathbf{x},\xi) dS, \tag{3.40}$$

where the free-surface Green function defined in equation (2.16) satisfies the homogeneous free-surface boundary condition (3.36). The integral equations (3.39) and (3.40) have an integral over the entire free surface on the right-hand side.

3.2.3 Nonlinear Wave Loads

The total horizontal force F acting on a body can be obtained from the integration of the pressure p over the wetted body surface. Applying the Bernoulli equation, F can be written as

$$\begin{aligned} F &= \iint_{s_b} p n_x dS \\ &= -\rho \iint_{s_b} (\Phi_t + \frac{1}{2}\nabla\Phi \cdot \nabla\Phi) n_x dS \\ &\quad -\rho \int_{C_w} dl \int_0^{\zeta} (\Phi_t + \frac{1}{2}\nabla\Phi \cdot \nabla\Phi + gz) n_x dz, \end{aligned} \tag{3.41}$$

where C_w is the waterline, the intersection of the body with the mean free surface. The total force can be expanded as

$$\begin{aligned} F &= Re(F^{(1)}e^{i\omega t} + F^{(2)}e^{2i\omega t} + F^{(3)}e^{3i\omega t} \\ &\quad + \bar{F}^{(2)} + \bar{F}^{(3)}e^{i\omega t}) + O(\epsilon^4), \end{aligned} \tag{3.42}$$

where $F^{(1)}$ is the first-order force, $F^{(2)}, F^{(3)}$ are the second- and third-order sum-frequency forces, and $\bar{F}^{(2)}, \bar{F}^{(3)}$ are the second- and third-order difference-frequency forces.

Upon solving for the second- and third-order potentials, the nonlinear forces are obtained,

$$\begin{aligned} F^{(2)} &= -\rho \iint_{S_b} (2i\omega\phi^{(2)} + \frac{1}{4}\nabla\phi^{(1)} \cdot \nabla\phi^{(1)}) n_x dS - \frac{\rho}{4} K \int_{c_w} (\phi^{(1)})^2 n_x dl \\ &= F_1^{(2)} + F_2^{(2)}, \end{aligned} \tag{3.43}$$

where $F_1^{(2)}$ is the quadratic component due to the first-order potential, and $F_2^{(2)}$ is the second-order component due to the contribution from the second-order potential itself. $F^{(3)}$ is decomposed into three components

$$F^{(3)} = F_1^{(3)} + F_2^{(3)} + F_3^{(3)}, \tag{3.44}$$

where $F_1^{(3)}$ is due to the first-order contribution, $F_2^{(3)}$ due to the second-order contribution, and $F_3^{(3)}$ due to the third-order contribution. Each component is obtained by the following relations:

$$F_1^{(3)} = \frac{i\rho\omega}{8g} \int_{C_w} (\nabla\phi^{(1)} \cdot \nabla\phi^{(1)} + K^2\phi^{(1)}\phi^{(1)})\phi^{(1)} n_x dl, \tag{3.45}$$

$$F_2^{(3)} = -\frac{\rho}{2} \iint_{S_b} (\nabla\phi^{(1)} \cdot \nabla\phi^{(2)}) n_x dS - \rho K \int_{c_w} \phi^{(2)}\phi^{(1)} n_x dl, \tag{3.46}$$

$$F_3^{(3)} = -3i\rho\omega \iint_{S_b} \phi^{(3)} n_x dS. \tag{3.47}$$

3.3 Comparison of Two Theories

The long-wave approximation theory and the conventional perturbation theory are based on different assumptions, which lead to different boundary conditions and thus to different integral equations.

In the long-wave approximation theory, the free-surface condition is an inhomogeneous Neumann condition, and the free surface is the moving first-order wave elevation surface. The nonlinear potential Ψ has both second- and third-harmonic terms, $\Psi^{(2)}$ and $\Psi^{(3)}$, which are of the same order. These two terms can be compared to $\phi^{(2)}$ and $\phi^{(3)}$ in the conventional perturbation theory, although $\phi^{(2)}$ and $\phi^{(3)}$ are of different orders. The forcing function is assumed to be significant in the inner domain. For the perturbation theory, the free-surface conditions are more complicated, with $-4K\phi^{(2)}$ and $-9K\phi^{(3)}$ terms on the left-hand side of equations (3.35) and (3.36). There are more terms in the forcing function, and the foricng function persists over the far field.

3.4 Nonlinear Incident Potential in Infinitely Deep Water

From the definition in equation (2.8), the first-order incident potential is

$$\phi_I = \frac{gA}{\omega} e^{(Kz - iKx)}. \tag{3.48}$$

The wave amplitude of the incident potential is small compared to the wave length, so the second- and third-harmonic incident potentials satisfy the nonlinear free-surface conditions, equations (3.35) and (3.36) respectively.

Considering the monochromatic wave, substituting ϕ_I into the right-hand side of (3.35) gives

$$\begin{aligned} \nabla\phi_I \cdot \nabla\phi_I &= (\phi_I)^2(-iK, K)\cdot(-iK, K) = 0, \\ -K\frac{\partial\phi_I}{\partial z} + \frac{\partial^2\phi_I}{\partial z^2} &= -K^2\phi_I + K^2\phi_I = 0. \end{aligned} \tag{3.49}$$

The two terms on the right-hand side of (3.35) vanish for the second-harmonic incident potential, so the second-harmonic potential vanishes for infinite water depth. For the third-harmonic forcing function in equation (3.36), the terms with the second-harmonic incident potential components vanish. The other terms with only the first-harmonic potential all contain either $(\nabla\phi_I \cdot \nabla\phi_I)$ component or $(-K\partial\phi_I/\partial z + \partial^2\phi_I/\partial z^2)$ component. Therefore, the free-surface condition for the third-harmonic potential vanishes, and the third-harmonic incident potential vanishes. Both the second- and third-harmonic incident potentials are zero in infinite water depth.

Chapter 4

Numerical Methods

The integral equations for the nonlinear problems discussed in Chapter 3 can be solved numerically by a panel method. This chapter describes two different numerical methods: the low-order panel method and the higher-order panel method.

In the low-order panel method, the body surface and the free surface are discretized into a finite number of planar panels. Assuming that the potential is constant on each panel, a set of linear equations can approximate the integral equation to be solved. In this method, the integral of the Green function and its derivatives are evaluated by subroutines in WAMIT (Newman[31], Newman[32]).

For the higher-order panel method, the body geometry and the potential are approximated by B-splines. A set of linear equations with the same number of unknowns is solved by a semi-discrete Galerkin procedure. In this method, an adaptive subdivision algorithm ([27]) is developed for the evaluation of the Rankine near-field coefficients. The wave part of the Green function and its derivatives are evaluated by the corresponding subroutines from WAMIT.

For WAMIT, the formulation of the second-order problem is based on the conventional perturbation theory. Since the forcing function persists over the entire free surface, some numerical techniques are developed to integrate the entire free surface ([23],[24]). The free surface is divided into three regions, separated by two circles with different radii. The radius of the outer circle is large enough so that the local evanescent modes can be ignored. In the outer region of the free surface, both the Green

function and the first-order potential are expanded in Fourier-Bessel series. After the integration of the trigonometric functions with respect to the angular coordinate, the free-surface integral is reduced to a summation of line integrals in the radial coordinate. The radius of the inner circle is large enough to enclose only the body. In the inner domain, the free surface is discretized with panels. The integration over the intermediate annulus is based on Gauss-Chebyshev quadrature in the azimuthal direction and Gauss-Legendre quadrature in the radial direction.

We are interested in the second- and third-harmonic solutions at relatively low frequencies. In the long-wave approximation, the forcing function is assumed to be significant in the inner domain. In the conventional perturbation method, we neglect two contributions in our numerical computation: the forcing function in the far field and the second-order potential contribution to the third-order forcing. These simplifications are based on the arguments of the long-wave approximation theory, discussed in Chapter 3.

Since the forcing functions from both theories are confined only in the inner domain, it is not necessary to divide the free surface into different regions. The free-surface integration is obtained by truncation of the free surface at some distance away from the body. Numerical tests are required to determine the appropriate truncation radius b. In the low-order panel method, the truncated free surface is discretized into flat panels, and the potential and the forcing function are evaluated at the centroid of each panel. In the higher-order panel method, the free surface is represented by B-splines. A technique to evaluate the forcing function in B-splines is developed, and will be discussed later in this chapter.

The integral equations derived in Chapter 3 have the time-varying surfaces in the long-wave approximation theory and the mean surfaces in the conventional perturbation theory. The numerical procedures for both theories are basically the same except for the different surfaces. Unless specified in this chapter, the numerical implementations of solving the integral equations are for the long-wave approximation theory, but also apply to the conventional perturbation theory.

4.1 Discretization of the Moving Surfaces

In the long-wave approximation theory, the free-surface condition is satisfied on the first-order wave elevation. For a monochromatic wave, the first-order wave elevation changes periodically, so the instantaneous free surface and the body surface are rediscretized at a sequence of time steps within one wave period. Two kinds of coordinates will be used in this section: Cartesian coordinates (x, y, z), and inner normalized coordinates (R, θ, Z), which are defined in equations (3.8) and (3.24). The mean surfaces are discretized in Cartesian coordinates, and the instantaneous surfaces are discretized in the inner normalized coordinates.

For a single truncated cylinder, even though the inner free surface moves up and down locally with time, its profile is horizontal plane all the time and the panels do not need to be changed. However, the submerged body surface changes, and those panels do need to be rediscretized. At a given time ωt, the vertical position of the submerged body surface is changed from its fixed position z to the instantaneous position in Cartesian coordinates: $(-z + A\sin\omega t)$. One way to reconstruct the panels on the body is to rediscretize only the panels near the free surface and to keep the rest of the panels unchanged. But this procedure could cause high aspect ratio panels near the free surface, and the total number of panels would be different at different time steps. To keep the same number of panels on the body and to preserve the uniformity of the panels, each of the vertical coordinates on the body is stretched. Let a cylinder draft be T, then for a given A and ωt, the submerged part of the draft is: $T + A\sin\omega t$. Thus the stretching ratio is $(T + A\sin\omega t)/T$, and the vertical inner normalized coordinate for each vertex is $Z = -z \times (T + a\sin\omega t)/T$ at each time step.

For an array of multiple cylinders or a TLP, the wave slope of the inner free surface changes with time, so the panels on both the local free surface and the body surface must be rediscretized at each time step. For a given time and position, the vertical coordinate of the free surface is changed from its mean position $z = 0$ to $z = A\sin(\omega t - Kx)$ in Cartesian coordinates. Therefore, the free surface is discretized according to its profile at each time step. The submerged body surface is discretized in

the same way as for a single cylinder. The vertical positions in Cartesian coordinates on the body are changed from z to $z + A\sin(\omega t - Kx)$, so the stretching ratio in this case is $(T + A\sin(\omega t - Kx))/T$, and the vertical inner normalized coordinate for each vertex is $Z = -z \times (T + A\sin(\omega t - Kx))/T$ for each time step.

4.2 Low-Order Panel Method

As a simple example, we discuss the numerical implementation for the integral equation of a truncated cylinder. In FNV theory, the analytical results are derived for an infinitely deep cylinder with long-waves. To verify the regime of the long-wave approximation method, numerical results are obtained in a range of increasing wavenumbers. In addition, the results of several cylinders with different drafts are obtained. In this section, unless specified, the numerical calculations are carried out for a deep cylinder with draft $T = 8a$ at $KA = 0.025$.

4.2.1 Evaluation of the Forcing Function

The first-order velocity and its derivatives are required to evaluate the forcing function (3.17) on the mean free surface $z = 0$. The source formulations in equations (A.2) and (A.3) are used to avoid double derivatives of the Green function. The source strength is first calculated on the body surface, then the velocities on the free surface are computed in Cartesian coordinates.

We use central differentiation to calculate the derivatives of the velocities on the free surface with respect to space in polar coordinates. The first and second derivatives with respect to z are evaluated using the free surface condition and the Laplace equation. Figure 4-1 shows the radial derivative of the velocity on the free surface, evaluated with several values of the finite radial difference $\triangle r$. The velocity is evaluated at the centroid of the waterline panel on the body along the normal to the body boundary at $\theta = \pi/4$. The total number of panels is 144 for one quadrant of the cylinder. The numerical solution agrees with the FNV solution except locally within a distance of about half a waterline panel length from the body. This numerical

difficulty is discussed in §4.2.3.

After every component required in the forcing function is calculated, the forcing function can be evaluated at the centroid of each panel on the free surface. Figure 4-2 shows the forcing function at $\theta = \pi/4$ for different wavenumbers. The forcing function decays rapidly along the radial distance as the field point moves away from the cylinder. In the figure, the numerical solution converges to the FNV solution as the wavenumber decreases, which is consistent with the long-wave approximation. Note that the forcing function is not correct close to the body. Figure 4-3 shows the numerical solution of the forcing function along the radial direction for cylinders with different drafts T. The solution is obtained at $Ka = 0.025$. All of the numerical solutions in Figure 4-3 are graphically close to the analytical solution for an infinitely deep cylinder. It should be noted that the solutions shown in Figures 4-1 - 4-3 are imaginary parts, and the real parts are relatively small in this case.

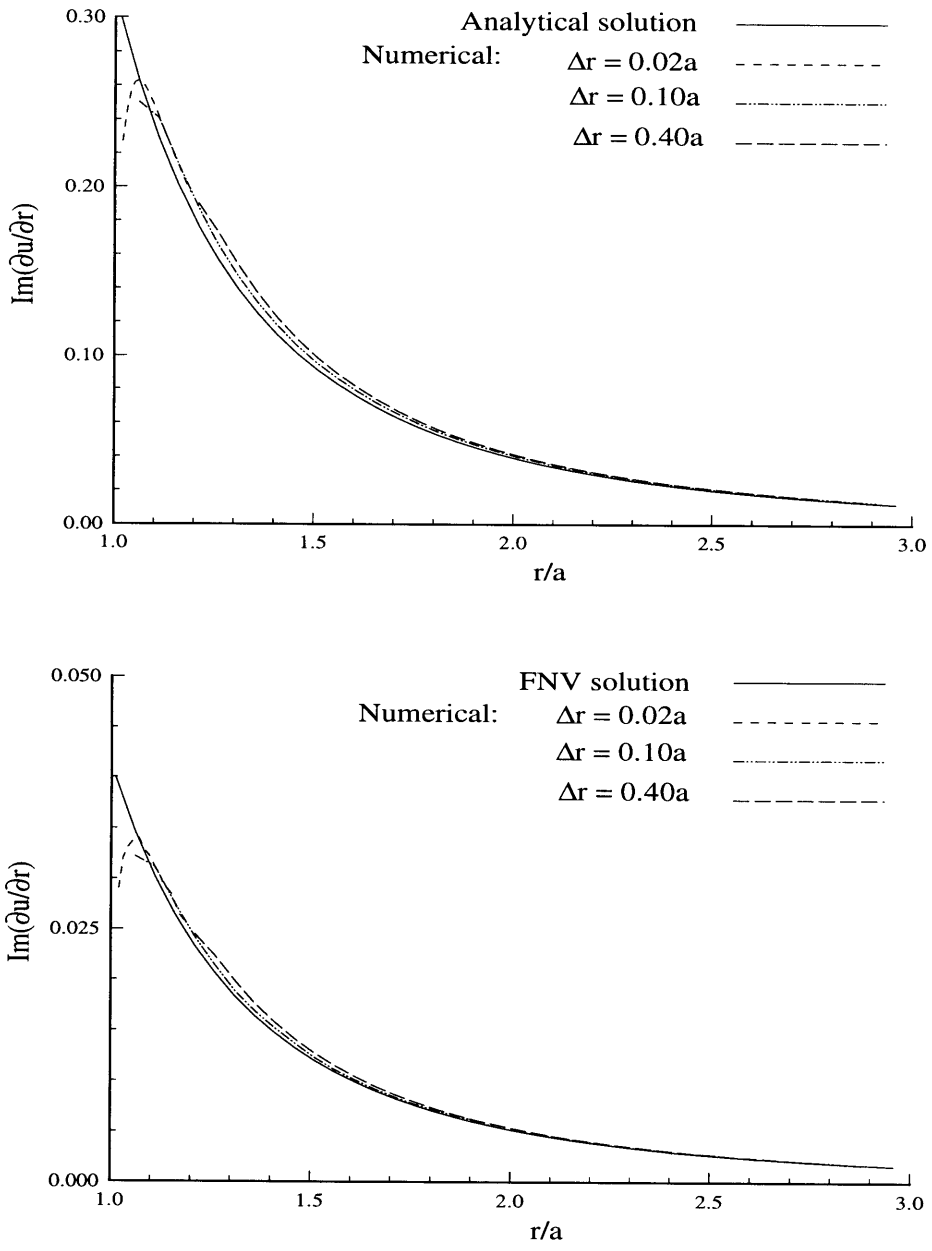

Figure 4-1: Comparison of the numerical derivatives of velocities on the free surface with the FNV results, $u = \partial\phi^{(1)}/\partial x$, and $v = \partial\phi^{(1)}/\partial y$.

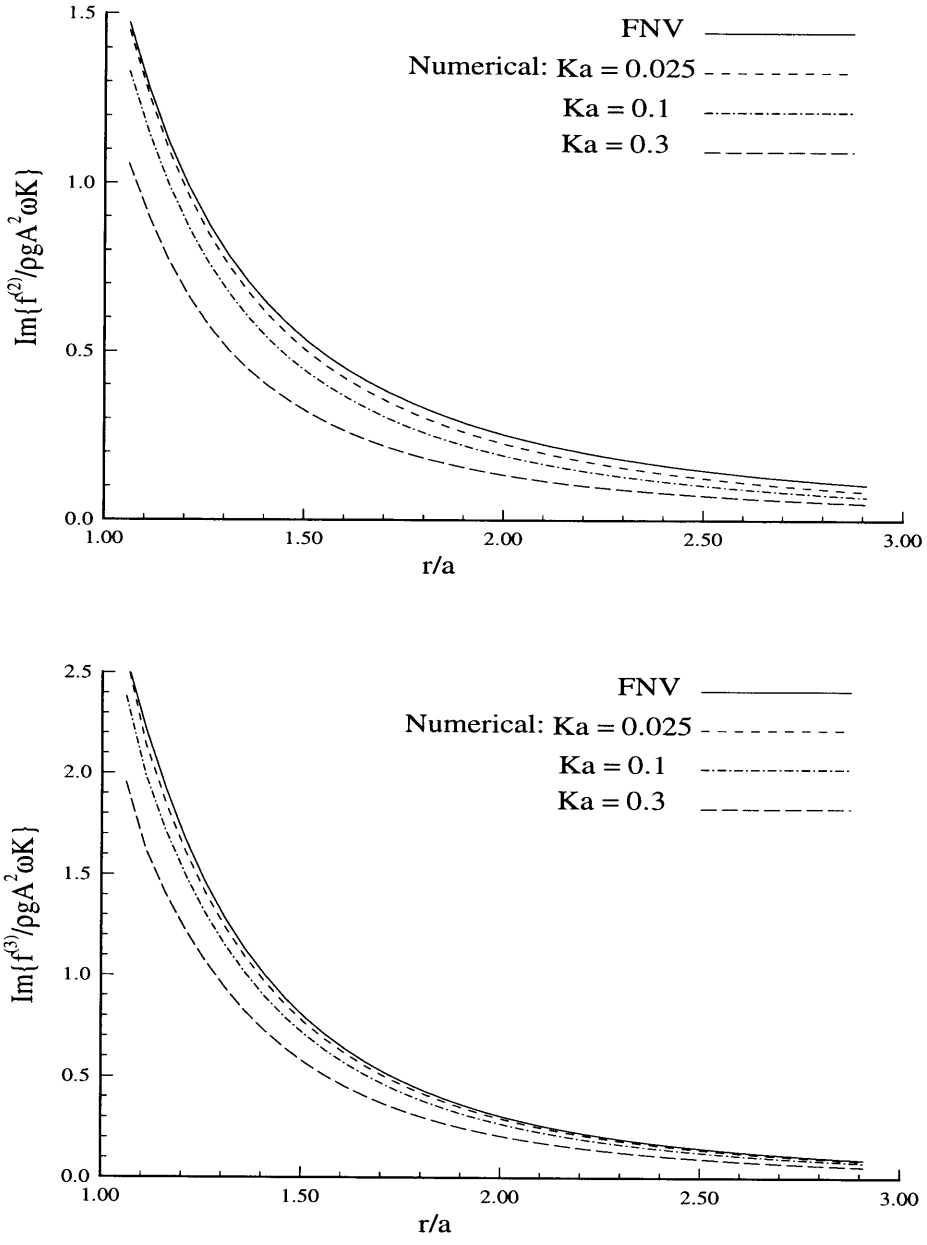

Figure 4-2: The forcing functions $f^{(2)}$ and $f^{(3)}$ as functions of r for different wavenumbers. The results are normalized by ωK.

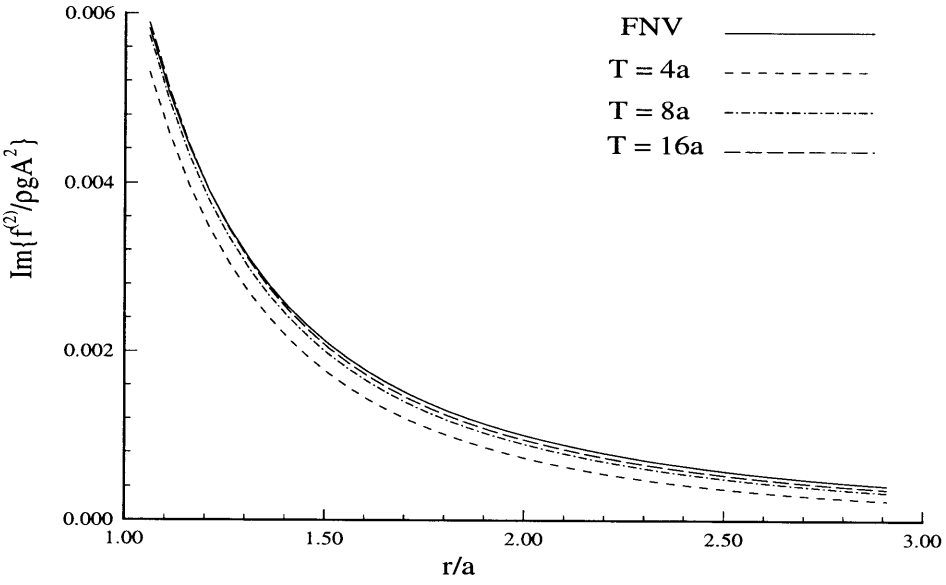

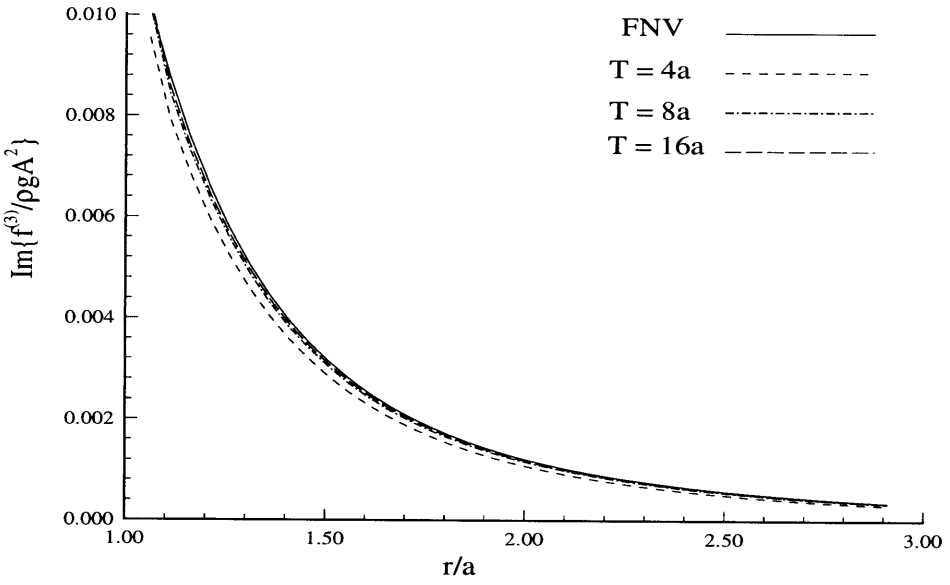

Figure 4-3: The forcing functions $f^{(2)}$ and $f^{(3)}$ as functions of r for cylinders with different drafts.

4.2.2 A Linear System of Equations

A low-order panel code is developed to solve the integral equation (3.23). Since the forcing function is a localized function, the free surface is truncated with truncation radius b.

The body surface and the inner free surface are divided into a finite number of flat panels, and a linear system is set up for the integral equation (3.19),

$$2\pi\Psi_i^{(2)} + \sum_{j=1}^{N_b} \Psi_j^{(2)} \iint_{S_j(t)} \frac{\partial G(\mathbf{x}_i, \xi_j)}{\partial n} dS = \sum_{j=1+N_b}^{N_f+N_b} f_j^{(2)} \iint_{S_j(t)} G(\mathbf{x}_i, \xi_j) dS, \quad (4.1)$$

or

$$2\pi\Psi_i^{(3)} + \sum_{j=1}^{N_b} \Psi_j^{(3)} \iint_{S_j(t)} \frac{\partial G(\mathbf{x}_i, \xi_j)}{\partial n} dS = \sum_{j=1+N_b}^{N_f+N_b} f_j^{(3)} \iint_{S_j(t)} G(\mathbf{x}_i, \xi_j) dS, \quad (4.2)$$

where $i = 1, \cdots, N_b$, N_b is the number of panels on the body, and N_f is the number of panels on the truncated free surface. $S_j(t)$ is the jth panel on the time-varying body surface and on the free surface. There are N_b unknowns and the same number of equations. This linear system is solved using LU decomposition and back-substitution. In order to obtain the solution at different time steps within one wave period, the submerged body surface is rediscretized at different times from $\omega t = 0$ to $\omega t = 2\pi$. At each time step, the linear system is set up to solve the integral equation, then the wave loads are calculated accordingly.

4.2.3 Numerical Difficulties

The components of the forcing function include the first and second derivatives of the first-order potential. The velocities are evaluated using the source formulation. The free-surface integration of the forcing function component of double derivatives with respect to z can be reduced to the integration along the waterline of the first derivative in the formulation by using the Gauss identity. However, in the forcing function, some terms containing the second derivative with respect to space must be evaluated numerically.

As shown in §4.1.1, the velocities on the free surface are not correct near the waterline even using the source formulation. If the source point and the field point are close to each other and to the free surface, the wave part of the Green function has a weak logarithmic singularity. Newman and Sclavounos [33] have developed a technique for the analytic integration of this logarithmic singularity in the low-order panel method.

Figure 4-4 shows the relative errors of the first-order potential on the free surface along the radial direction for a bottom mounted cylinder with radius a and draft $T = 6a$. Figure 4-5 shows the relative and absolute errors of its derivative with respect to the radial direction of the same cylinder. The numerical results are obtained with the source formulation, and the integration of the logarithmic singularity is evaluated analytically. The analytical solution is by the method of MacCamy and Fuchs (Mei [29]), and the numerical solution is obtained along the normal to the body boundary at the mid-point of the waterline panels using the source formulation. The number of unknowns shown is for one quadrant of the body. The number of waterline panels is: 5, 9 and 15, and the waterline panel length is: $0.314a, 0.175a, and 0.105a$ for three different discretizations. The results are obtained at $\theta = \pi/4$ with wavenumber $K = 1.0$. The solution for the potential appears to be satisfactory everywhere, but not its radial derivative. Figure 4-5 shows that the relative error of this derivative is significant within one waterline panel distance from the body boundary. Though the radial derivative of the diffraction potential is small close to the body, the absolute error does not decrease near the waterline by increasing the number of panels on the body. Since the error of the derivative is relatively large, the numerical double derivatives cannot be correct close to the waterline, and the forcing function cannot be evaluated robustly in this region using the low-order panel method.

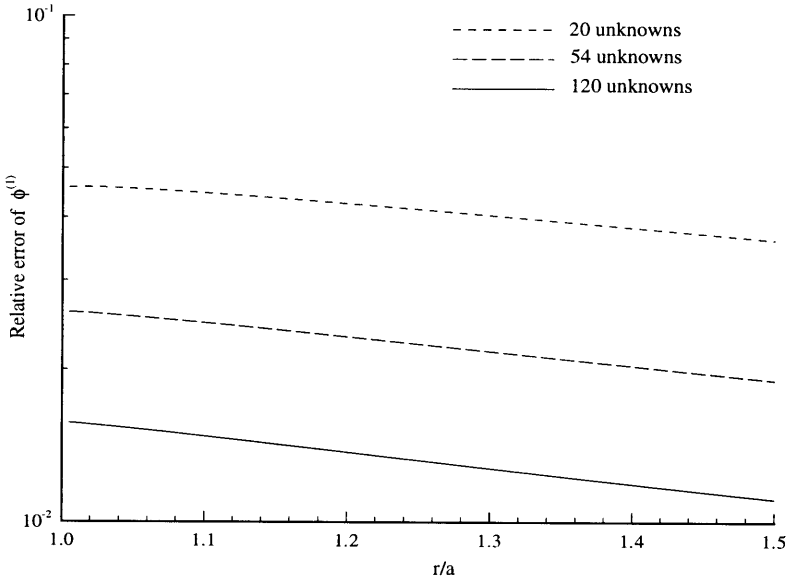

Figure 4-4: Relative error of $\phi^{(1)}$ on the free surface using the low order panel method.

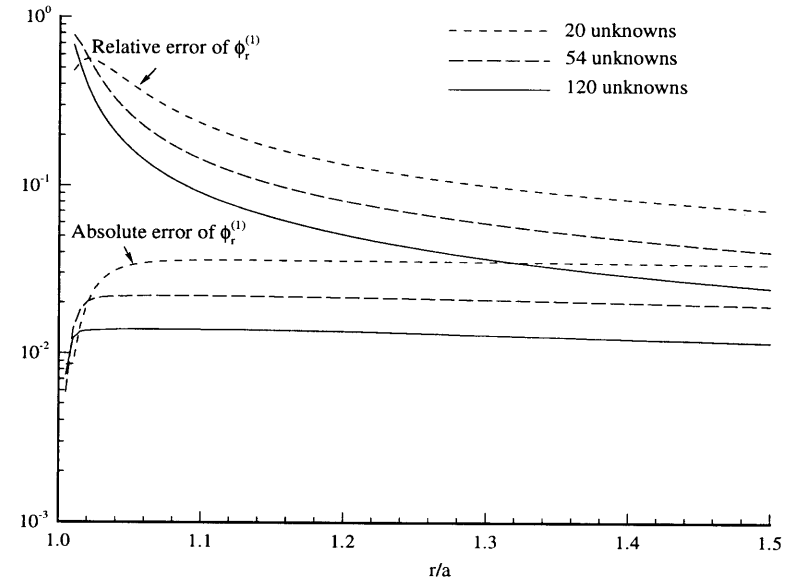

Figure 4-5: The errors of the radial derivative of $\phi^{(1)}$ on the free surface using the low order panel method. The top group of lines represent the relative errors, and the bottom group represent the absolute errors.

4.3 Higher-Order Panel Method

Due to the fundamental numerical difficulties in the low-order panel method, we shall implement a higher-order panel method using B-splines to solve the integral equations for the nonlinear potentials. A three-dimensional higher-order panel code has been developed by Maniar [27] to solve the first-order diffraction and radiation problems. We extend this code to solve the nonlinear diffraction problems. The geometry and unknown potential are represented by B-splines in this higher-order panel method. The basic idea of this method is outlined §4.3.1, and more details can be found in [27].

If the potential is represented by a B-spline of kth order, the potential has $(k-2)$ degrees of continuity. The first and second derivatives can be calculated analytically from the B-spline representation if $k > 3$. Therefore, there is no need to use the source formulation or the numerical differentiation for the evaluation of the derivatives.

4.3.1 B-spline Methodology

The body surface and the free surface are sub-divided into several continuous surfaces $(p = 1, \cdots, P)$, which are called patches. On each patch, the surface is described parametrically by a B-spline tensor product expansion,

$$\mathbf{x}^p(u,v) = \sum_{i=1}^{\tilde{I}_p} \sum_{j=1}^{\tilde{J}_p} \mathbf{x}_{ij}^p \tilde{U}_i^p(u) \tilde{V}_j^p(v), \tag{4.3}$$

where $\tilde{U}_i^p(u)$, and $\tilde{V}_j^p(v)$ are B-splines of order $\tilde{k}$ associated with the parametric variables u and v, and $\mathbf{x}_{ij}^p = (x_{ij}^p, y_{ij}^p, z_{ij}^p)$ are known vertices and coefficients. $\tilde{I}_p = \tilde{M}_p + \tilde{k} - 1$, $\tilde{J}_p = \tilde{N}_p + \tilde{k} - 1$, and $\tilde{M}_p, \tilde{N}_p$ are the numbers of non-zero intervals between consecutive knots of the usable space in the u, v directions. The unknown potential on the surface is represented in the similar way,

$$\phi^p(u,v) = \sum_{i=1}^{I_p} \sum_{j=1}^{J_p} \phi_{ij}^p U_i^p(u) V_j^p(v), \tag{4.4}$$

where $U_i^p(u)$, and $V_j^p(v)$ are B-splines of order k associated with the parametric variables u and v, and ϕ_{ij}^p are unknown coefficients to be solved for. $I_p = M_p + k - 1$, $J_p = N_p + k - 1$, and M_p, N_p are the numbers of non-zero intervals between consecutive knots of the usable space in the u, v directions.

The unknown potential coefficients are not the potentials in the physical sense. However, a given set of potential vertices and corresponding B-splines determine a continuous distribution of the velocity potential along the surface of each patch. No condition is imposed across the intersection of two adjoining patches, however, it is found that the continuity of the potential is satisfied automatically in [27].

For each patch, the usable domain is defined in the form

$$[\tilde{u}_{\tilde{k}}^p, \tilde{u}_{\tilde{I}_p+1}^p) \times [\tilde{v}_{\tilde{k}}^p, \tilde{v}_{\tilde{J}_p+1}^p), \tag{4.5}$$

where $\tilde{u}_m^p, \tilde{v}_n^p$ are the mth, nth knots of the knot vectors, which are a monotonically increasing sequence of integer values. The parametric space for the geometry B-splines is

$$[\tilde{u}_1^p, \tilde{u}_{\tilde{I}_p+\tilde{k}}^p) \times [\tilde{v}_1^p, \tilde{v}_{\tilde{J}_p+\tilde{k}}^p). \tag{4.6}$$

The B-splines for the surface and for the potential can be different in order and in the knot vectors. However, the usable rectangular parametric domain implicit in equation (4.4) must match that of the geometry in equation (4.3). Thus,

$$[u_k^p, u_{I_p+1}^p) \times [v_k^p, v_{J_p+1}^p) = [\tilde{u}_{\tilde{k}}^p, \tilde{u}_{\tilde{I}_p+1}^p) \times [\tilde{v}_{\tilde{k}}^p, \tilde{v}_{\tilde{J}_p+1}^p). \tag{4.7}$$

In this thesis, we refer to the panels in the higher-order panel method as the space between consecutive knots of the B-spline for the geometry. Therefore, for each patch p, the number of panels is $M_p \times N_p$, and the number of unknowns is $(M_p + k - 1) \times (N_p + k - 1)$.

4.3.2 A linear system of equations

For simplicity, we introduce the following equation

$$s\pi\phi + \iint_S \phi \frac{\partial G}{\partial n} dS = \iint_S qG dS \tag{4.8}$$

to represent the integral equations (3.23), (3.25), (3.39), or (3.40). Here: $s = 2$ or $s = 4$, S is the body surface or the sum of the body surface and the free surface, ϕ is the unknown potential to be solved for, and q is the right-hand side forcing function.

The difference of the right- and left-hand side of the above equation is defined as the residual in the form

$$r(u,v) = s\pi\phi + \iint_S \phi \frac{\partial G}{\partial n} dS - \iint_S qG dS. \tag{4.9}$$

Applying the Galerkin procedure to minimize the residual with respect to each of the potential B-spline tensor products in the usable domain (S_{ij}^p) gives

$$\iint_{S_{ij}^p} r(u,v) U_i^p V_i^p du dv = 0 \tag{4.10}$$

where $i = 1, 2, \cdots, I_p, j = 1, 2, \cdots, J_p$, and I_p, J_p are defined in equation (4.4). The potential is represented by equation (4.4) with a set of unknown coefficients, ϕ_{ij}^p. For each patch, the number of unknowns is the same as the number of equations, $I_p \times J_p$. The linear equations of the system are a C by C linear system, where

$$C = \sum_{p=1}^{P} (M_p + k - 1)(N_p + k - 1). \tag{4.11}$$

By using a Gauss-Legendre rule (order N_g), the outer integral of equation (4.10) can be replaced by a numerical integration,

$$\sum_{S_{ij}^p} \sum_{m=1}^{N_g} \sum_{n=1}^{N_g} w_m w_n r(u_m, v_n) U_i^p(u_m) V_j^p(v_n) = 0, \tag{4.12}$$

where w_m, w_n are the weight functions, and u_m, v_n are the nodes of the Gauss rule.

This procedure is called the outer Gauss rule. A linear square system of equations for the unknown coefficients of the potential is obtained by a semi-discrete Galerkin procedure to solve the integral equations numerically.

For the integration of the influence coefficients of the second and third terms in equation (4.8), the integrals are evaluated over each panel on a patch. This procedure is called the inner integration. On each patch, the integrals are approximated by a polynomial form of B-spline

$$\begin{aligned} &\iint (u-u_e)^m (v-v_e)^n \frac{\partial G}{\partial n} dS \\ &\iint (u-u_e)^m (v-v_e)^n G dS \end{aligned} \tag{4.13}$$

where (u_e, v_e) is some expansion point on the panel. An adaptive subdivision algorithm is developed to evaluate the Rankine influence near field coefficients, and the evaluation of the far-field Rankine influence is also described in [27]. For the evaluation of the integrals of the wave part in the Green function, a Gauss-Legendre rule, called the inner Gauss rule, is adopted. LU decomposition and back-substitution are used to solve the linear system.

Due to the presence of the singularity of the Green function when a field point and a source point are close, some caution is required to evaluate the right-hand side integral in equation (3.23). The forcing function should be evaluated in the B-spline form, and is replaced locally by a series expansion in the parametric variables,

$$\iint_{S_{ij}} qGdS = \sum_{m=0}^{\infty} \sum_{n=0}^{m} q_{mn} \iint u^m v^n G dS, \tag{4.14}$$

where q_{mn} is the coefficient for the polynomials. This procedure allows the use of adaptive schemes for the efficient evaluation of the integrals of G, independent of the behavior of the forcing function q. The numerical procedure to evaluate the forcing function in the B-spline form will be discussed in the next section.

For the long-wave approximation method, the free surface and body surface change over time, so the B-spline form of the geometry for each time step has to be recom-

puted.

4.3.3 Evaluation of the Forcing Function

To solve the nonlinear problem, the forcing function should be evaluated in the B-spline form. The higher-order panel method is first extended to evaluate the potential on the free surface in equation (2.20). Even though the solution of the potential on the body is in the B-spline form, we are not able to obtain the B-spline form for the potential on the free surface from equation (2.20) directly.

In order to obtain the B-spline form of the forcing function, the following procedures are used: (a) Truncate the free surface at a truncation radius b. The region within the truncation circle surrounding the body waterline is divided into several patches. (b) Over each patch, the potential is evaluated pointwise. The pointwise values of the potential are fit by B-splines using a least square procedure. (c) The first and second derivatives of the potential are evaluated from B-spline of the potential directly. After that, the forcing function is obtained pointwise on each patch. The B-spline coefficients for the forcing function are obtained using the same least square procedure as in fitting the potential. Some more detailed procedures are discussed below.

In the low-order panel method, the field quantities on the free surface should be evaluated along the normal to the waterline at the centroid of waterline segments to minimize the numerical error. Due to the continuity of the B-spline potential, the field quantities can be evaluated everywhere on the free surface in the higher-order panel method. Figure 4-6 shows the relative error of the potential on the free surface using this method. The geometry and wavenumber are the same as in Figure 4-4. $\tilde{k} = 4$ (the order of B-spline for the geometry), and $k = 4$ (the order of B-spline for the potential) are used in this calculation. The number of unknowns shown is for one quadrant of the body. The error decreases when the number of unknowns increases. Compared to Figure 4-4, the relative error of the coarse discretization of this method is at least one order smaller, while the number of unknowns is only about one-third of that used in the finest discretization in the low-order panel method. In this figure,

the error is the largest in the region close to the waterline and decays rapidly along the radial direction. For the fine discretization, the error is dominated by random error when $r/a > 1.1$, since single precision is used in the calculations. When the field point and the source point are close, the wave part of the Green function has a weak logarithmic singularity, which may contribute to the larger error near the waterline.

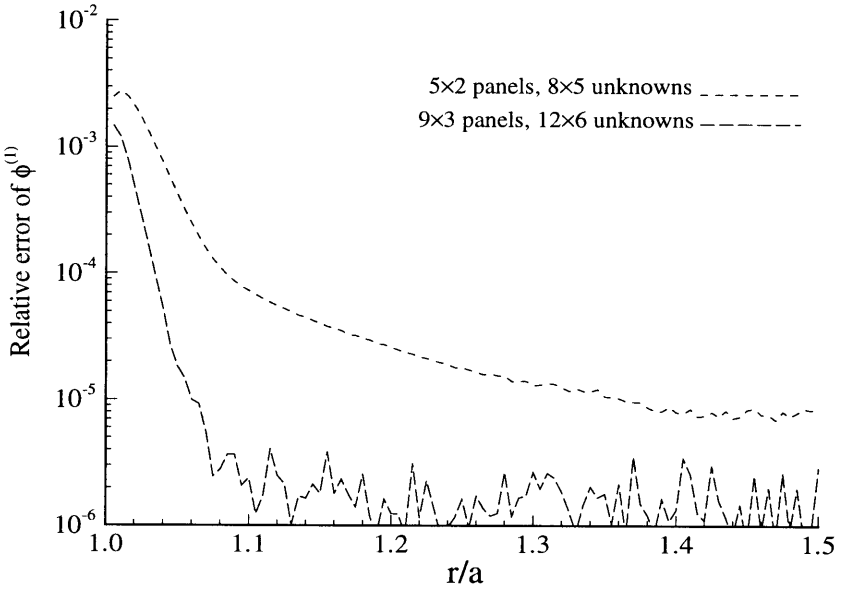

Figure 4-6: Relative error of $\phi^{(1)}$ on the free surface along the radial direction using the higher-order panel method.

When calculating the field quantities, the wave part of the influence coefficients is evaluated using a product Gauss-Legendre rule (the inner Gauss rule, defined in §4.3.3). Figures 4-7 and 4-8 show the error of the potential on the free surface. The geometry and the wavenumber are the same as used in Figure 4-4. The number of panels is $12 * 4$ for one quadrant of the body with $\tilde{k} = 4, k = 4$. 4×4 Gauss rules are used in Figure 4-7, while 6×6 Gauss rules are used in Figure 4-8. In general, the errors are smaller in Figure 4-8 due to the higher Gauss rule.

In these two figures, the local errors are larger around the locations of Gauss nodes and at the midpoints between two consecutive Gauss nodes. Figure 4-7 shows the solution obtained at four different radial distances from the body. The error is halved when the field point is moved from $r/a = 1.01$ to $r/a = 1.02$. Figure 4-8

shows the effect of moving the field point below the free surface $z = 0$. The error is also halved when the field quantity is evaluated at $z/a = -0.0025$, and is one order smaller when evaluated at $z/a = -0.01$, compared to the error on the free surface. The results suggest that the logarithmic singularity contributes to the relatively larger errors near the waterline intersection.

The errors of the potential and its derivatives on the waterline are shown in Figure 4-9. The solution is obtained directly from the integral equation (2.19). Since the radial derivative is zero due to the boundary condition, the derivatives shown are the derivatives in the x and y directions. The error of the potential does not have the behavior shown in Figures 4-7 and 4-8. The errors of the derivatives close to the waterline are about one order larger than the errors of the potential on the waterline.

Using the free surface condition, the Laplace equation, and the parametric representations for the potential and the patch geometry, the first and second derivatives of the potential can be obtained in Cartesian coordinates (Bingham and Maniar [2]). Appendix B lists more detailed formulations to evaluate these derivatives in parametric space.

Since the least square procedure is an over-determined system, the data set to be fit should be larger than the number of unknowns, the B-spline coefficients. From our numerical experience, the number of data points should be about two to four times more than the number of unknowns in the least square fitting.

Figure 4-10 shows the error of the radial derivative of the potential from the B-spline. Both the absolute error and the relative error are plotted. The geometry and wavenumber are the same as in Figure 4-4. 12×4 panels with $\tilde{k} = 5, k = 5$ are used for the fitting domain. The number of panels and unknowns shown is for the first-order solution with cubic orders of the B-splines for the geometry and the potential. Increasing numbers of panels on the body results in a more accurate potential on the free surface, then a more accurate B-spline form of the potential, and therefore more accurate derivatives. In the figure, the error decays rapidly as the field point moves away from the body. The relative error is below 1% in most of the range, and is below 2% at the waterline intersection. Compared to Figure 4-5, the error close to the

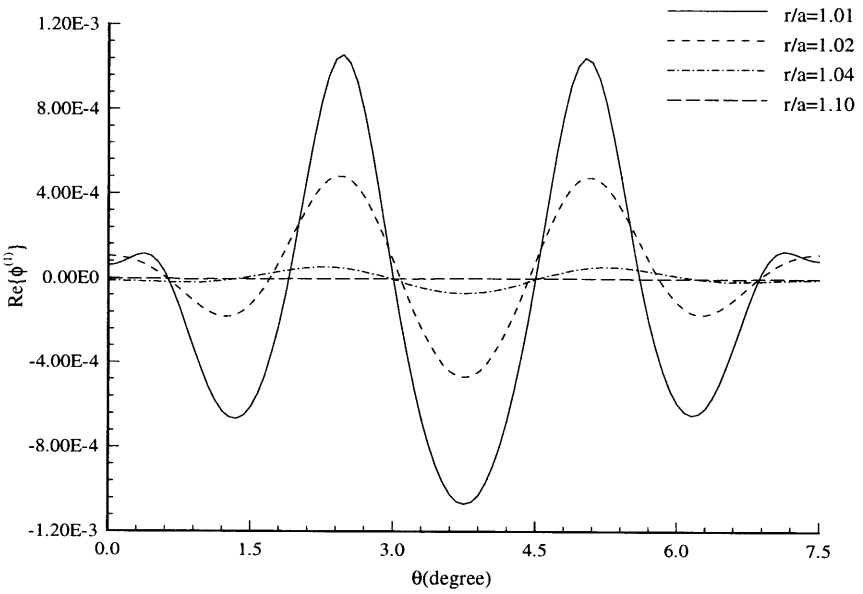

Figure 4-7: The errors of $Re\{\phi^{(1)}\}$ on the free surface for different r/a using the higher-order panel method.

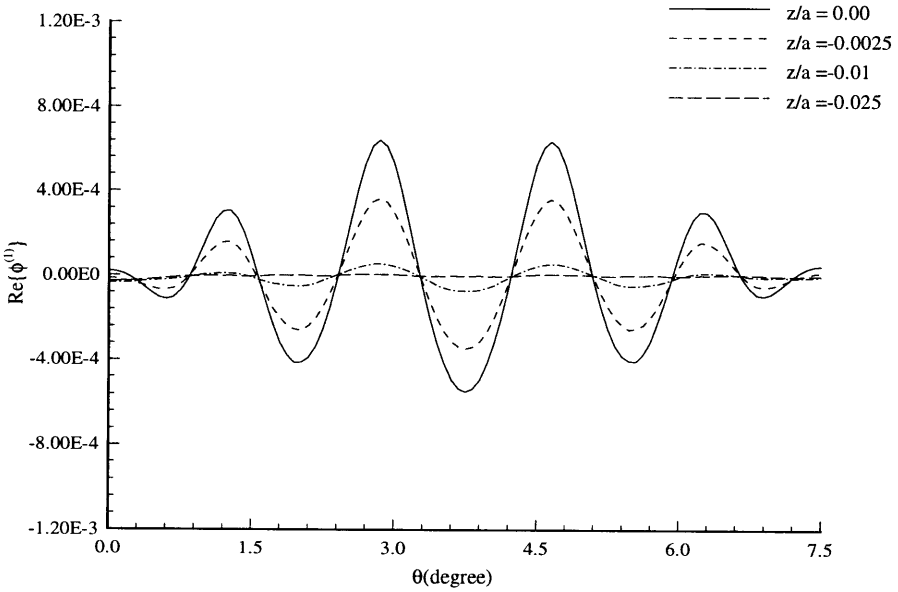

Figure 4-8: The errors of $Re\{\phi^{(1)}\}$ for different z below the free surface for $r/a = 1.01$ using the higher-order panel method.

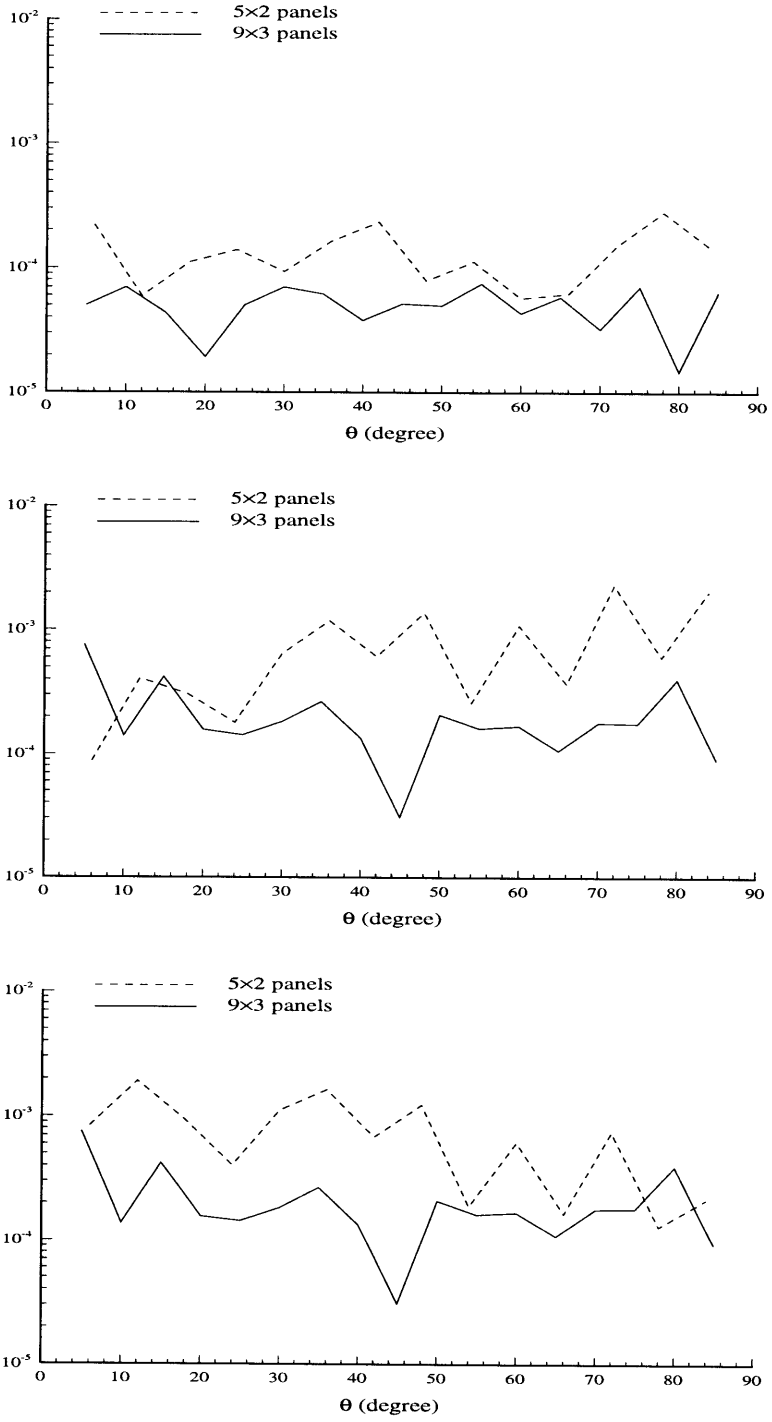

Figure 4-9: Relative error of $\phi^{(1)}$ (top figure), and its derivatives $\phi_x^{(1)}$ (middle figure) and $\phi_y^{(1)}$ (bottom figure) along the waterline using the higher-order panel method.

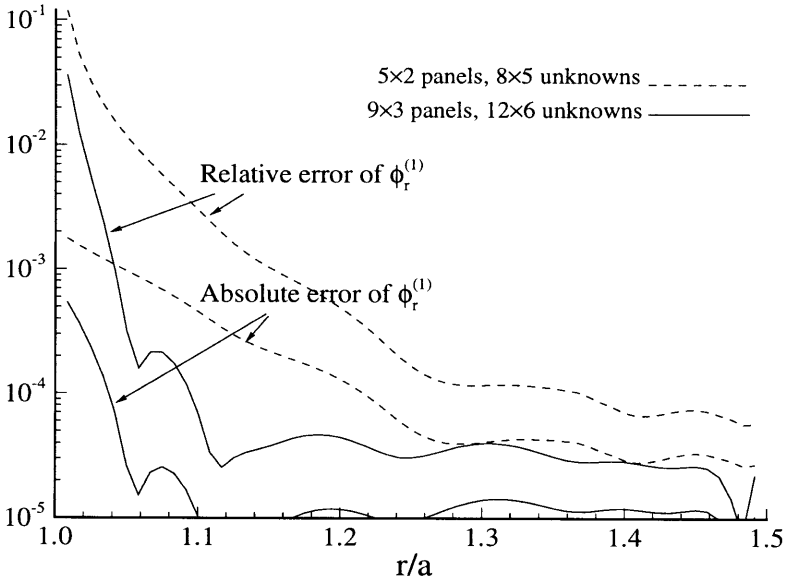

Figure 4-10: Relative and absolute errors of the radial derivative of the potential on the free surface using the higher-order panel method.

waterline is greatly reduced from the solution using the low-order panel method, and away from the waterline the error is several orders smaller. By increasing the number of unknowns in solving the first-order problem, the error close to the waterline can be reduced. Compared to Figure 4-9, the error on the free surface close to the waterline is about one order larger than the error on the waterline.

The accuracy of the least square fitting also depends on the parameters used for the fitted domain. Figures 4-11 and 4-12 show the effect on the first and second derivatives by increasing numbers of panels and the order of the B-spline for the fitted free-surface domain. The geometry and wavenumber are the same as in Figure 4-4, and 24×8 panels with $\tilde{k} = 5, k = 4$ are used in the first-order solution. In Figure 4-11, 12×4 panels are used for the free-surface domain by varying the fitting order k. In Figure 4-12, the fitting order $k = 5$ is fixed, and the solutions are obtained by changing the number of panels on the free surface. The error is not a smooth function, since the error is evaluated pointwise everywhere on the patch. The error decreases in most of the region when increasing numbers of panels or orders of the B-spline. However, the solution close to the waterline does not improve as significantly as the

solution away from waterline region.

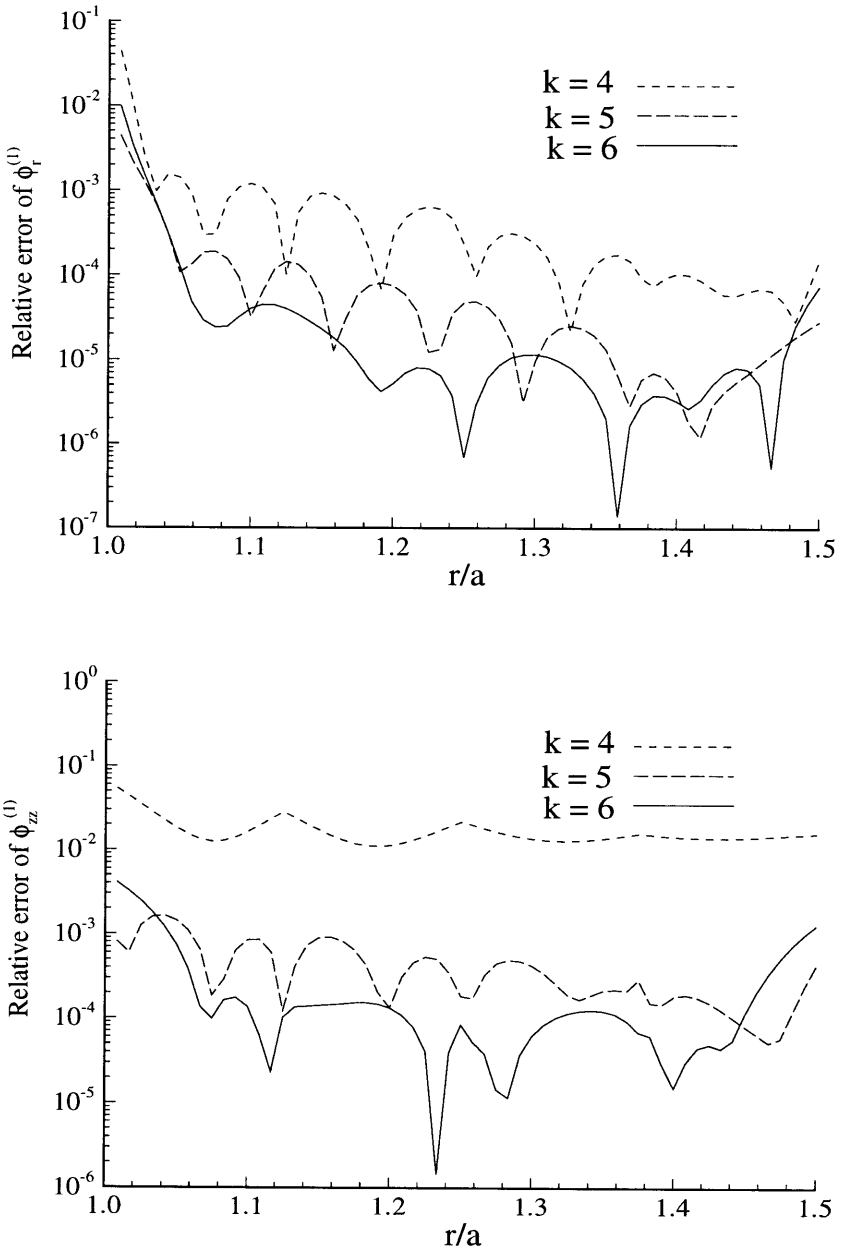

Figure 4-11: Relative error of the first and second derivatives on the free surface along the radial direction using the higher-order panel method with different orders of the B-spline.

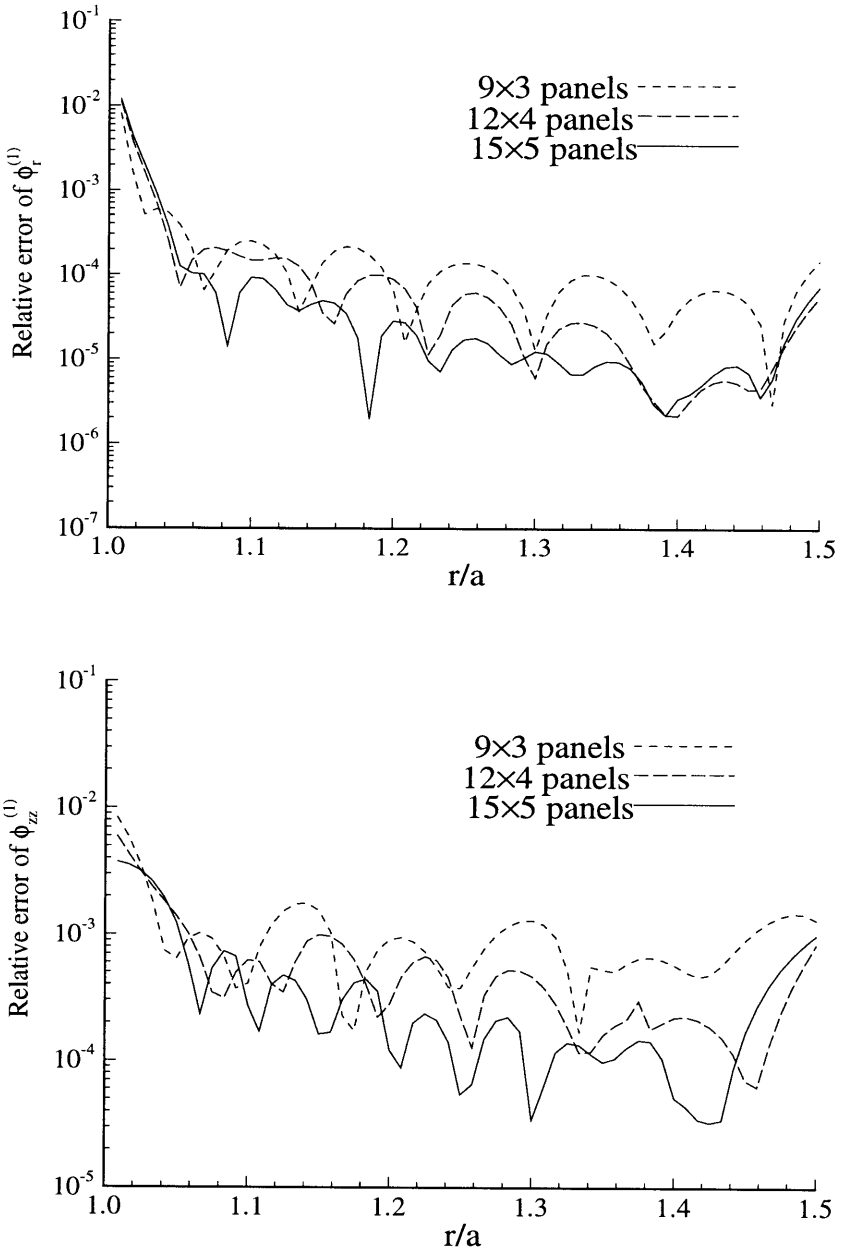

Figure 4-12: Relative error of the first and second derivatives on the free surface along the radial direction using the higher-order panel method with different number of panels.

Chapter 5

Numerical Results

This chapter presents the numerical results of the second- and third-harmonic potentials and the wave loads. The results are obtained from the integral equations of the long-wave approximation theory and the conventional perturbation theory. The numerical results by the low-order panel method illustrate the disadvantage of this method. Most of the numerical results in this chapter are computed using the higher-order panel method. Our interest is in the long-wave range, thus all the calculations are obtained for $Ka \leq 0.3$. All the wave loads computed are the horizontal forces.

5.1 Results of Long-Wave Approximation Theory

This section contains the numerical results of the long-wave approximation. The nonlinear potentials are obtained from the integral equation (3.23) for a truncated cylinder. In addition, for application to TLPs, the results of an array of four symmetric cylinders are obtained from the integral equation (3.25). The results of the wave loads are from equations (3.27), (3.28) and (3.29).

The numerical results for a truncated cylinder are compared with the FNV results. In FNV, the nonlinear potential on an infinitely deep cylinder is expressed as the Fourier series in equation (3.30). To facilitate the comparison, the numerical results of the potentials are also transformed into Fourier series. The numerical Fourier

transformation for $\Psi^{(2)}$ and $\Psi^{(3)}$ is

$$\Psi_n^{(j)}(R,Z) = \frac{1}{\pi c_n^{(j)}} \int_0^{2\pi} \Psi^{(j)}(R,\theta,Z)\cos n\theta d\theta, \qquad n = 0,1,..., \tag{5.1}$$

where $j = 2,3$, and $c_0^{(j)} = 2, c_n^{(j)} = 1$ for $n > 0$. $\Psi_n^{(j)}$ is the jth coefficient of the Fourier component for $\Phi^{(j)}$. Note that there are only four Fourier components for the nonlinear potential Ψ from FNV in equation (3.30), but there is an arbitrary number of components in the numerical transformation, even though most of the components should be small or zero numerically. Compared to the Fourier series for the FNV analysis, equation (5.1), Ψ_0 is comparable to $Im\{\Psi_0^{(2)}/(2\omega KA^2a)\}$, Ψ_1 to $Im\{\Psi_1^{(3)}/(\frac{1}{4}\omega KA^3)\}$, Ψ_2 to $Im\{\Psi_2^{(2)}/(\omega KA^2a)\}$, and Ψ_3 to $Im\{\Psi_3^{(3)}/(\frac{1}{4}\omega KA^3)\}$.

Since the body surface and the free surface change with time, the numerical results are obtained at several time steps within one wave period for each wavenumber. For simplicity, the numerical results presented in this chapter are for $\omega t = 0$ unless specified.

5.1.1 Results from the Low-Order Panel Method

This section shows some results of the nonlinear potentials from the long-wave approximation theory using the low-order panel method. The results are obtained for the truncated cylinder of draft $T = 8a$ with $Ka = 0.025$. Since we are able to use two planes of symmetry, only one quadrant of the body surface and the free surface is discretized. In the figures of this section, the number of panels and unknowns are specified for one quadrant.

The forcing function is assumed to be a local function, so the free surface is truncated at a specified distance away from the body, and a numerical test is carried out to determine the truncation radius b for the integral on the right-hand side of equation (3.19). Figure 5-1 shows the Fourier components Ψ_1 and Ψ_2 as functions of the depth Z, and the numerical solutions are compared with FNV results. 174 panels are used on one quadrant of the body. The numerical solutions are obtained for two different truncation radii and numbers of panels. The numerical solutions converge

graphically to the FNV solutions by increasing the truncation radius b and number of panels on the truncated free surface. The FNV solutions are about 5% larger than the numerical ones when the truncation radius, $b/a = 3.4$, is in the inner domain $Kb < O(1)$.

Figure 5-2 shows the Fourier component Ψ_0 as a function of Z. The numerical solution is obtained at $b/a = 3.4$. In this case, the difference is more significant between the numerical solution and the analytical solution of FNV. The numerical solutions do not converge to the FNV results when the number of panels on the body is increased. In fact, the difference is caused by the different geometries used in the numerical calculation and the analytical analysis. In Figure 5-3, the numerical results converge to the FNV results as the draft of the cylinder is increased from $8a$ to $16a$. Since the difference of the forcing function is a constant everywhere on the free surface, the effect is only significant in the Fourier component Ψ_0 term after the numerical Fourier transformation.

$\nabla\Psi$ is solved by the source formulation in the low-order panel method. In the source formulation, the potential is expressed in terms of source distributions of unknown strength σ over the body and the free surface (Appendix A.2), and σ is assumed to be constant on each panel.

Figure 5-4 shows the vertical derivative of the Fourier component Ψ_1. The solution is obtained by two discretizations on the body and compared with the FNV solution. The solution is not correct on the body within two panel lengths of the free surface. When a field point on the body and a source point on the free surface are both very close to the waterline, it is numerically difficult to evaluate the influence coefficients, as discussed in §4.1.3. As shown in the figure, the derivative close to the waterline does not converge when the number of panels is increased, although the solution away from the waterline converges to the FNV result. In addition to the difficulties in evaluating the forcing function near the waterline discussed in §4.1.3, the gradient of the nonlinear potential close to the waterline can not be evaluated accurately by the low-order panel method either.

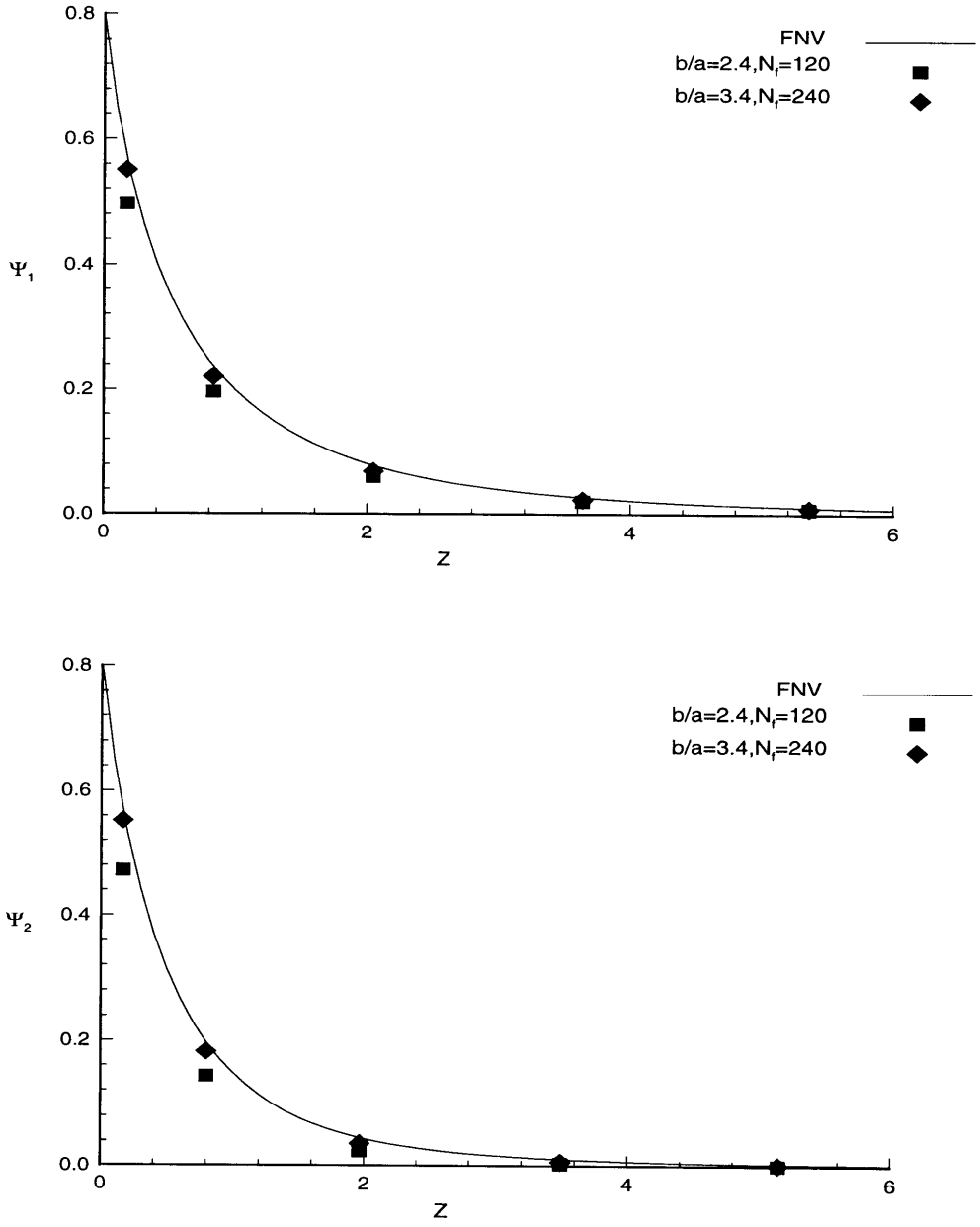

Figure 5-1: Comparison of the Fourier component Ψ_1 and Ψ_2 as functions of Z with the FNV results. The numerical results are obtained at two different truncation radii on the free surface.

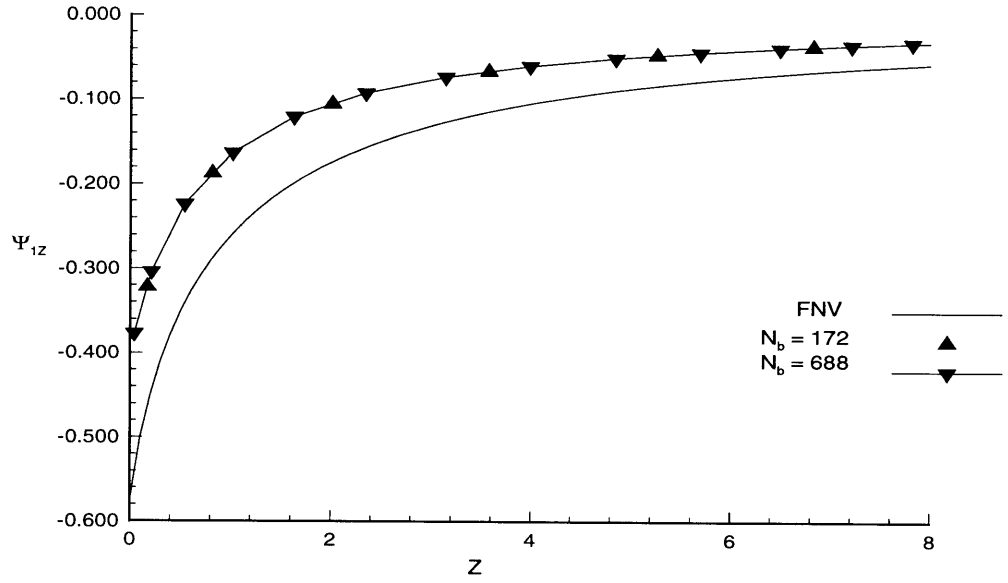

Figure 5-2: Fourier component Ψ_0 as a function of Z with different numbers of panels on the body.

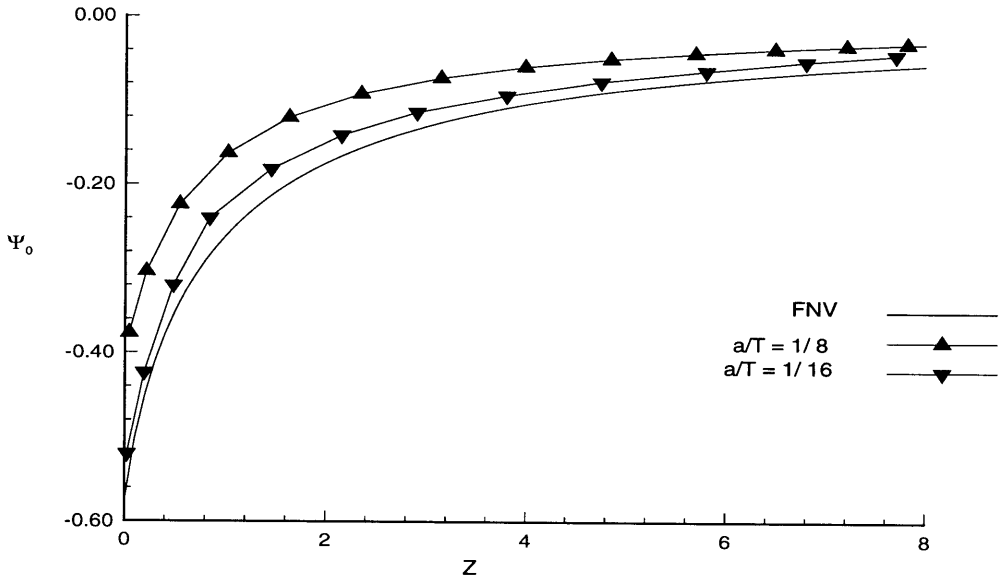

Figure 5-3: Fourier component Ψ_0 as a function of Z for cylinders with different drafts.

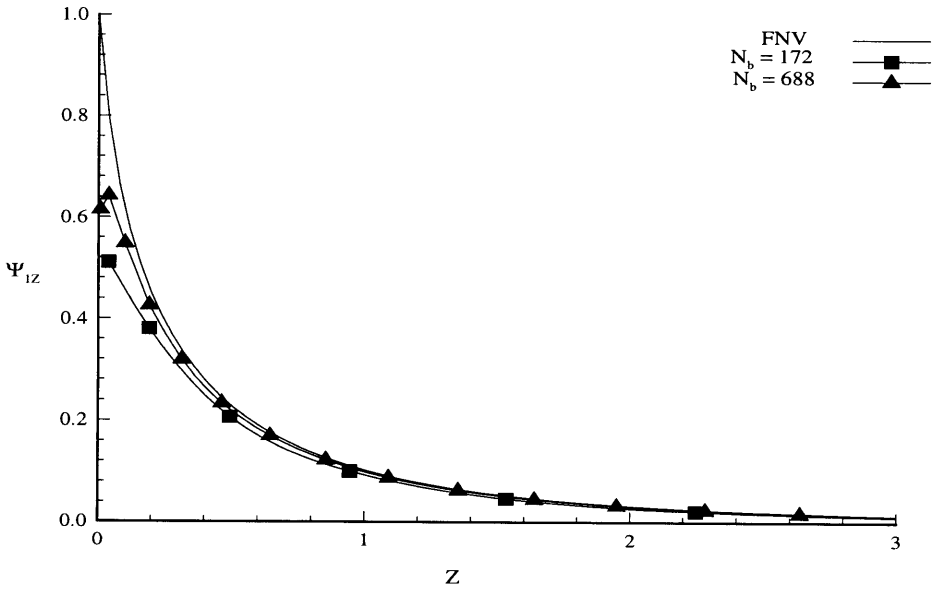

Figure 5-4: Comparison of Ψ_{1Z} as a function of Z with the FNV result.

5.1.2 Results from the High-Order Panel Method

One reason for using the higher-order panel method is to evaluate the forcing function robustly near the waterline, which is discussed in previous chapter. The other reason for using this method is to resolve the incorrect gradient of the nonlinear potential close to the waterline in the low-order panel method shown in Figure 5-4. In this method, the solution of the potential is represented by B-splines, so the potential and its derivatives can be evaluated everywhere on the body. We use three patches in the computation: one patch for the side of the cylinder, one patch for the bottom of the cylinder, and one for the truncated free surface.

Uniform discretization of panels is first used for the body surface and the free surface. Figure 5-5 shows the solutions for Ψ_1 and Ψ_{1Z} as functions of Z. The number of panels for the cylinder is $4 \times (12 + 2)$ with $\tilde{k} = 4$. The free surface is truncated at $b/a = 3.4$, and the number of panels on the free surface is 4×6. The solution is obtained with three different orders of B-spline for the potential and outer Gauss rule. The potential and its derivative converge to the FNV results when the orders are increased. Keeping the potential order and the order of the outer Gauss rule the

same, Figure 5-6 shows the numerical solution with three different discretizations on the body. In these two figures, $k = 5, \tilde{k} = 4$, and the outer Gauss order is 4×4 for all the calculations. The free surface discretization is the same as in Figure 5-5. The results of the derivative are improved when the number of panels is increased.

With cosine discretization on the body, Figure 5-7 shows that the potential and its derivative agree with the FNV solutions when $k > 3$, and the difference between the numerical solution and analytical solution is within 5%. The number of panels on the body in these Figures is $4 \times (8 + 2)$, and on the free surface is 4×6. The potential has $(k-2)$ degrees of continuity, so a larger k, is required to obtain accurate results for the derivatives. Since the difference of the potential is almost constant as a function of Z, the difference in the Z-derivative is much smaller.

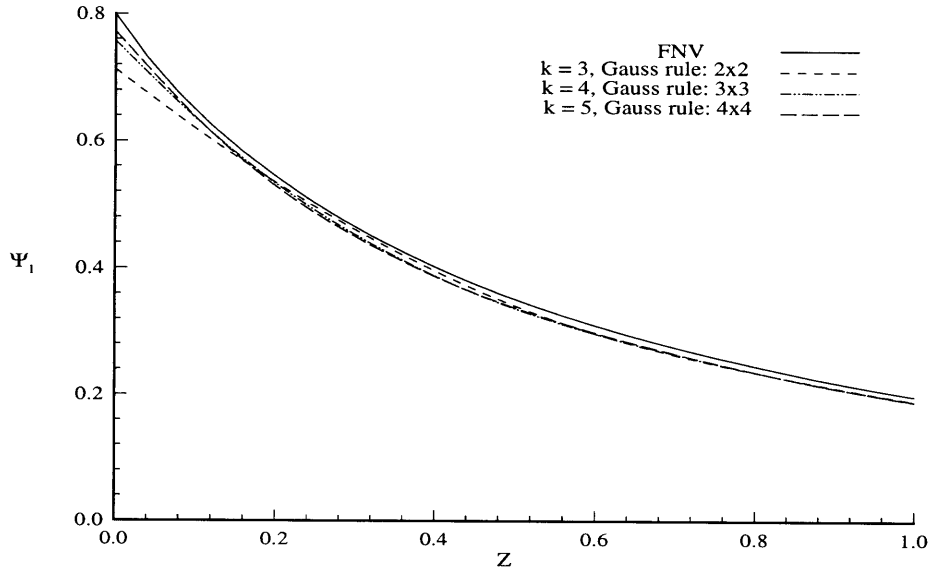

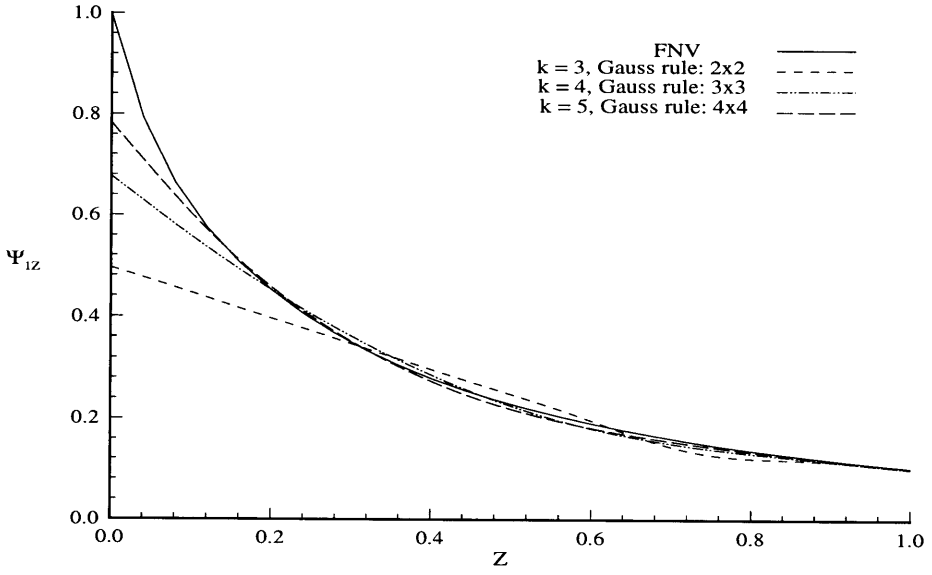

Figure 5-5: The results of Ψ_1 and Ψ_{1Z} as functions of Z with different orders of B-spline for the potential and the outer Gauss rule.

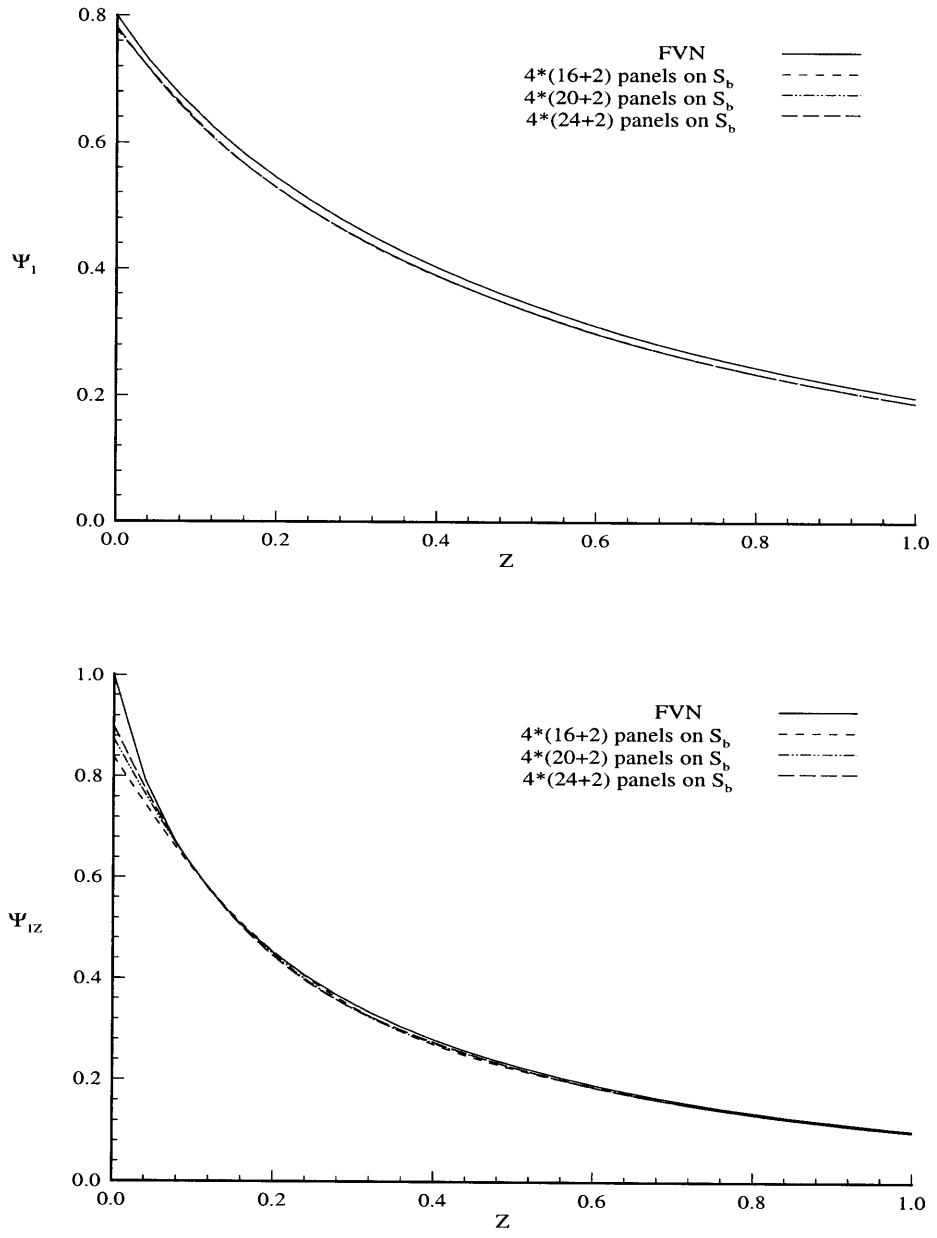

Figure 5-6: The results of Ψ_1 and Ψ_{1Z} as functions of Z with different discretizations on the body.

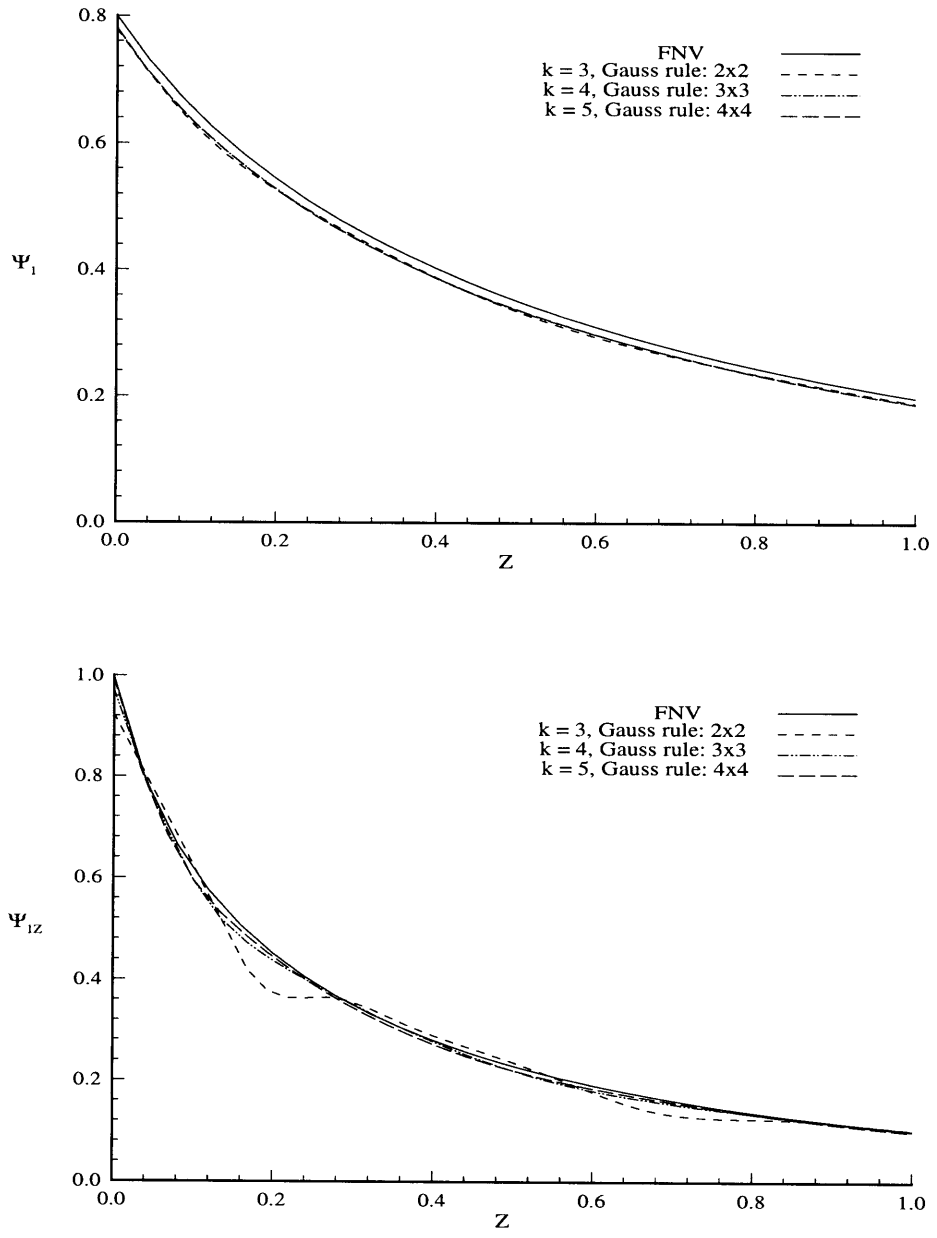

Figure 5-7: The results of Ψ_1 and Ψ_{1Z} as functions of Z using cosine discretization with different orders of B-spline for the potential and the outer Gauss rule.

Table 5.1 and Table 5.2 show the convergence of the nonlinear solution using the higher-order panel method. The results listed in the tables are for the wave load $F_3^{(3)}$ defined in equation (3.28). The geometry is a truncated cylinder with radius a and draft $T = 6a$. The free surface is truncated at $b/a = 6$.

Table 5.1 shows the convergence for different discretizations in solving the integral equation of the third-harmonic potential. The number of panels shown in the table is for the body surface, and the number of unknowns is also listed in the table. The order of the B-spline for both the geometry and the potential is cubic. On the free surface, the number of panels is $3 \times (3 + 1)$, $4 \times (4 + 2)$ and $6 \times (6 + 3)$ for three columns respectively. For all three results, the first-order potential on the free surface is obtained by using $12 \times (48 + 2)$ panels on the body. In the table, the numerical results of the nonlinear wave loads differ only in the fourth decimal place.

Table 5.2 shows the effect of increasing the accuracy of the forcing function while keeping all the parameters the same in solving the nonlinear potential. The number of panels listed is for the first-order solution. Increasing the number of panels means increasing the accuracy of the first-order solution, and therefore increasing the accuracy of the forcing function. When solving the integral equation for the third-harmonic potential, the number of panels and the order of the B-spline used are the same as for the results in the third column of Table 5.1. In Table 5.2, the results of the wave loads also differ only in the third or fourth decimal place.

After confirming that the numerical results agree with each other to several decimal place with different discretizations using the higher-order panel method, the results of truncated cylinders are compared with the FNV results. Figure 5-8 shows the difference of the wave loads between the numerical results and the FNV results. The numerical results are obtained for truncated cylinders of different drafts with different wavenumbers, and the free surface is truncated at $b/a = 6$. The results shown are $F_3^{(3)}$ defined in equation (3.28), and $F_{22}^{(3)}$ in equation (3.31). The difference between the numerical solution and analytical solution is small, and the difference decreases with decreasing wavenumber or increasing cylinder draft.

In the long-wave approximation, the forcing function is assumed to be only signifi-

Ka	$\lvert F_3^{(3)}\rvert/(\rho g A^3)$		
	$2 \times (4+1)$ panels	$3 \times (8+2)$ panels	$6 \times (16+3)$ panels
	$5 \times (7+4)$ unknowns	$6 \times (11+5)$ unknowns	$9 \times (19+6)$ unknowns
0.025	0.8540E-03	0.8690E-03	0.8688E-03
0.050	0.3550E-02	0.3556E-02	0.3557E-02
0.100	0.1533E-01	0.1531E-01	0.1530E-01
0.150	0.3919E-01	0.3850E-01	0.3855E-01
0.200	0.6900E-01	0.6947E-01	0.6944E-01
0.300	0.1545E+00	0.1552E+00	0.1553E+00

Table 5.1: The modulus of $F_3^{(3)}$ computed using different discretizations in solving the integral equation for the nonlinear potential. The number of panels shown in the table is for the body surface.

Ka	$\lvert F_3^{(3)}\rvert/(\rho g A^3)$		
	$6 \times (24+2)$ panels	$8 \times (30+2)$ panels	$12 \times (48+3)$ panels
0.025	0.8663E-03	0.8761E-03	0.8690E-03
0.050	0.3549E-02	0.3583E-02	0.3556E-02
0.100	0.1533E-01	0.1539E-01	0.1531E-01
0.150	0.3728E-01	0.3725E-01	0.3850E-01
0.200	0.6978E-01	0.7034E-01	0.6947E-01
0.300	0.1544E+00	0.1547E+00	0.1552E+00

Table 5.2: The modulus of $F_3^{(3)}$ computed using different discretizations to obtain the first-order solution. The number of panels shown is the discretization of the body surface in solving the first-order solution.

cant in the inner domain close to the body. Figure 5-9 shows the modulus of the same two wave loads in Figure 5-8 using different truncation radii. For $Ka \leq 0.2$, truncating the free surface at $Kb = O(1)$ is sufficient to achieve convergence. As expected, the difference between the numerical solution and analytical solution increases as the wavenumber increases for the same cylinder.

In the FNV analysis for an infinitely deep cylinder, the wave loads vanish for $F^{(2)}$, $F^{(4)}$, and $F_{21}^{(3)}$. Figure 5-10 shows the numerical results for $F^{(2)}$ and $F^{(4)}$. The magnitude of $F^{(4)}$ is small compared to other nonlinear wave loads, but not $F^{(2)}$ for $Ka > 0.1$. Figure 5-11 shows the numerical results for $F_{21}^{(3)}$, which vanishes in the

FNV analysis. The magnitude of $F_{21}^{(3)}$ is significant for $Ka > 0.1$. Figure 5-12 shows the results for $F_2^{(3)}$ in equation (3.28), and the results begin to differ from the FNV results when $Ka > 0.1$ due to the nonzero contribution from $F_{21}^{(3)}$.

The numerical results for $F^{(2)}$ and $F_{21}^{(3)}$ suggest that the Fourier component $\Psi_1^{(2)}$ defined in equation (5.1) does not vanish, in contrast to the analysis of FNV. A higher-order correction in the forcing function of FNV theory is derived in Appendix C for the infinitely deep cylinder. This higher-order correction term is neglected in the FNV analysis, but the contribution from this term to the right-hand side of equation (3.23) behaves like logarithm in the radial direction on the free surfaces. This correction term leads to the nonzero solution of $\Psi_1^{(2)}$.

Figures 5-13 and 5-14 show the Fourier components of $\Psi_1^{(2)}$ and $\Psi_2^{(2)}$ from equation (5.1) as functions of Z. $\Psi_2^{(2)}$ is normalized by $\omega K A^2$, and $\Psi_1^{(2)}$ is normalized by $\omega K^2 A^2$. The free surface is truncated at $b/a = 12$. In Figure 5-14, the numerical solution of $\Psi_2^{(2)}$ agrees with the analytical solution from FNV for $Ka < 0.20$. The nondimensional results in Figure 5-13 show that $\Psi_1^{(2)}$ is proportional to $\omega K^2 A^2$, which is consistent with the analysis in Appendix C. The magnitude of $\Psi_1^{(2)}$ is small for small wavenumbers, but the magnitude of $\Psi_1^{(2)}$ is about the same order of magnitude as $\Psi_2^{(2)}$ when $Ka > 0.1$. Therefore, the wave loads due to $\Psi_1^{(2)}$, shown in Figures 5-10 and 5-11, are significant for $Ka > 0.1$.

The analysis in Appendix C shows that the far-field contribution to $\Psi_1^{(2)}$ is significant. As shown in Figures 5-15 and 5-19, the second-harmonic potential and its related wave loads do not converge by truncating the free surface just in the inner domain, although the other components shown in this section converge. To include the complete far-field contribution, some analysis in the far field should be further carried out.

All the results presented above are obtained for $\sin \omega t = 0$. Figure 5-16 shows the nonlinear wave loads obtained at different time steps for $Ka = 0.15$. As shown in this figure, the results for different time steps do not change significantly.

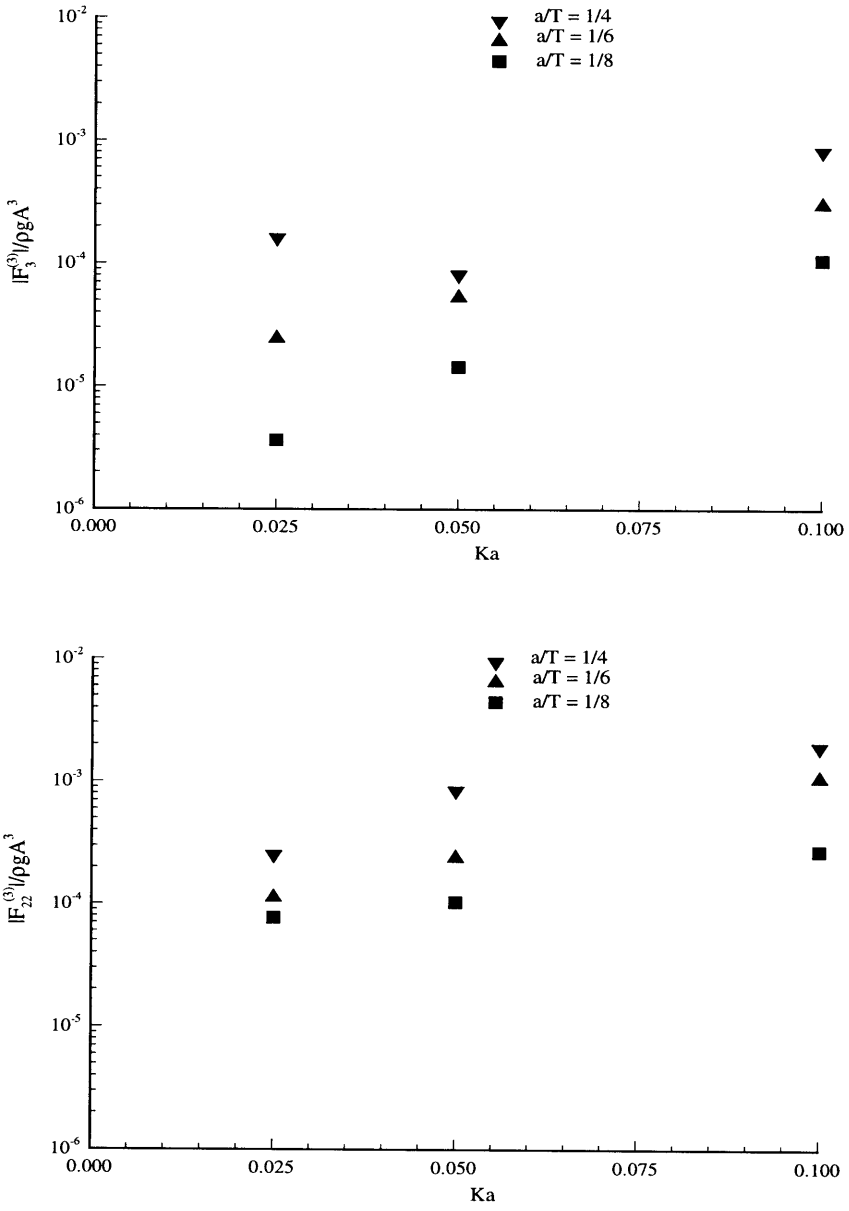

Figure 5-8: Difference of the modulus between the numerical solution for cylinders with different draft T and the FNV results. The top figure shows the difference of $F_3^{(3)}$. The bottom figure shows the difference of $F_{22}^{(3)}$.

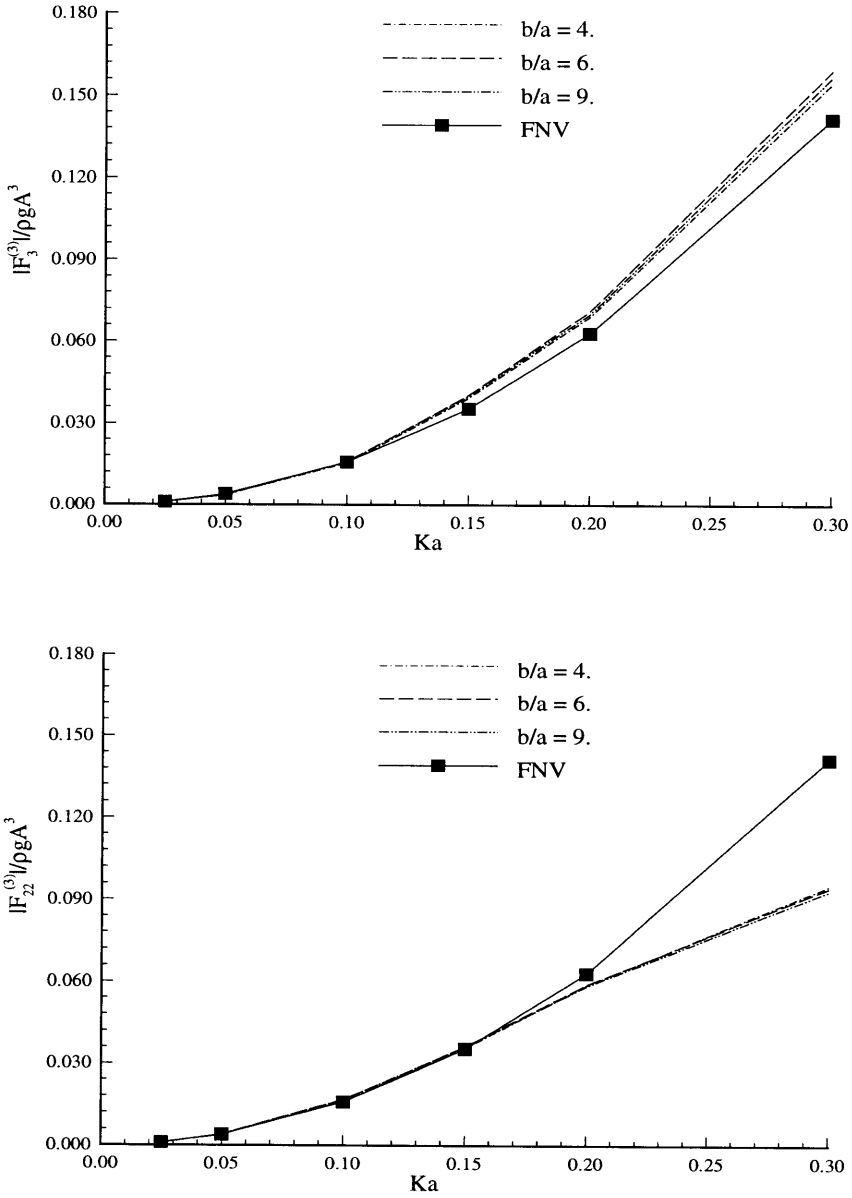

Figure 5-9: Modulus of the wave loads evaluated with different truncation radii on the free surface. The top figure shows the modulus $F_3^{(3)}$. The bottom figure shows the modulus of $F_{22}^{(3)}$.

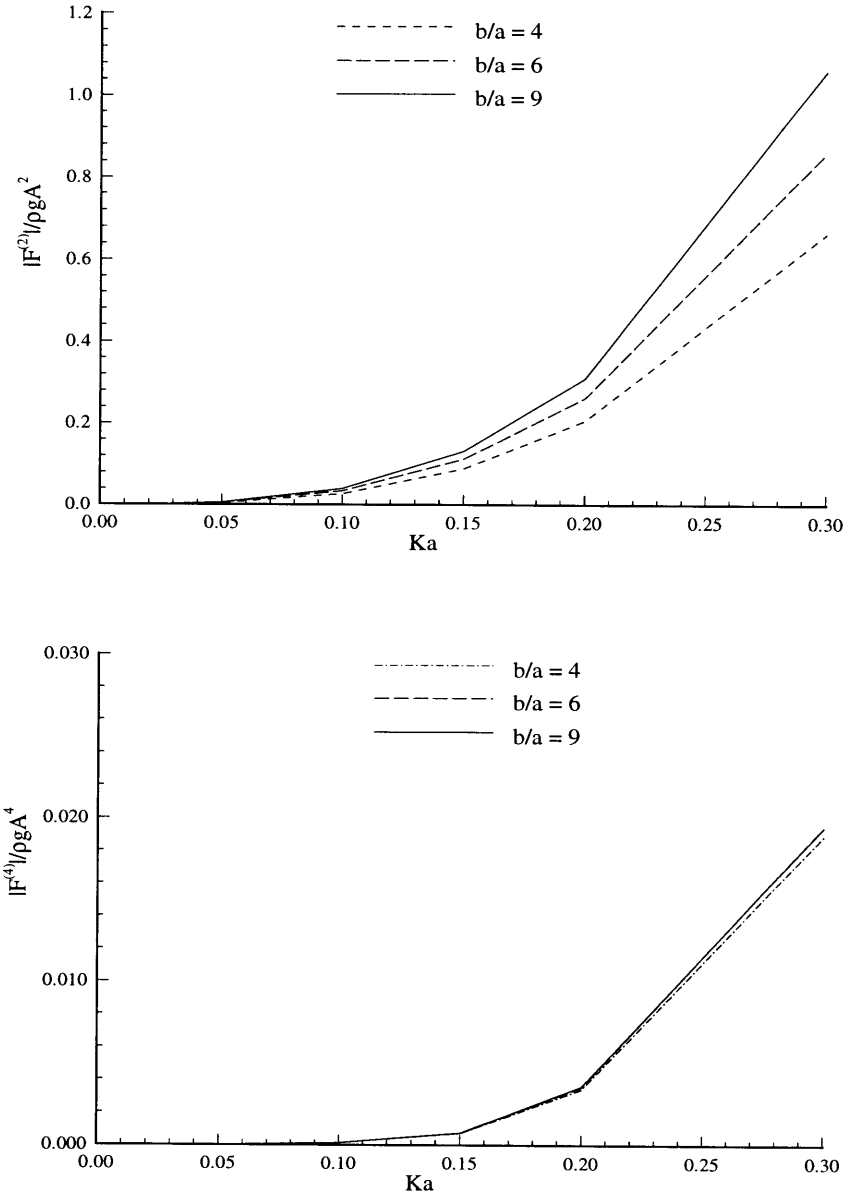

Figure 5-10: The numerical results of $F^{(2)}$ and $F^{(4)}$ for different wavenumbers with different truncation radii b on the free surface.

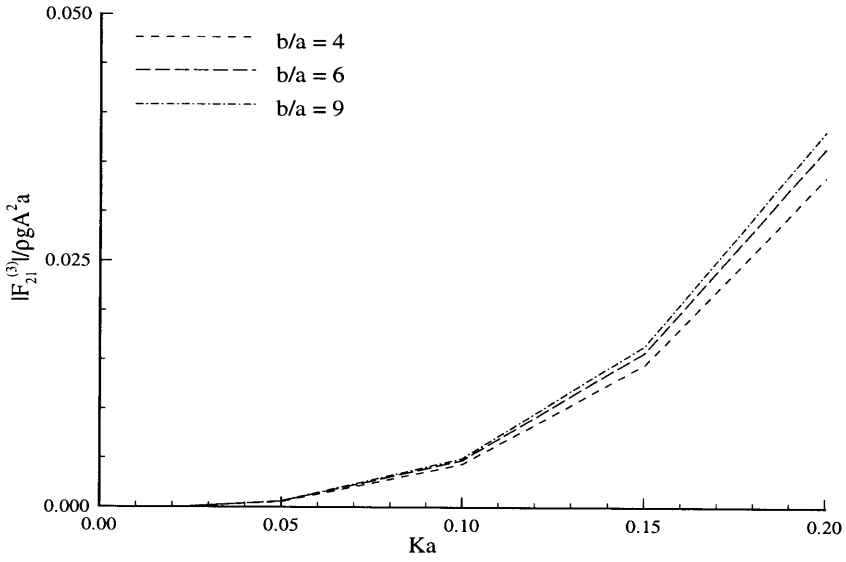

Figure 5-11: The numerical results of $F_{21}^{(3)}$ for different wavenumbers with different truncation radii on the free surface.

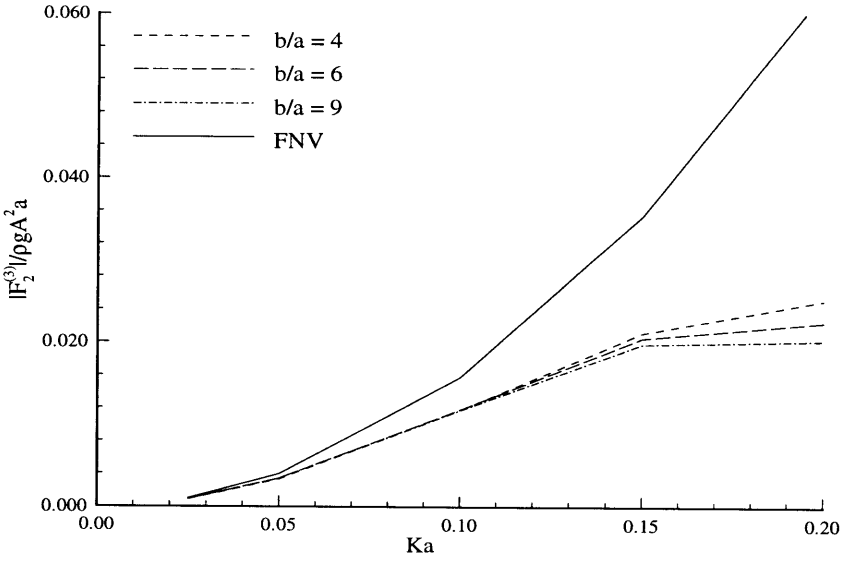

Figure 5-12: The numerical results of $F_2^{(3)}$ for different wavenumbers with different truncation radii on the free surface.

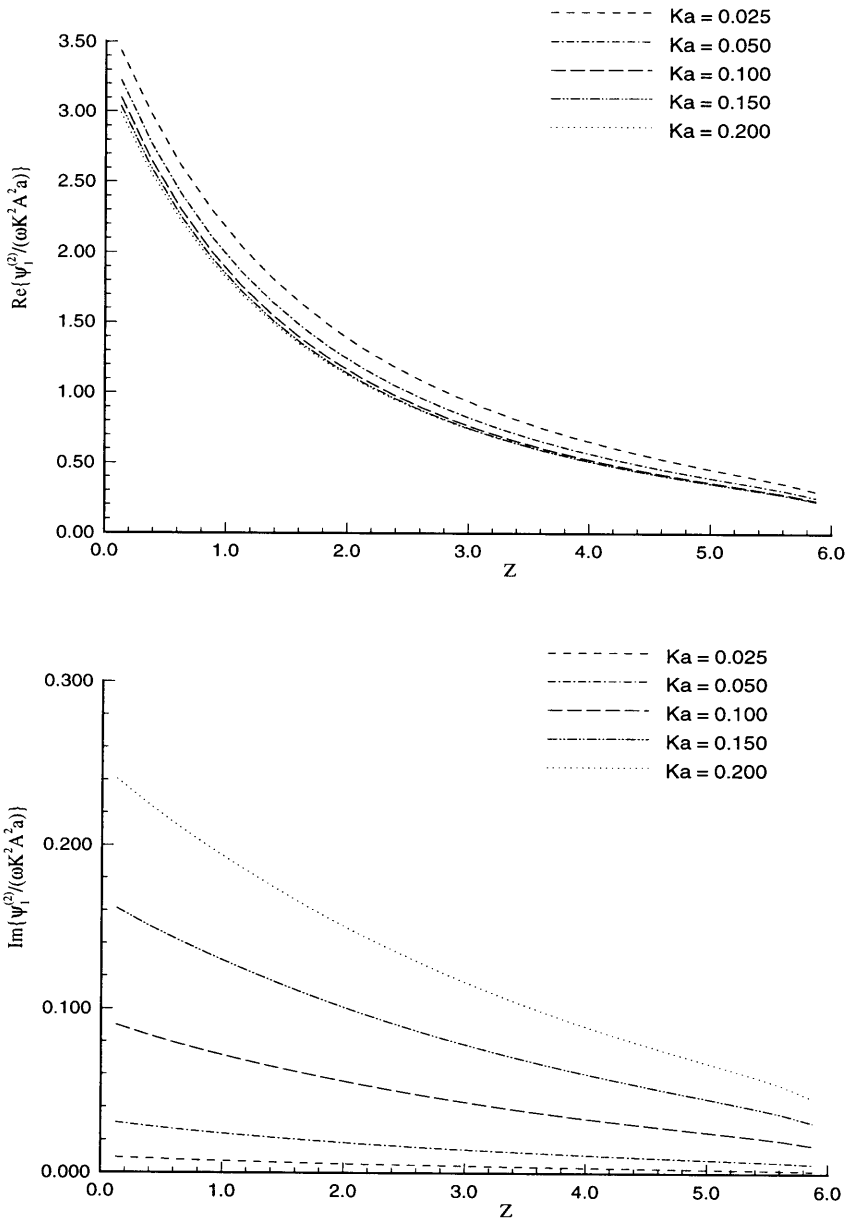

Figure 5-13: The real and imaginary parts of $\Psi_1^{(2)}$ as functions of Z for different wavenumbers.

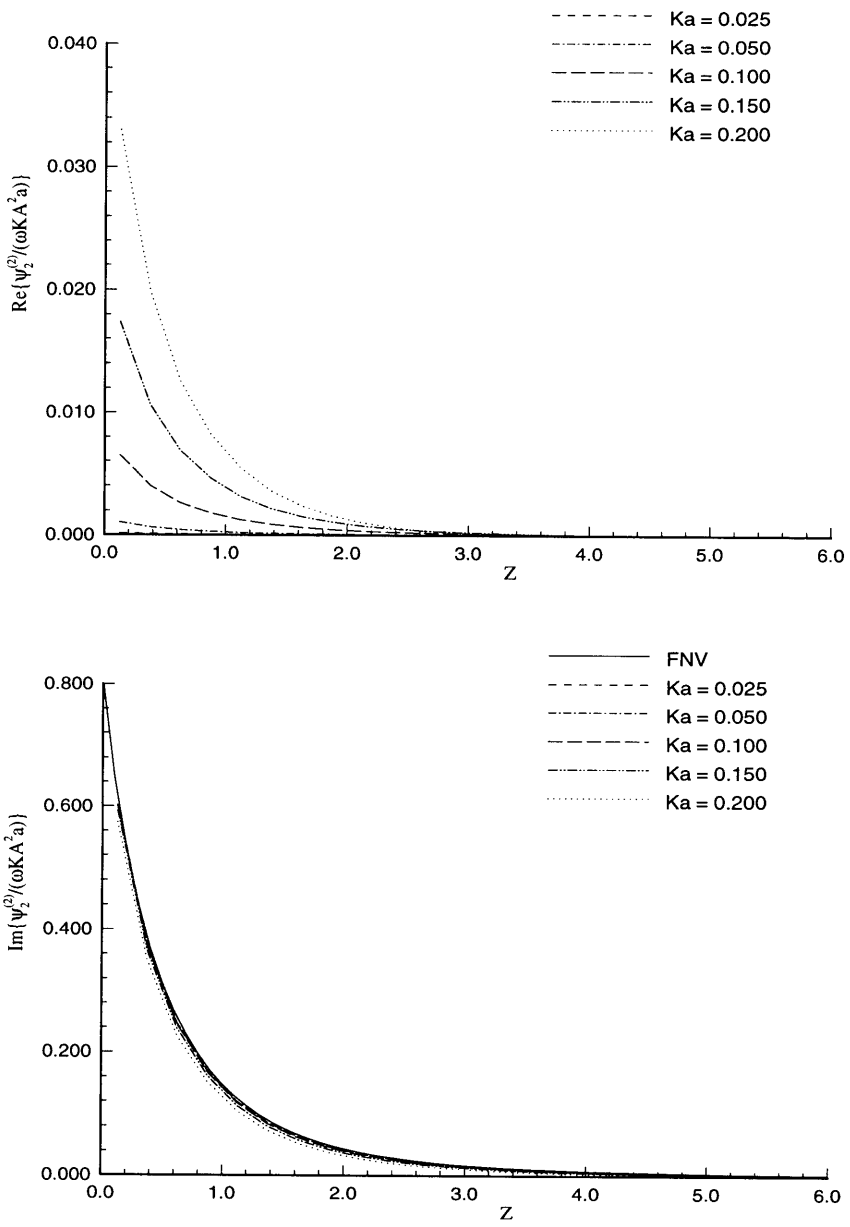

Figure 5-14: The real and imaginary parts of $\Psi_2^{(2)}$ as functions of Z for different wavenumbers.

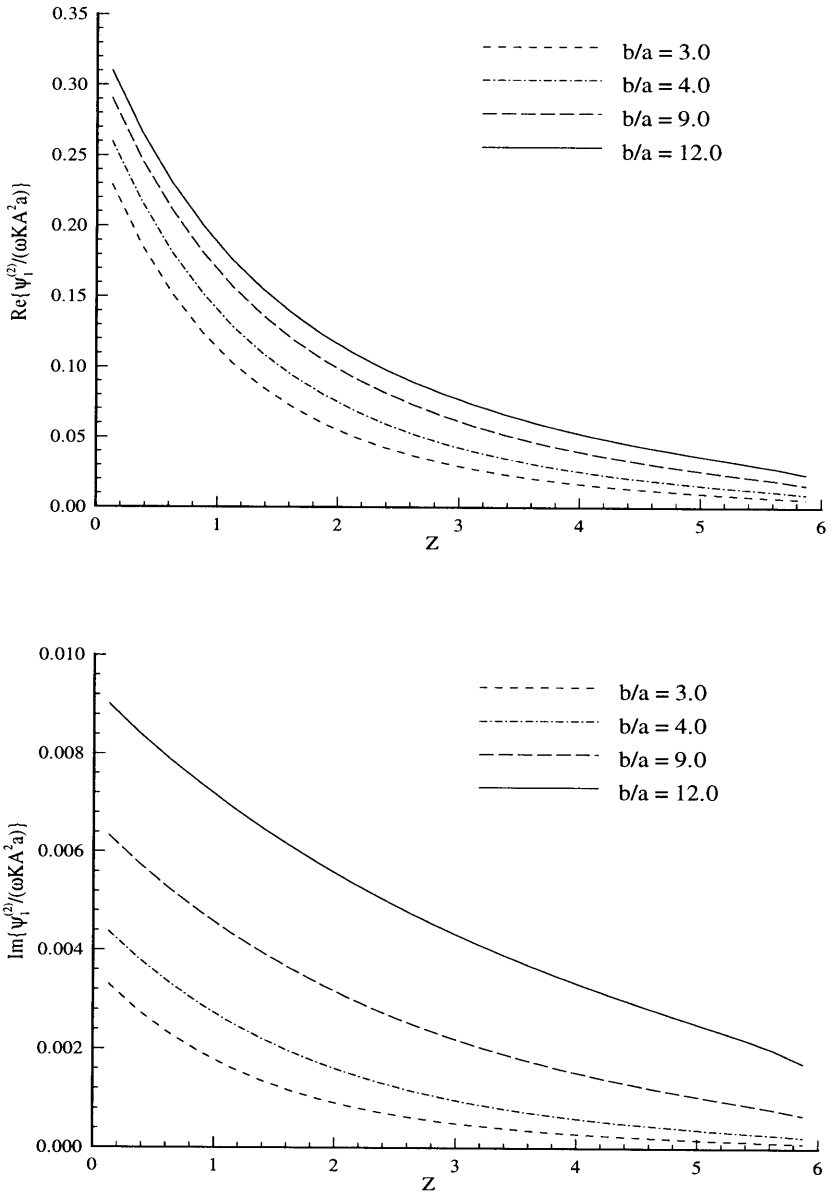

Figure 5-15: The real and imaginary parts of $\Psi_1^{(2)}$ as functions of Z. The results are obtained for $Ka = 0.1$ at different truncation radii.

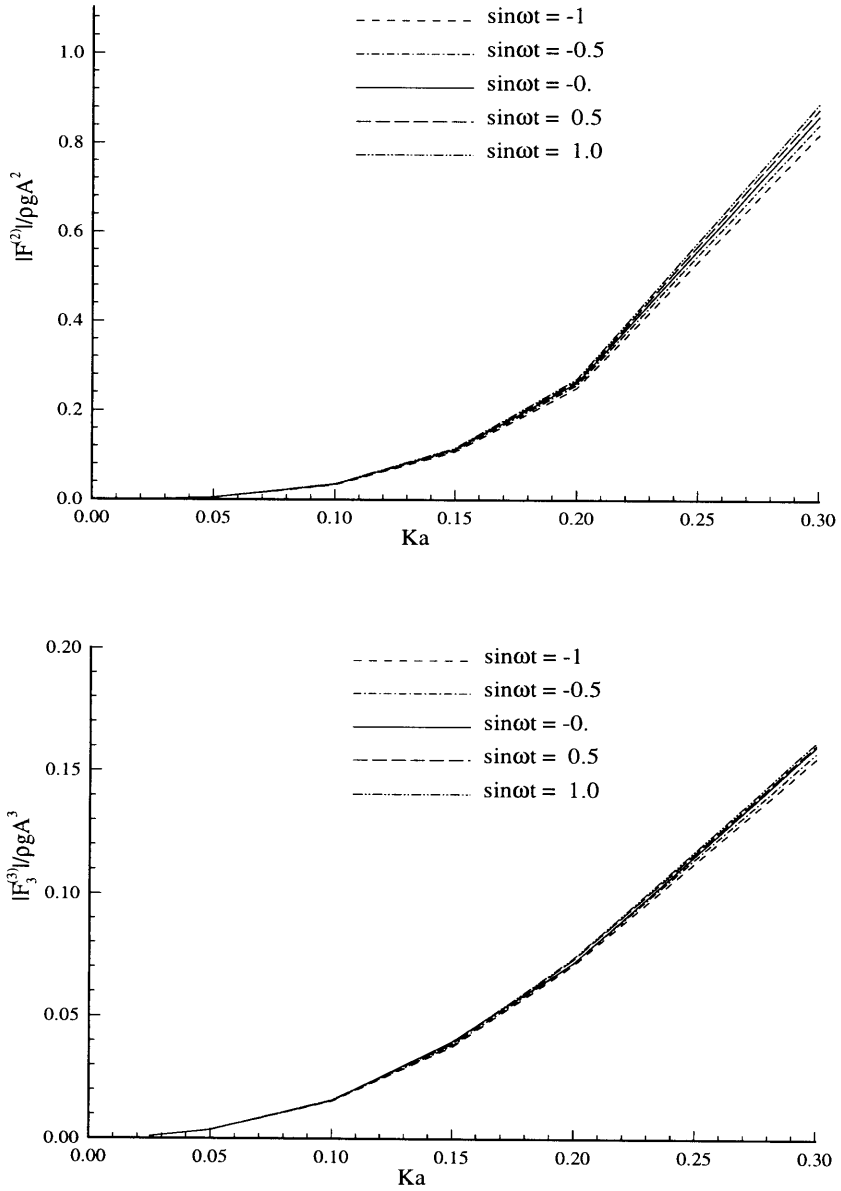

Figure 5-16: The modulus of $F^{(2)}$ (top figure) and $F_3^{(3)}$ (bottom figure) for different time steps within one wave period.

5.1.3 Results for an Array of Four Cylinders

This section presents numerical results for an array of four symmetric cylinders. For each cylinder, the radius is a and the draft is $T = 6a$. The centers of the cylinders are at $(\pm 4a, \pm 4a, 0)$ symmetric to the origin. Figure 5-17 illustrates the computational domain of the body surface and the free surface. The free surface is truncated at $b = 14a$. The free surface is the first-order wave elevation defined in equation (3.3, and the body surface is the instantaneous submerged body surface.

Figure 5-18 shows the discretization of the free surface, and 10 patches represent the truncated free surface. The free surface is discretized to ensure a structured grid on each patch, and to test the convergence by truncating the free surface at different radii. For the incoming wave propagating along the $+x$ axis, the free surface is symmetric about $y = 0$. We are able to use one plane of symmetry, with half of the complete surfaces discretized. The integral equation (3.25) is solved with the unknown potentials on the body surface as well as on the free surface.

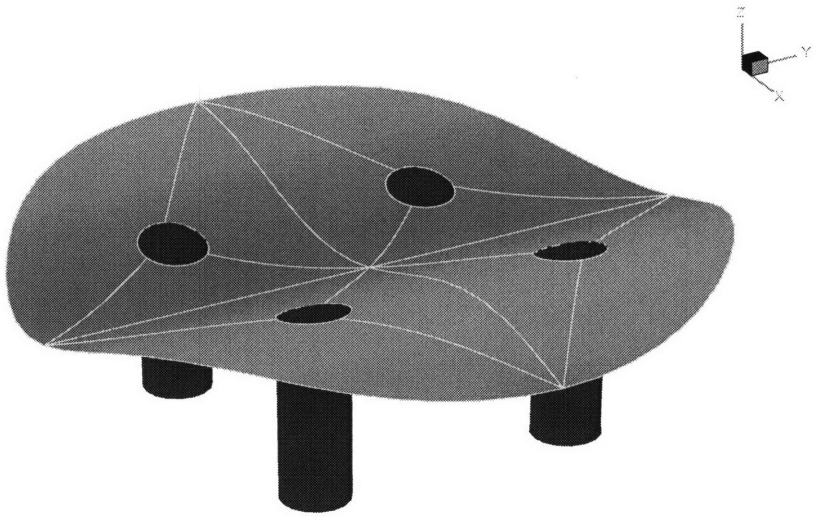

Figure 5-17: Perspective view of the inner free surface and four cylinders.

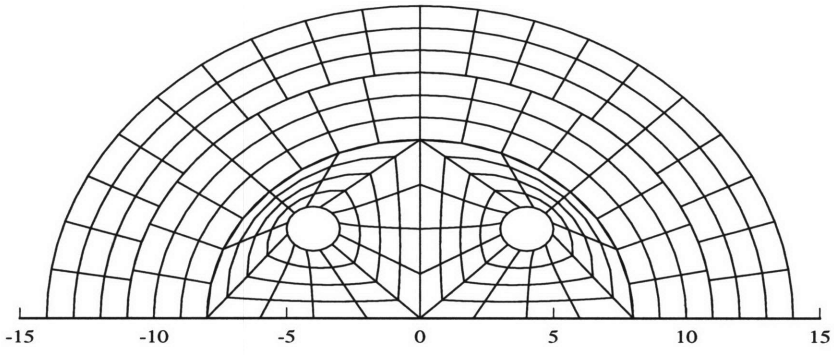

Figure 5-18: Discretization of the inner free surface

To test the interaction effects among these four cylinders just described, Table 5.3 shows the first- and third-harmonic wave loads acting on one single cylinder and these four cylinders for different wavenumbers. The geometry of the single cylinder is the same as each of the four cylinders. The second and fourth columns list the results for the single cylinder; the third and fifth columns list the total loads on the four cylinders, divided by 4 for comparison. Notice that the phase in incident waves are different for the four cylinders and one single cylinder, and the phase difference is accounted on these four cylinders in the table. The second and third columns are the first-order wave loads; the fourth and fifth columns are the third-harmonic wave loads. Compared to the single cylinder with center at the origin, the results on these four cylinder have a phase difference e^{-iKx}. The phase difference is accounted for the results in this table on these four cylinders. For the first-order force, the solution on the single cylinder and the on four cylinders do not have significant difference, which means that the interaction effects are not important. However, when $Ka \geq 0.1$, the third-harmonic solution on the single cylinder and on the four cylinders has large difference, which indicates that the interference effects among these cylinders are significant. Even in the low-frequency range, the interaction effects are important for the third-order solution for a TLP-type body according to the results from the table.

Ka	$\lvert F^{(1)}\rvert/\rho g A$	$\lvert F^{(1)}\rvert/4\rho g A$	$\lvert F_3^{(3)}\rvert/\rho g A^3$	$\lvert F_3^{(3)}\rvert/4\rho g A^3$
0.025	0.834	0.830	0.860E-03	1.010E-02
0.05	1.564	1.557	0.353E-02	0.384E-02
0.10	2.762	2.738	0.157E-01	0.372E-01
0.15	3.687	3.593	0.401E-01	0.371E+00
0.20	4.398	4.187	0.717E-01	0.430E+00

Table 5.3: The first- and third-harmonic horizontal forces acting on the single cylinder (columns 2 and 4) and the four cylinders (columns 3 and 5).

Figures 5-19 to 5-22 show the wave loads defined in equations (3.27), (3.28) and (3.29). The numerical results are obtained by truncating the free surface at $b/a = 8, 11, 14$ respectively for the integral over the free surface. Except for $F^{(2)}$, the other wave loads converge for $Ka \leq 0.2$ by truncating the free surface at $b/a = 8$.

The truncation radius is about the same as the distance of the diagonally opposite cylinders. As discussed in §5.1.2, the far-field contribution is important for $F^{(2)}$ in the single cylinder case, and the numerical results in Figure 5-19 suggest it is also important for the four cylinders. As shown in Figure 5-20, the far-field contribution for the third-harmonic forces due to the second-harmonic potential is less important. Figures 5-23 and 5-24 shows the nonlinear wave loads obtained within one wave period for $Ka = 0.15$. The results do not change significantly at different time steps.

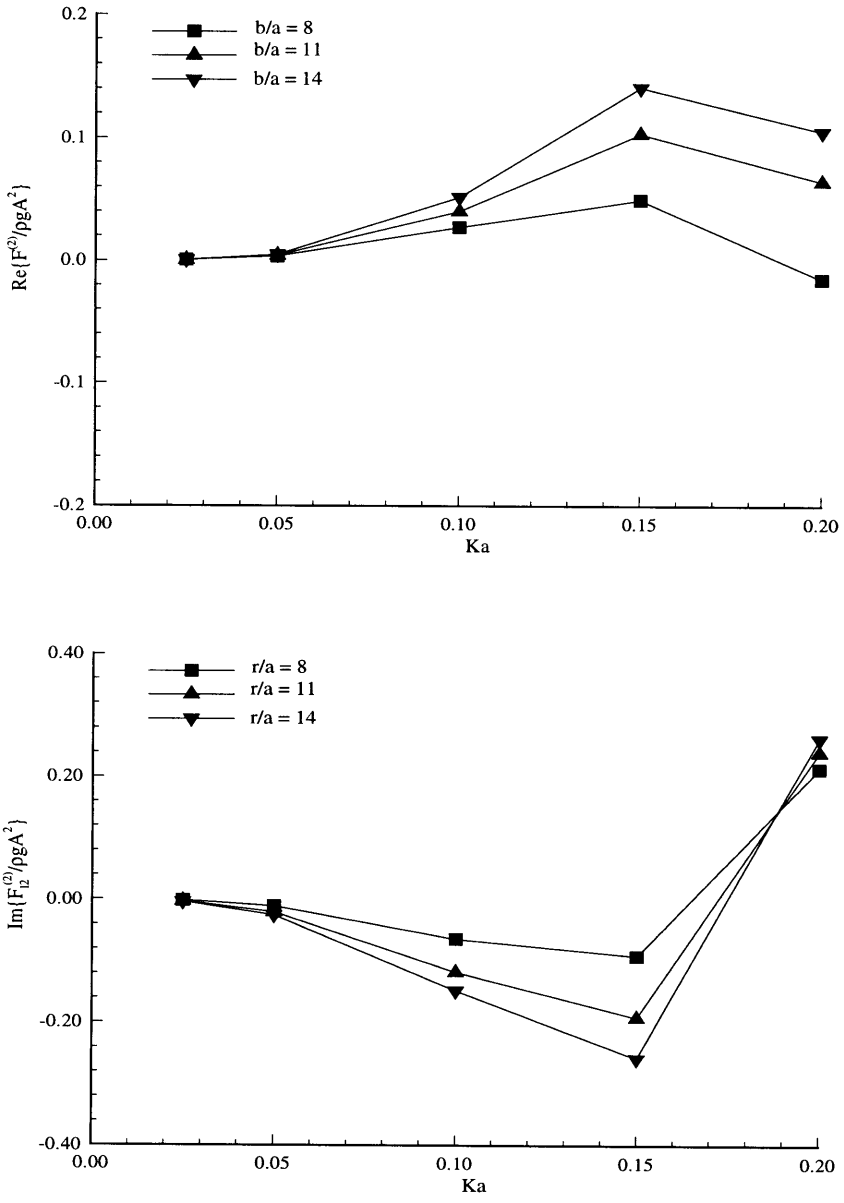

Figure 5-19: The real and imaginary parts of $F^{(2)}$ for the four cylinders.

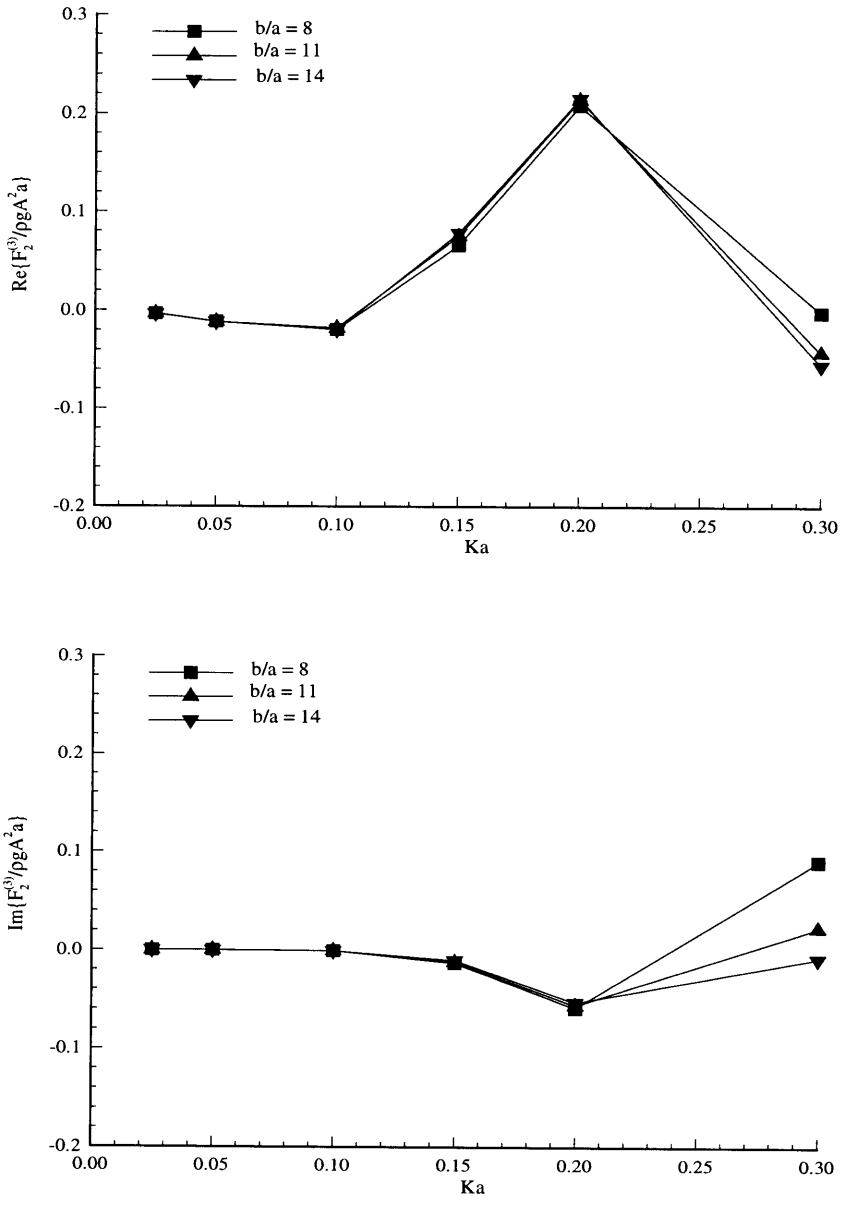

Figure 5-20: The real and imaginary parts of $F_2^{(3)}$ for the four cylinders.

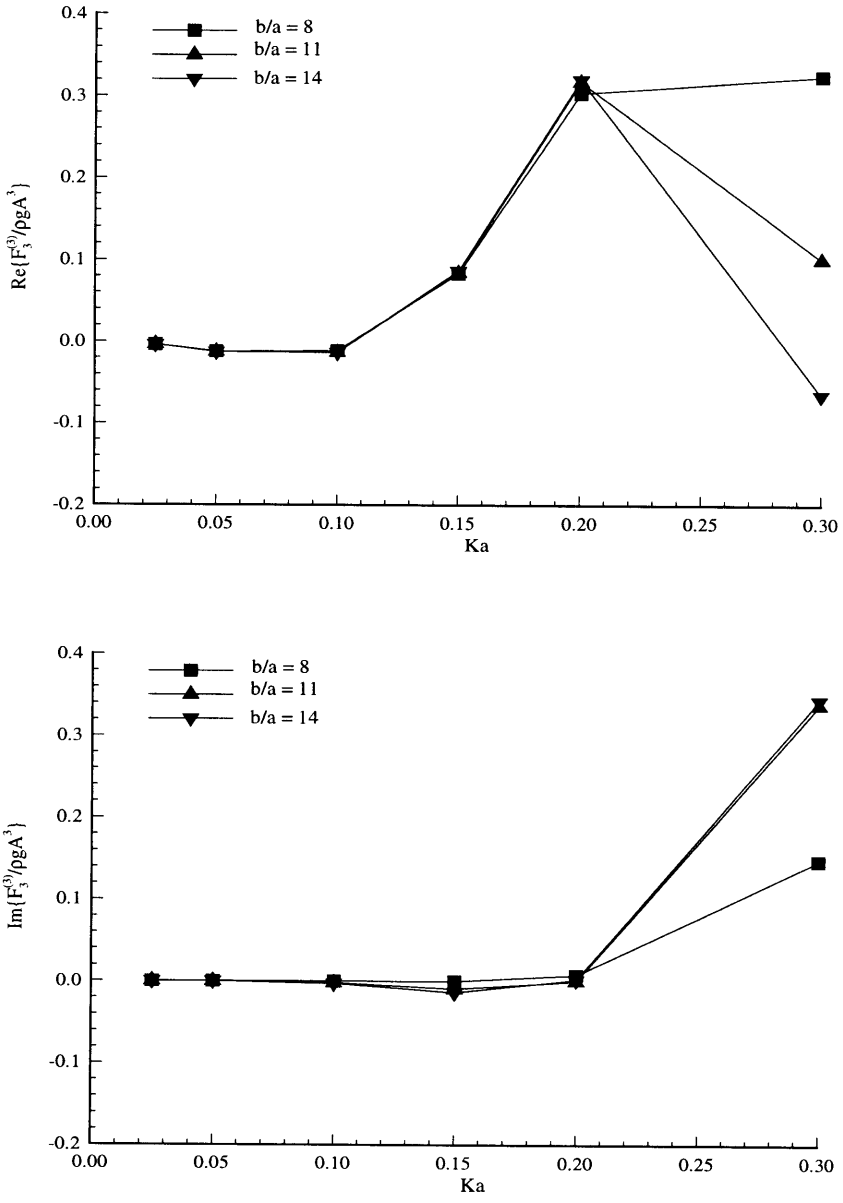

Figure 5-21: The real and imaginary parts of $F_3^{(3)}$ for the four cylinders.

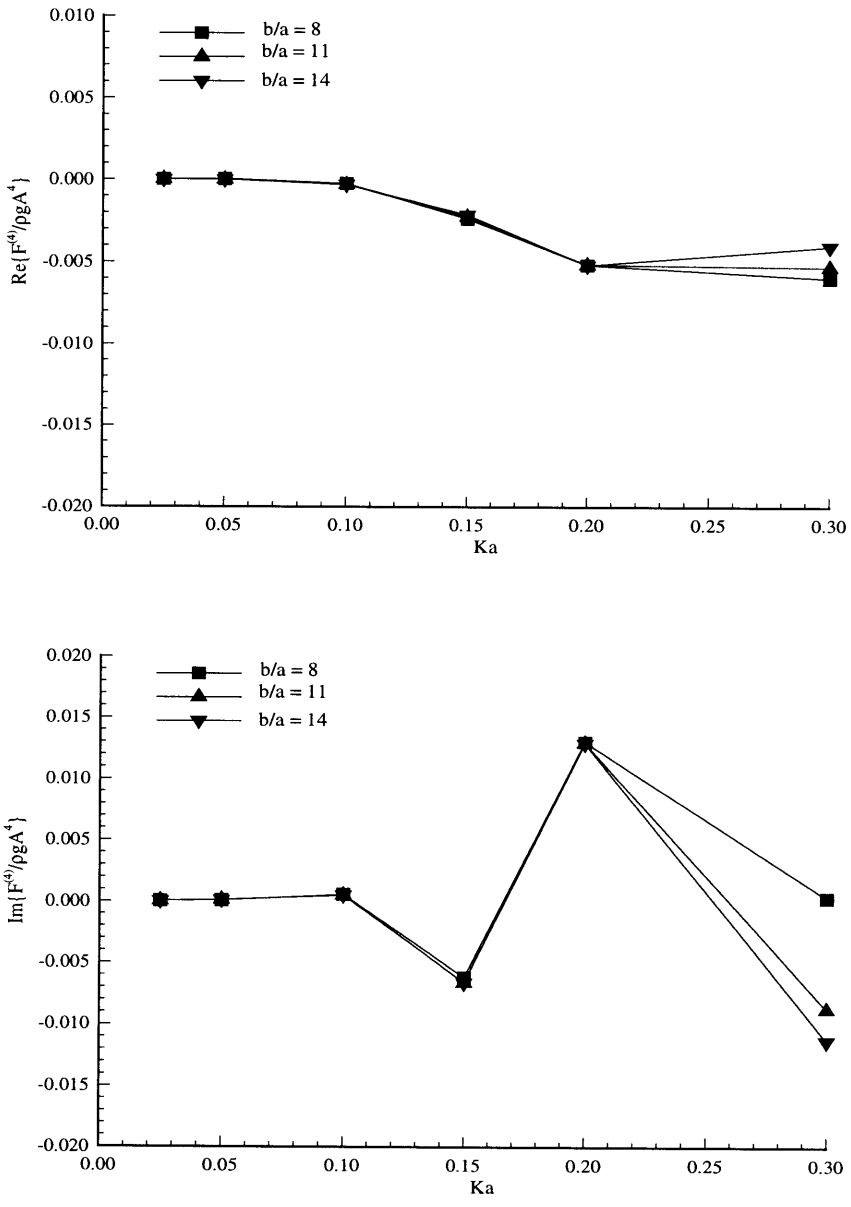

Figure 5-22: The real and imaginary parts of $F_3^{(4)}$ for the four cylinders.

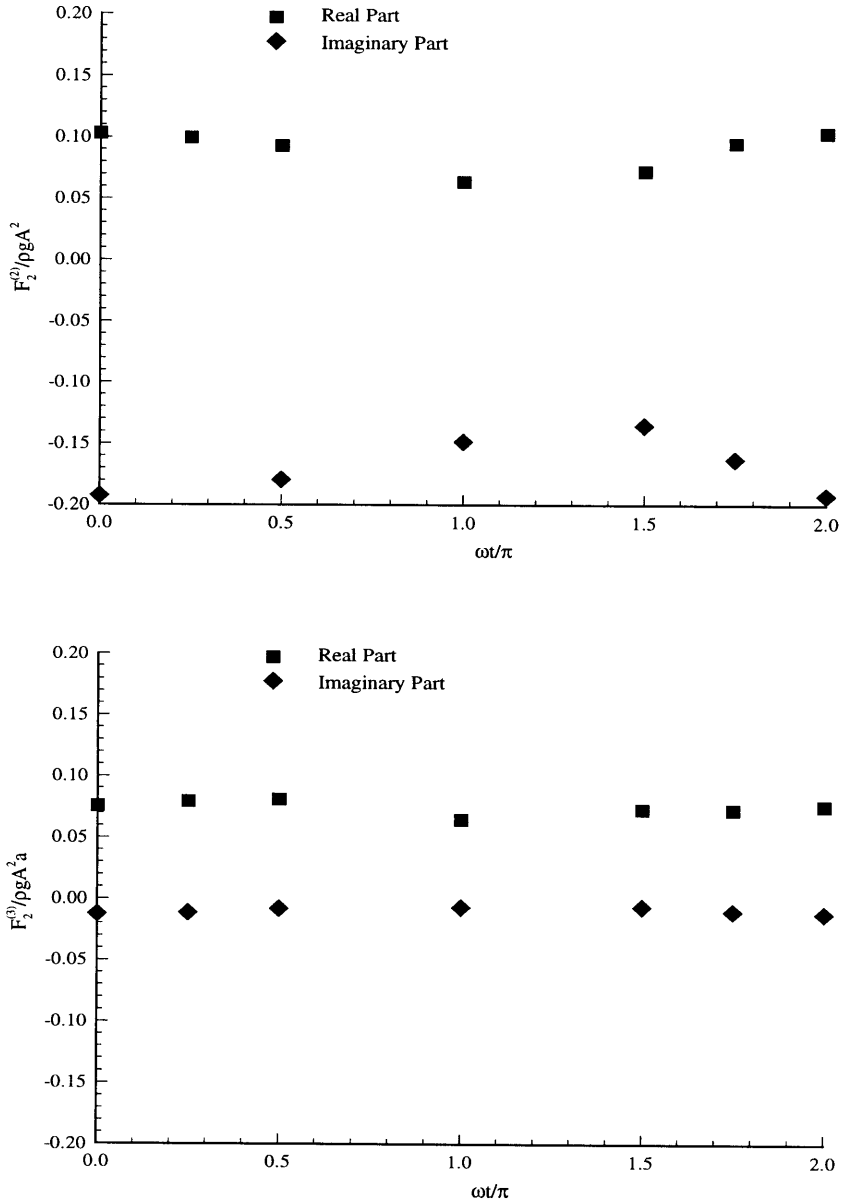

Figure 5-23: The results of $F_2^{(2)}$ and $F_2^{(3)}$ for the four cylinders computed at different times within one wave period for $Ka = 0.15$. The solution is obtained by truncating the free surface at $b = 11a$.

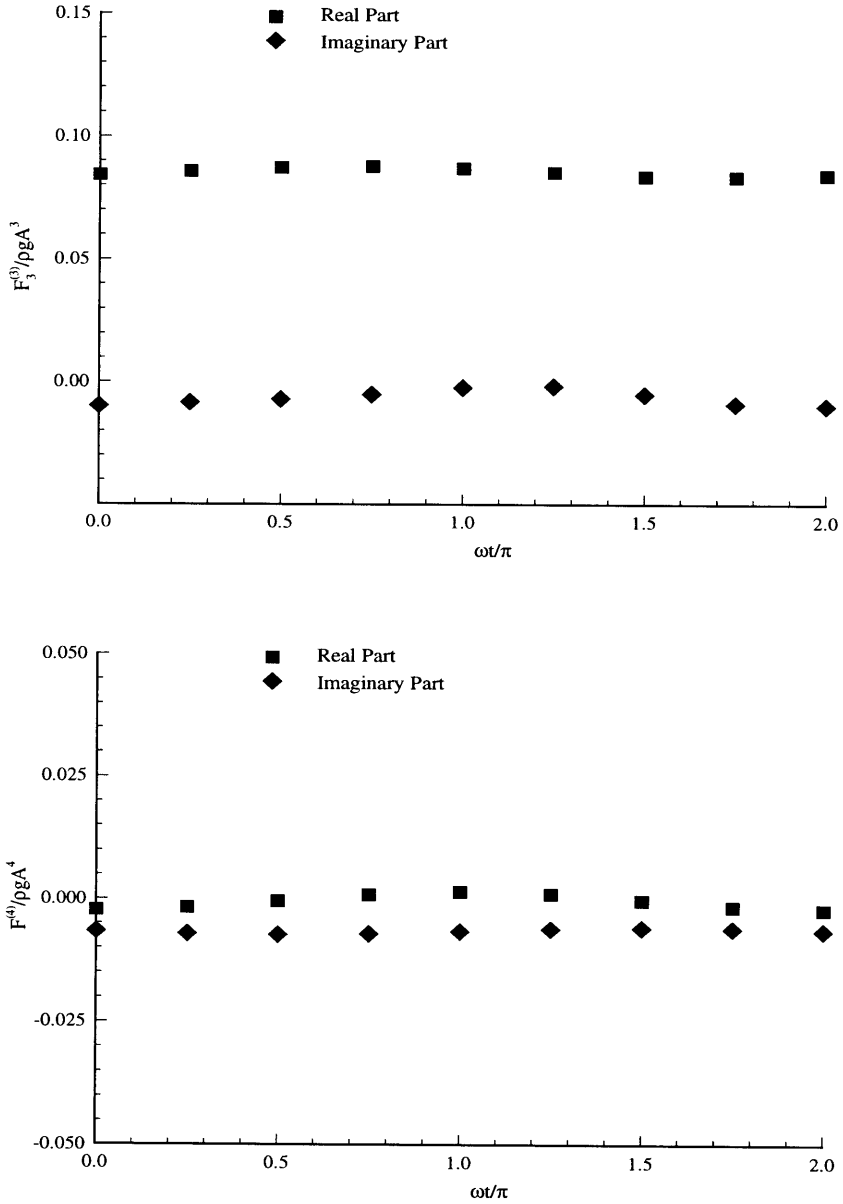

Figure 5-24: The results of $F_3^{(3)}$ and $F_3^{(4)}$ for the four cylinders computed at different times within one wave period for $Ka = 0.15$. The solution is obtained by truncating the free surface at $b = 11a$.

5.2 Results of Conventional Perturbation Theory

In this section, numerical results are obtained for the truncated cylinder with radius a and draft $T = 6a$. As discussed in Chapter 4, we neglect the far field contribution in the forcing function, and we also neglect the second-order potential contribution to the third-order forcing function.

5.2.1 Second-Order Results

To test the computational efficiency of the higher-order panel method, the results of second-order horizontal force due to the second-order potential computed from two kinds of the numerical methods are listed in Table 5.4. The free-surface integration in equation (3.39) is truncated at $b = 6a$. For the two B-spline discretizations with $\tilde{k} = 4, k = 4$, the results agree with each other to the fourth decimal place. For the three discretizations of the low-order panel method, the numerical results converge slowly to the results from the higher-order panel method. The discretization in the fifth column in the table has hundreds of time more panels than that of the second column. Even so, the numerical results from these columns imply that much more panels are required in the low-order panel method in order to achieve the same accuracy as listed in the table in the higher-order panel method.

From the analysis of Newman [34], in the conventional perturbation regime, the forcing function persists over the far field for the second-order problem, and the pressure is inversely proportional to the depth. Figure 5-25 illustrates the importance of the far-field contribution to the horizontal forces. In WAMIT, for the conventional perturbation second-order solution, the near-field ($r < b$) and the far-field ($r > b$) integrals are computed separately in equation (3.43). Figure 5-25 shows the ratio of the second-order force from the far-field contribution and the total second-order force. The far-field contribution becomes smaller when the truncation radius is increased. However, even when the free surface is truncated at $b = 118a$, the far-field contribution to the total force is still about 15%. Figure 5-26 shows the second-order force computed from the higher-order panel method with the truncated free surface,

	higher-order panel method		low-order panel method		
N_b	96	160	768	2688	9984
N_f	86	134	1920	7680	30720
Ka	$\Re\{F_2^{(2)}/\rho g A^2\}$		$\Re\{F_2^{(2)}/\rho g A^2\}$		
0.10	-0.07969	-0.07969	-0.0718	-0.0760	-0.0783
0.15	-0.32143	-0.32145	-0.2968	-0.3107	-0.3177
0.20	-0.47781	-0.47778	-0.4283	-0.4568	-0.4699
Ka	$\Im\{F_2^{(2)}/\rho g A^2\}$		$\Im\{F_2^{(2)}/\rho g A^2\}$		
0.10	-0.05968	-0.05967	-0.0315	-0.0460	-0.0532
0.15	0.00932	0.00931	0.0563	0.0321	0.0208
0.20	0.36915	0.36921	0.4244	0.3946	0.3811

Table 5.4: The second-order horizontal forces as computed by two kinds of numerical methods. The top half is the real part, and the bottom half is the imaginary part. N_b denotes the number of panels on the body, and N_f denotes the number of panels on the free surface.

and the importance of the far-field integral is apparent for $Ka > 0.15$.

5.2.2 Third-Order Results

Figure 5-27 shows the real and imaginary parts of $F_1^{(3)}$, the third-order force due to the first-order potential as defined in equation (3.45). The force is obtained by integrating the triple product of the first-order potential along the waterline. In the figure, 3×8 panels are used on one quadrant of the body with $\tilde{k} = 4, k = 4$. The result from MM and FNV are also plotted in the figure. The result from MM is obtained for a bottom mounted cylinder in a finite water depth H with $KH = 8$. The depth is considered to be sufficiently large so that the finite depth effect is not significant. The numerical results agree with the MM results. The result derived by FNV compares well with the result from the conventional perturbation theory for $KA < 0.2$. Thus, to calculate the third-order force due to the first-order potential, both the long-wave approximation theory and the conventional perturbation theory are appropriate in the low frequency range. It should be noted that the magnitudes of the total third-harmonic wave loads from FNV and from MM agree with each other except for the phase difference.

Figure 5-28 shows the numerical third-order force due to the third-order potential. Compared to Figure 5-26, the third-order force converges more rapidly than the second-order force for $Ka \leq 0.15$ when increasing the radius of the truncation radius on the free surface. The far-field integral appears to be less important in the third-order calculation compared to the second-order calculation.

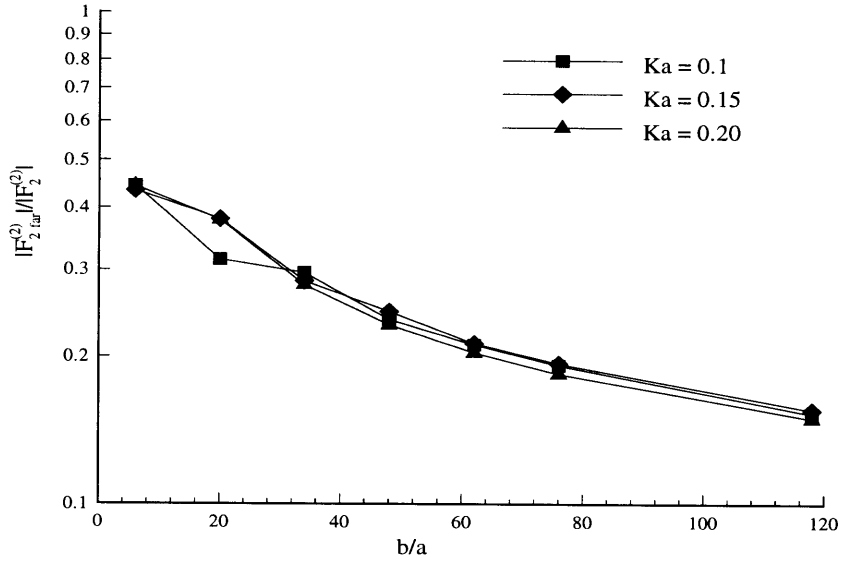

Figure 5-25: The ratio of the second-order force due to the far field contribution and the complete second-order force. The far-field force is denoted by $F_{2\text{far}}^{(2)}$. The results are obtained at three different wavenumbers from WAMIT.

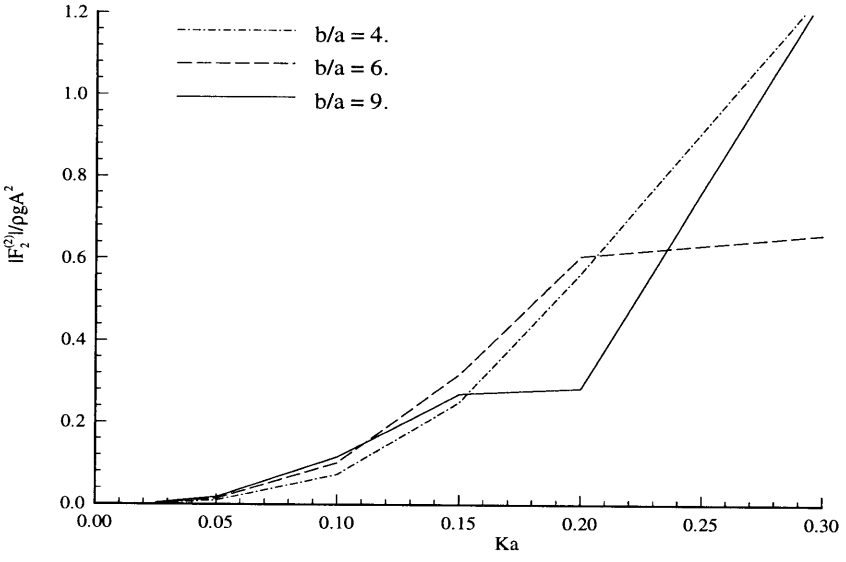

Figure 5-26: The modulus of the second-order force from the higher-order panel method evaluated at different truncation radii on the free surface.

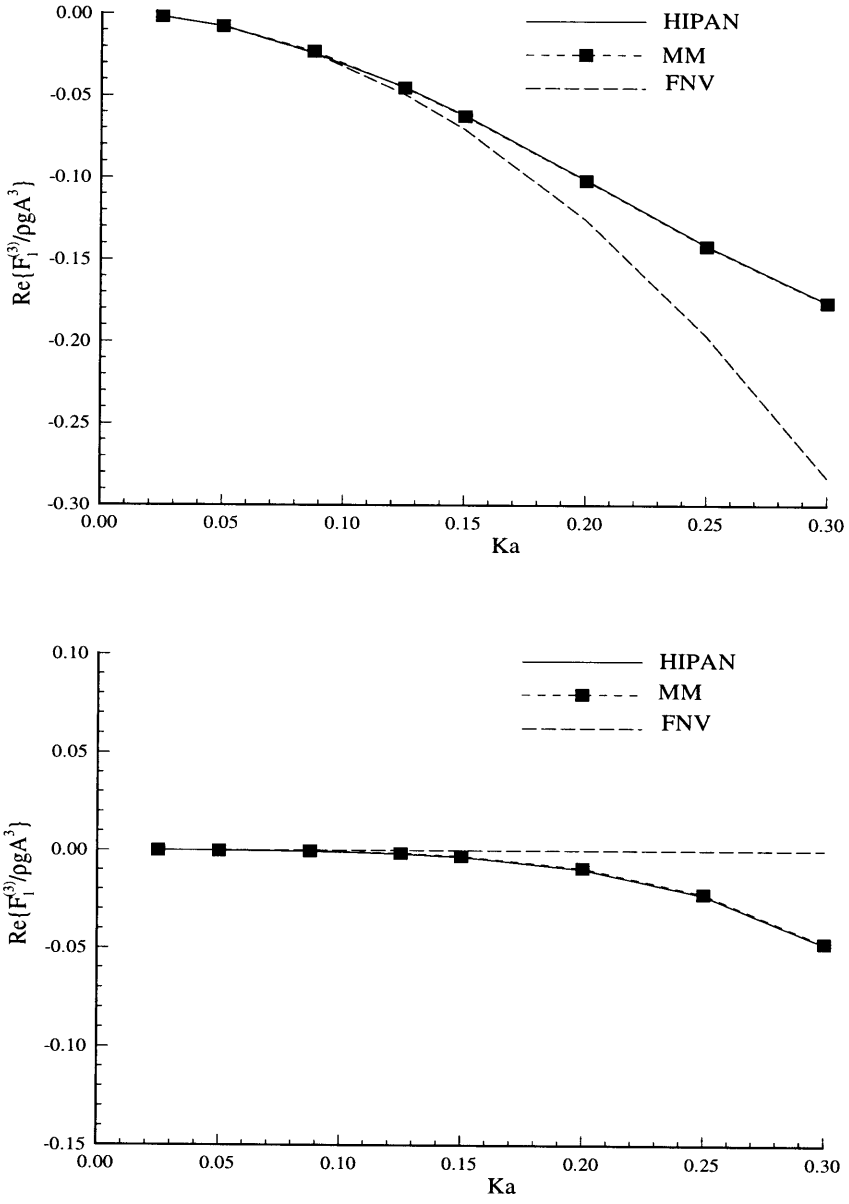

Figure 5-27: The real and imaginary parts of $F_1^{(3)}$ from the higher-order panel method, and the results of MM and FNV.

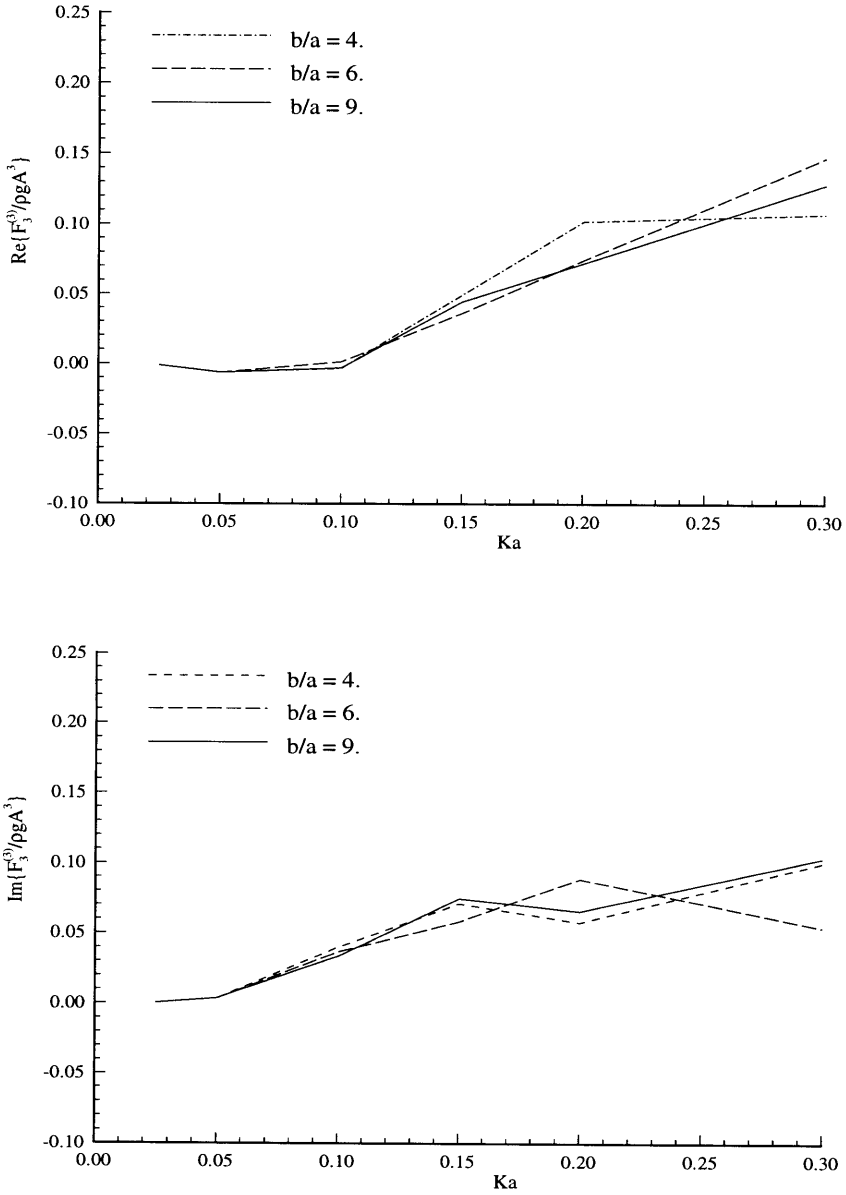

Figure 5-28: The real and imaginary parts of $F_3^{(3)}$ from the higher-order panel method evaluated at different truncation radii on the free surface. $k = 4, k = 4$ are used in the calculation.

Chapter 6

Discussion and Conclusions

In this thesis, the third-harmonic diffraction problems have been solved for general bodies to provide a basis for investigating the ringing phenomenon. Both the long-wave approximation theory and the conventional perturbation theory are investigated. A three-dimensional higher-order panel method using B-splines is used to solve the integral equations derived from these two theories.

The traditional low-order panel method has some fundamental numerical difficulties to solve these nonlinear problems. In this thesis, a higher-order panel method based on B-splines is adopted to solve these problems. In this method, the geometry and the potential are represented by B-splines. The use of a differentiable B–spline for the potential enables the derivatives of the potential to be calculated in a straightforward and robust way. The first-order potential is evaluated pointwise on the free surface from the solution of the potential on the body. A least square fit is used to obtain the B-spline form of the first-order potential on the free surface and the B-spline form of the forcing function. The integral equations of the nonlinear potentials are solved by a Galerkin procedure. For nonlinear problems, the higher-order panel method achieves the same accuracy with at least 100 times less unknowns than that in the low-order panel method In addition, this higher-order panel method overcomes the significant local error of the forcing function close to the waterline, as well as the local error of the derivatives of the nonlinear potential on the body close to the waterline appeared in the low-order panel method.

For the long-wave approximation theory, the inhomogeneous Neumann free surface condition is satisfied on the moving first-order wave elevation. The Green function $1/r + 1/r'$ is used in the integral equations for the nonlinear potentials. For a body with a single vertical column, the local free surface is the moving horizontal free surface, so the integral equation (3.23) has an integral over the free surface on the right-hand side. For a body with multiple columns, the free surface is the moving surface with a wave slope, so the integral equation (3.25) has an integral over the free surface on both the left-hand side and on the right-hand side. Both the second- and third-harmonic potentials are of the same order in this theory.

The convergence of the numerical results has been demonstrated, and the error is reduced when the number of unknowns in the linear system is increased. Also, the numerical results of a single cylinder converge to the FNV results by increasing the draft of the cylinder or decreasing the wavenumber. The numerical results are obtained at a set of time steps within one wave period, and the results do not change significantly at different time steps within one wave period.

Due to the localized forcing function assumption, the free surface is truncated at some distance away from the body, and the far-field contribution is neglected. The truncation radius is determined numerically. For a single cylinder, satisfactory convergence of the third-harmonic potential is achieved by truncating the free surface at a radius several times larger than the cylinder radius. The nonlinear wave loads due to the third-harmonic potential are consistent with the FNV analysis for $Ka < 0.2$. The fourth-harmonic force due to the third-harmonic potential is small as predicted by FNV.

A correction is derived for the second-harmonic forcing function in FNV analysis for the infinitely deep cylinder. This correction is inconsistent with the asymptotic expansion method, since this term is of higher order compared to the leading-order terms in the forcing function due to an extra Ka factor. However, this correction is useful in certain applications. In the numerical calculation, for the right-hand side of equation (3.23), the contribution from this term behaves like a logarithm along the radial direction, so the far-field contribution from this term is important when

wavenumber is not small. The numerical result of a truncated cylinder is consistent with the analysis in Appendix C. The results for the second-harmonic potential do not converge by truncating the free surface at some finite radius, and this force becomes significant when $Ka > 0.1$ due to the contribution of this term. Also, the total numerical third-harmonic force differs from the FNV results when $Ka > 0.1$ due to the contribution of this term. To include the far-field contribution, some further analysis and computation are required.

For applications to TLPs, we also compute the wave loads of an array of four symmetric cylinders using the long-wave approximation theory. The third-harmonic wave load converges by truncating the free surface at a radius about the same as the distance between diagonally opposite cylinders, although this is not true for the second-harmonic wave load due to the second-harmonic potential. The third-harmonic wave load acting on each one of the four cylinders is about the same as the same load on only one single cylinder for small wavenumber. When $Ka > 0.1$, however, the results of the third-harmonic wave loads begin to differ, which indicates that the diffraction interaction among the cylinders is significant, even though the interaction effects are no significant for the first-order solution. Thus, a numerical method is essential to obtain the nonlinear wave loads of TLPs.

The third-order problem based on the conventional perturbation theory is also solved in this thesis. We use the free-surface Green function in the integral equations. From the arguments of long waves, we neglect two contributions in the numerical computation: the far-field integration over the free surface, and the second-order potential contribution to the third-order forcing function. The third-order wave loads due to the first-order potential agree with the FNV results for $Ka < 0.2$. But the other nonlinear wave loads are different from the ones obtained by the long-wave approximation theory. In the low-frequency range, the third-order results converge more rapidly than the second-order results when the truncation radius on the free surface is increased, so the far-field contribution in the third-order wave loads might not be as important as in the second-order wave loads.

Overall, a numerical solution for predicting the third-harmonic wave loads has

been developed for a general body. Both the long-wave approximation theory and the perturbation theory are investigated using this method. The numerical results demonstrate that this higher-order panel method overcomes the numerical deficiencies in the low-order panel method, and higher-order panel method is efficient and robust in solving the nonlinear problems.

The integral equations for the two theories are different due to the different assumptions and the different boundary conditions. Therefore, it is not surprising that the numerical results from the two theories are not comparable to each other.

To solve the third-order problem outside of the long-wavelength range, the conventional perturbation theory should be used. For the free-surface integration, the free surface can be divided into three regions as in WAMIT, separated by two circles of different radii. In the inner region, the free-surface integration can be evaluated in the same way as presented in this thesis. In the intermediate region, the numerical schemes used in [24] can be adopted. In the outer region of the free surface, the far-field integration of the quadratic product of the first-order potential in the forcing function can be approximated in the same way as in WAMIT [23]. The far field integration of the triple product of the first-order potential can be analyzed similarly for the integral of the third-order forcing function. It might be difficult to find the analytical expression for the second-order potential in the far field, thus the integral of the second-order potential over the free surface might have to be evaluated numerically.

Ferrant [13] has developed a fully nonlinear code, and his results for the third-harmonic wave loads agree reasonably well with those of MM for a bottom mounted cylinder. In his calculation, $KH = 8$ is fixed, and the radius of the cylinder changes to keep K constant. KA is kept to be 0.06, $A/a = 0.6$ for $Ka = 0.1$, and $A/a = 0.3$ for $Ka = 0.2$. According to the parameters used in his calculation, it is difficult to draw the conclusion that his results should be in considered to be in the long-wave regime or in the conventional perturbation regime.

Another related application has been carried out by Krokstad *et al* [20]. They have modified the FNV theory and irregular waves analysis by Newman [37] to verify the experiments for two different cylinders. They find that the FNV model overpredicts

the second-harmonic wave loads, but the third-harmonic wave loads from FNV are close to the experimental results. Their conclusion indicates that the diffraction effect neglected in the FNV analysis for a slender body is important for the second-harmonic solution, which is consistent with our numerical results. Their comparison with experiments is improved by combining the second-harmonic wave loads from the conventional perturbation theory with the third-harmonic wave loads from the FNV theory. In our analysis and computational results, we found that the third-harmonic solution predicted by FNV is more accurate than the second-harmonic solution. It appears that their conclusion supports the conclusions in this thesis.

Eckhoff [6] has worked on the simulations by combining the complete second-order solution from WAMIT and the third-harmonic results of FNV theory for a three-column TLP, and his simulations are compared with the experiments done at MARINTEK. Additional experimental results for an array of four cylinders at MARINTEK [43] suggest that the interference effects are important in the second- and third-harmonic wave loads, which is consistent with the conclusions in this thesis.

Appendix A

Source Formulation

A.1 Integral Equation for the First-Order Potential

The velocity potential in the fluid can be expressed by a distribution of source strength σ over the body surface,

$$4\pi\phi(\mathbf{x}) = \iint_{S_b} \sigma(\xi) G(\mathbf{x}, \xi) dS, \tag{A.1}$$

where the free surface Green function G is defined in equation (2.16). As the field point $\mathbf{x}$ in the fluid approaches the body boundary, the normal derivative of the Green function is singular. Therefore, we have

$$4\pi \frac{\partial \phi(\mathbf{x})}{\partial n} = 2\pi\sigma(\mathbf{x}) + \iint_{S_b} \sigma(\xi) \frac{\partial G(\mathbf{x}, \xi)}{\partial n} dS \quad \mathbf{x} \in S_b. \tag{A.2}$$

The normal derivative of the potential on the left-hand side is known due to the body boundary condition, and the unknown source strength can be solved by a panel method.

Upon obtaining the source strength on the body, the velocity in the fluid can be

evaluated from the gradient of equation (A.1),

$$4\pi\nabla\phi(\mathbf{x}) = \iint_{S_b} \sigma(\xi)\nabla G(\mathbf{x},\xi)dS. \tag{A.3}$$

If using equation (2.20) to calculate the fluid velocity, one has to evaluate the integral of double derivatives of the Green function. The source formulation is preferred in order to avoid calculating numerical double derivatives of the Green function in the low-order panel method.

A.2 Integral Equation for the Nonlinear Potentials

We only derive the source formulation for the long-wave approximation method. Define the nonlinear potential $\Psi^{(i)}$ $(i = 2, 3)$ to be represented by a distribution of source strength $\sigma^{(i)}(i = 2, 3)$ over the submerged body surface and the free surface,

$$4\pi\Psi^{(i)}(\mathbf{x},t) = \iint_{S_b(t)} \sigma^{(i)}(\xi,t)G(\mathbf{x},\xi,t) + \iint_{S_Z(t)} \sigma^{(i)}(\xi,t)G(\mathbf{x},\xi,t)dS. \tag{A.4}$$

The free-surface integral is restricted to the inner domain close to the body, and the far-field contribution is neglected as discussed in Chapter 3. As the field point approaches the body or the free surface, the normal derivative of the Green function is singular, therefore

$$\begin{aligned} 4\pi\frac{\partial\phi^{(i)}(\mathbf{x},t)}{\partial n} &= 2\pi\sigma^{(i)}(\mathbf{x},t) + \iint_{S_b(t)} \sigma^{(i)}(\xi,t)\frac{\partial G(\mathbf{x},\xi,t)}{\partial n}dS \\ &+ \iint_{S_Z(t)} \sigma^{(i)}(\xi,t)\frac{\partial G(\mathbf{x},\xi,t)}{\partial n}dS, \qquad \mathbf{x}\in S_b, \end{aligned} \tag{A.5}$$

$$\begin{aligned} 4\pi\frac{\partial\phi^{(i)}(\mathbf{x},t)}{\partial n} &= 4\pi\sigma^{(i)}(\mathbf{x},t) + \iint_{S_b(t)} \sigma^{(i)}(\xi,t)\frac{\partial G(\mathbf{x},\xi,t)}{\partial n}dS \\ &+ \iint_{S_Z(t)} \sigma^{(i)}(\xi,t)\frac{\partial G(\mathbf{x},\xi,t)}{\partial n}dS, \qquad \mathbf{x}\in S_Z, \end{aligned} \tag{A.6}$$

where the factor 4π on the right-hand side of (A.6) is due to the fact that the normal derivatives of $1/r$ and $1/r'$ are both singular with the same sign when the field point

approaches the free surface.

For the long-wave approximation method, the left hand side in (A.5) is zero due to the diffraction boundary condition. The left hand side in (A.6) is the forcing function defined in equation (3.17), since the normal on the free surface can be approximated along the vertical z direction. The source strength of each order is obtained by solving the integral equations (A.5) and (A.6) together.

For a single truncated cylinder, equations (A.5) and (A.6) can be simplified. The local free surface S_Z is a horizontal surface, and $\partial G/\partial n = -\partial G/\partial Z = 0$ when the field point is on the free surface. Thus, the second and third terms on the right hand side of (A.6) vanish, and (A.6) becomes

$$\sigma^{(i)}(\mathbf{x}) = f^{(i)}(\mathbf{x}), \quad \mathbf{x} \in S_Z. \tag{A.7}$$

Substituting the source strength on the free surface into equation (A.6), we have

$$2\pi\sigma^{(i)}(\mathbf{x},t) + \iint_{S_b(t)} \sigma^{(i)}(\xi,t)\frac{\partial G(\mathbf{x},\xi,t)}{\partial n}dS \;=\; -\iint_{S_Z(t)} f^{(i)}(\xi)\frac{\partial G(\mathbf{x},\xi,t)}{\partial n}dS, \quad \mathbf{x} \in S_b.$$

After solving the above equation for the source strength on the body, the gradient of the nonlinear potential can be evaluated by

$$4\pi\nabla\Psi^{(i)}(\mathbf{x},t) = \iint_{S_b(t)} \sigma^{(i)}(\xi,t)\nabla G(\mathbf{x},\xi,t) + \iint_{S_Z(t)} \sigma^{(i)}(\xi,t)\nabla G(\mathbf{x},\xi,t)dS. \tag{A.8}$$

Appendix B

Derivatives on the Free Surface

B.1 First derivatives

A surface is defined in parametric space by

$$x = x(u,v), \quad y = y(u,v), \quad z = z(u,v), \tag{B.1}$$

where u, v are parametric variables on the surface. Define a position vector to the surface,

$$\mathbf{x} = x\mathbf{i} + y\mathbf{j} + z\mathbf{k}, \tag{B.2}$$

then, the tangent vectors are $\mathbf{x}_u, \mathbf{x}_v$. The vector $\mathbf{x}_u \times \mathbf{x}_v$ is normal to the surface. Thus, the unit normal $\mathbf{n}$ can be defined as

$$\mathbf{n} = \frac{\mathbf{x}_u \times \mathbf{x}_v}{H}, \tag{B.3}$$

where $H = |\mathbf{x}_u \times \mathbf{x}_v|$.

Let $\nabla_s u, \nabla_s v$ denote the set reciprocal to $\mathbf{x}_u, \mathbf{x}_v$, then

$$\nabla_s u = \frac{\mathbf{x}_v \times \mathbf{n}}{H} = \frac{1}{H^2}(G\mathbf{x}_u - F\mathbf{x}_v) \tag{B.4}$$

$$\nabla_s v = \frac{\mathbf{n} \times x_u}{H} = \frac{1}{H^2}(-F\mathbf{x}_u + E\mathbf{x}_v) \tag{B.5}$$

and E, F, G are the coefficients of the first fundamental form of the surface given by

$$\begin{aligned} E &= \mathbf{x}_u \cdot \mathbf{x}_u, \\ F &= \mathbf{x}_u \cdot \mathbf{x}_v, \\ G &= \mathbf{x}_v \cdot \mathbf{x}_v. \end{aligned}$$

For a differentiable function f, the derivative with respect to arc s along the surface is the following:

$$\frac{df}{ds} = \frac{\partial u}{\partial s}\frac{df}{du} + \frac{\partial v}{\partial s}\frac{df}{dv}. \tag{B.6}$$

If s is arc length along a curve in any direction, the unit tangent vector e to the curve is

$$\begin{aligned} \mathbf{e} &= \frac{d\mathbf{x}}{ds} \\ &= \mathbf{x}_u\frac{du}{ds} + \mathbf{x}_v\frac{dv}{ds} \end{aligned} \tag{B.7}$$

Therefore, $\nabla_s u \cdot \mathbf{e} = du/ds$, $\nabla_s v \cdot \mathbf{e} = dv/ds$. Equation (B.6) can be rewritten as

$$\frac{df}{ds} = \mathbf{e} \cdot (\nabla_s u\frac{\partial f}{\partial u} + \nabla_s v\frac{\partial f}{\partial v}). \tag{B.8}$$

Denote $\nabla_s f$ to be the surface gradient of f , thus

$$\begin{aligned} \nabla_s f &= \nabla_s u\frac{\partial f}{\partial u} + \nabla_s v\frac{\partial f}{\partial v} \\ &= \frac{1}{H^2}[\mathbf{x}_u(G\frac{\partial}{\partial u} - F\frac{\partial}{\partial v})f + \mathbf{x}_v(E\frac{\partial}{\partial v} - F\frac{\partial}{\partial u})f] \end{aligned} \tag{B.9}$$

For vector $\mathbf{f}$,

$$\nabla_s \cdot \mathbf{f} = \frac{1}{H^2}[\mathbf{x}_u(G\frac{\partial}{\partial u} - F\frac{\partial}{\partial v}) \cdot \mathbf{f} + \mathbf{x}_v(E\frac{\partial}{\partial v} - F\frac{\partial}{\partial u})\mathbf{f}] \tag{B.10}$$

The spatial gradient ∇ can be expressed as the sum of the surface gradient and the derivative in the direction to the surface ([2]),

$$\nabla f = \nabla_s f + \mathbf{n}\frac{\partial f}{\partial n}. \tag{B.11}$$

If f is the first-order potential on the free surface, $\partial f/\partial n = Kf$ due to the free surface condition.

B.2 Second Derivatives

Evaluating the forcing function on the free surface requires the evaluation of the second derivatives of the potential.

From equation (B.9), the gradient of ∇f can be written as

$$\nabla\nabla f = \nabla\nabla_s f + \mathbf{n}\frac{\partial \nabla f}{\partial n}, \tag{B.12}$$

where the left hand double gradient contains all the second derivative components.

For the first term on the right-hand side of above equation,

$$\nabla\nabla_s f = \nabla_s\nabla_s f + \mathbf{n}\frac{\partial \nabla_s f}{\partial n} \tag{B.13}$$

There is a tensor identity from Brand [3],

$$\mathbf{n} \cdot^2 \nabla\mathbf{f} - \mathbf{n}\nabla \cdot \mathbf{f} = \mathbf{n} \cdot^2 \nabla_s\mathbf{f} - \mathbf{n}\nabla_s \cdot \mathbf{f} \tag{B.14}$$

where the operation $\mathbf{n} \cdot^2 \nabla\mathbf{f}$ means $\mathbf{n}$ is to be dotted with the components of $\mathbf{f}$ after the gradient operation on the components of $\mathbf{f}$. The above identity can be proved in the following,

$$\begin{aligned} \mathbf{n} \cdot^2 \nabla\mathbf{f} &= \mathbf{n} \cdot^2 \{\nabla_s\mathbf{f} + \mathbf{n}\frac{\partial \mathbf{f}}{\partial n}\} \\ &= \mathbf{n} \cdot^2 \nabla_s\mathbf{f} + \mathbf{n}\{\frac{\partial \mathbf{f}}{\partial n} \cdot \mathbf{n}\}. \end{aligned} \tag{B.15}$$

Using the fact that

$$\nabla \cdot \mathbf{f} = \nabla_s \cdot \mathbf{f} + \mathbf{n} \cdot \frac{\partial \mathbf{f}}{\partial n}, \tag{B.16}$$

so,

$$\mathbf{n} \cdot^2 \nabla \mathbf{f} = \mathbf{n} \cdot^2 \nabla_s \mathbf{f} + \mathbf{n}(\nabla \cdot \mathbf{f} - \nabla_s \cdot \mathbf{f}). \tag{B.17}$$

In this way, tensor identity in equation (B.14) is proved.

Define the potential to be ϕ, and the velocity $\mathbf{f} = \nabla\phi$,

$$\mathbf{n}\nabla \cdot \mathbf{f} = (\mathbf{n} \cdot \nabla)\nabla\phi = \mathbf{n}\frac{\partial \nabla\phi}{\partial n}. \tag{B.18}$$

Since

$$\begin{aligned}(\mathbf{n} \cdot \nabla)\nabla\phi &= (n_x\frac{\partial}{\partial x} + n_y\frac{\partial}{\partial y} + n_z\frac{\partial}{\partial z})\nabla\phi \\ &= n_x\nabla\frac{\partial\phi}{\partial x} + n_y\nabla\frac{\partial\phi}{\partial y} + n_z\nabla\frac{\partial\phi}{\partial z})\nabla\phi \\ &= \mathbf{n} \cdot^2 \nabla\nabla\phi \end{aligned} \tag{B.19}$$

$\nabla \cdot \nabla\phi = 0$, thus

$$\frac{\partial \nabla_s\phi}{\partial n} = \mathbf{n} \cdot^2 \nabla\nabla_s\phi - \mathbf{n}\nabla_s \cdot \nabla\phi \tag{B.20}$$

The second derivatives can be obtained through the following relation:

$$\nabla\nabla\phi = \nabla_s\nabla_s\phi + \mathbf{n} \cdot^2 \nabla\nabla_s\phi - \mathbf{n}\nabla_s \cdot \nabla\phi. \tag{B.21}$$

Appendix C

A Higher-Order Correction of FNV Theory

The first-order incident wave for an infinite depth fluid can be defined in cylindrical coordinates by MacCamy & Fuchs (Mei [29]),

$$\Phi_I = Re\{\frac{gA}{\omega}e^{(Kz+i\omega t)}\sum_{m=0}^{\infty}\epsilon_m i^{-m}\cos m\theta J_m(Kr)\} \tag{C.1}$$

For the infinitely deep cylinder, the linearized scattering potential can be written as

$$\Phi_s = -Re\{\frac{gA}{\omega}e^{(Kz+i\omega t)}\sum_{m=0}^{\infty}\epsilon_m i^{-m}\cos m\theta H_m^{(2)}(Kr)\frac{J_m'(Ka)}{H_m^{(2)'}(Ka)}\} \tag{C.2}$$

As discussed in Chapter 5, for the second-harmonic potential, only the component of the second-harmonic pressure with $\cos\theta$ dependence contributes to the second-harmonic horizontal force. Therefore, in the following analysis, we include the terms only with $\cos\theta$ components in $\nabla\Phi_I \cdot \nabla\Phi_s$. We neglect the terms with $m > 1$, since those terms are of higher-order with respect to Kr. Keeping the $m = 0, 1$ terms in the Φ_I and Φ_s expressions, we use the notation

$$\Phi_I^h = Re\{\frac{gA}{\omega}e^{(Kz+i\omega t)}(J_0(Kr) - 2i\cos\theta J_1(Kr))\}, \tag{C.3}$$

and

$$\Phi_s^h = -Re\{\frac{gA}{\omega}e^{(Kz+i\omega t)}[H_0^{(2)}(Kr)\frac{J_0'(Ka)}{H_0^{(2)'}(Ka)} -2i\cos\theta H_1^{(2)}(Kr)\frac{J_1'(Ka)}{H_1^{(2)'}(Ka)}]\}. \quad (C.4)$$

In the long-wave regime, $Ka << 1$, the leading order approximation of (C.4) is

$$\Phi_s^h \simeq Re\{\frac{gA}{\omega}(\frac{i\pi}{4})(Ka)^2e^{(Kz+i\omega t)}(H_0^{(2)}(Kr)+2i\cos\theta H_1^{(2)}(Kr))\}. \quad (C.5)$$

To simplify the analysis, by excluding the time dependence and constant amplitude in (C.3) and (C.5), define

$$\phi_I^h = e^{Kz}[J_0(Kr)-2i\cos\theta J_1(Kr)], \quad (C.6)$$

$$\phi_s^h = e^{Kz}[H_0^{(2)}(Kr)+2i\cos\theta H_1^{(2)}(Kr)]). \quad (C.7)$$

The gradients of ϕ_I^h, ϕ_s^h are

$$\nabla\phi_I^h = e^{Kz}\{J_0'(Kr)-2i\cos\theta J_1'(Kr), 2i\sin\theta\frac{J_1(Kr)}{r}, K[J_0(Kr)-2i\cos\theta J_1(Kr)]\}, \quad (C.8)$$

$$\nabla\phi_s^h = e^{Kz}\{H_0^{'(2)}(Kr)+2i\cos\theta H_1^{'(2)}(Kr), 2i\sin\theta\frac{H_1^{(2)}(Kr)}{r}, K[H_0^{(2)}(Kr)+2i\cos\theta H_1^{(2)}(Kr)]\}. \quad (C.9)$$

Collecting the component with $\cos\theta$ dependence in $\nabla\phi_I^h\cdot\nabla\phi_s^h$ and defining it to be f^h, we have

$$f^h = 2i\cos\theta e^{2Kz}\{J_0'(Kr)H_1^{'(2)}(Kr)-J_1'(Kr)H_0^{'(2)}(Kr) +K^2[J_0(Kr)H_1^{(2)}(Kr)-J_1(Kr)H_0^{(2)}(Kr)]\}. \quad (C.10)$$

Using Wronskions relation [1],

$$W(J_n(Kr), Y_n(Kr)) = J_{n+1}(Kr)Y_n(Kr) - J_n(Kr)Y_{n+1}(Kr) = \frac{2}{\pi Kr}, \qquad \text{(C.11)}$$

f^h can be rewritten as

$$f^h \simeq 2i\cos\theta e^{2Kz}\frac{4i}{\pi}\frac{K}{r} + O(\epsilon) = -\frac{8}{\pi}\frac{K}{r}\cos\theta e^{2Kz} + O(\epsilon). \qquad \text{(C.12)}$$

Let the leading-order of $\partial(\nabla\Phi_I^h \cdot \nabla\Phi_s^h)/\partial t$ with $\cos\theta$ dependence to be F^h, then

$$\begin{aligned} F^h\cos 2\omega t &\simeq -2i\omega(\frac{gA}{\omega})^2(\frac{i\pi}{4})(Ka)^2\frac{8}{\pi}\frac{K}{r}\cos\theta e^{2Kz}\cos 2\omega t \\ &= 4\omega^3A^2e^{2Kz}(Ka)\frac{a}{r}\cos\theta\cos 2\omega t. \end{aligned} \qquad \text{(C.13)}$$

In FNV, the leading order expansions for the forcing function in the inner domain are

$$\omega^3A^2e^{2Kz}\sin 2\omega t(\frac{2a^2}{r^2}\cos 2\theta - \frac{a^4}{r^4}),$$

and

$$-2\omega^3A^3e^{2Kz}\sin^3\omega t(\frac{a^2}{r^3}\cos 3\theta - 2\frac{a^4}{r^5}\cos\theta + \frac{a^6}{r^7}\cos\theta).$$

Compared to the above two terms, the right-hand side of equation (C.13) has an extra (Ka) component in the expression. Ka is a small parameter in the long-wave approximation assumption, therefore, F^h is one order smaller than the above two terms. Since F^h decays as $1/r$, and is one order smaller than the leading-order terms in the forcing function, the forcing fucntion term F^h in equation (C.13) is neglected in the asymptotic analysis of FNV.

However, the contribution from (C.13) is important in the numerical calculation, and also the far-field contribution from this term can not be neglected as illustrated in the following. To solve the integral equation (3.23), the forcing function is integrated

over the free surface. In the long-wave approximation theory, the forcing function is significant in the inner domain, so the free surface integration is truncated at a circle with radius b away from the body. The contribution from (C.13) to the right-hand side of (3.23) can be written as $\iint_{S_Z} F^h G dS = \int d\theta \int F^h G r dr$. Since $F^h \propto 1/r$ and $G \propto 2/r$, the integration over the radial distance can be approximated as

$$\begin{aligned} \int_a^\infty F^h G r dr &\propto \int_a^\infty F^h \frac{2}{r} r dr = \int_a^\infty 2F^h dr \\ &= \int_a^b 2F^h dr + \int_b^\infty 2F^h dr. \end{aligned} \tag{C.14}$$

If we only truncate the free surface at $r = b$, and neglect the far-field contribution, the integration in the inner domain is proportional to $(\log b - \log a)$, and the solution changes as the truncation radius b changes. On the other hand, the expansion for F^h is the same in the inner domain and the outer domain. Thus, for the last line in equation (C.14), the upper limit of the integral in the second term cancels out the lower limit of the integral in the first term. The logarithmic singularity disappears when the far field is included in the numerical analysis. Though this whole analysis is for the infinitely deep cylinder, the results can be applied to a truncated cylidner case with large draft.

Considering all components in (C.1) and (C.2), Newman [38] finds that for the second-order forcing function of the infinitely deep cylinder, the dominant component in the far field is also inversely proportional to the radial coordinate. The second-order potential is derived directly by a Weber transformation of the corresponding forcing function on the free surface in [38].

Bibliography

[1] Abramowitz, M. and Stegun, I. A., 1964, "Handbook of mathematical functions with formulas, graphs, and mathematical tables." US Government Printing Office and Dover.

[2] Bingham, H. B. and Maniar, H., 1996, "Calculating the double body m–terms with a higher order B–spline based panel method", $11th$ International Workshop on Water Waves and Floating Bodies, Hamburg, Germany.

[3] Brand, L., 1947, "Vector and tensor analysis," John Wiley & Sons Inc., New York.

[4] Chau, F. P. and Eatock Taylor, R., 1992, "Second-order wave diffraction by a vertical cylinder." *J. of Fluid Mech.* **242**, 571-599.

[5] Cummins, W. E., 1962, "The impulse response function and ship motions." Schiffstechnik, **9**, 101-109

[6] Eckhoff, K., 1996, "Ringing simulations of a three column TLP", thesis. prepared at MIT for siv.ing degree from NUST, Trondheim, Norway.

[7] Emmerhoff, O. J. and Sclavounos, P. D., 1992, "The slow drift motion of arrays of vertical cylinders." *J. Fluid Mech.*, **242**, 31

[8] Jefferys, E. R. and Rainey, R. C. T., 1994, "Slender body models of TLP and GBS ringing." BOSS, MIT, Cambridge.

[9] Grue, J. , Bjorshol, G., and Strand, O., 1994, "Nonlinear wave loads which may generate 'ringing' responses of offshore structures." $10th$ Int. Workshop on Water Waves and Floating Bodies, Kuju, Japan.

[10] Grue, J. and Palm E., 1993, "The mean drift force and yaw moment on marine structures in waves and current." *J. Fluid Mech.*, **250**, 121-142.

[11] Faltinsen, O. M, 1990, "Sea loads on ship and offshore structures." Cambridge University Press.

[12] Faltinsen, O. M., Newman, J. N. and Vinje, T., 1995,"Nonlinear wave loads on a slender vertical cylinder." *J. Fluid Mech.*, **289**, 179-198

[13] Ferrant, P., 1996, "Simulation of strongly nonlinear wave generation and wave-body interactions using a 3D MEL model." $21th$ Symposium on Naval Hydrodynamics, Trondheim, Norway.

[14] Hess, J. L. and Smith, A. M. O., 1964, "Calculation of nonlifting potential flow about arbitrary three-dimensional bodies." *J. Ship Research*, **8**, 22-44.

[15] Hildebrand, F. B., "Advanced calculus for applications." Prentice-Hall, Inc. 1976.

[16] Hsin, C.-Y., Kerwin, J. E. and Newman J. N., 1992, "A higher-order panel method based on B-splines", $6th$ International Conference on Numerical Ship Hydrodynamics, Iowa City, Iowa.

[17] Kim, M.-H. and Yue, D. K. P., 1989, "The complete second-order diffraction solution for an axisymmetric body. Part 1, Monochromatic incident waves." *J. Fluid Mech.*, **200**, 235-264.

[18] Kim, M.-H. and Yue, D. K. P., 1990, "The complete second-order diffraction solution for an axisymmetric body. Part 2, Bichromatic incident waves and body motions." *J. Fluid Mech.*, **211**, 557-593.

[19] Korsmeyer, F. T., Lee, C.-H., Newman, J. N. and Sclavounos, P.D., 1988, "The analysis of wave effects on tension-leg platforms." OMAE, Houston.

[20] Krokstad J. R., Stansberg C. T., Nestegard A. and Marthinsen T., 1996, "A new non-slender ringing load approach verified against experiments." OMAE, Florence, Italy.

[21] Molin, B., 1979, "Second order diffraction loads upon three dimensional bodies." *Applied Ocean Reseach,* **1**, 197-202.

[22] Lee, C.-H., 1995, "WAMIT theory manual." Department of Ocean Engineering, Massachusetts Institute of Technology.

[23] Lee, C.-H., Newman, J. N., Kim, M.-H., and Yue, D. K. P., 1991, "The computation of second-order wave loads." OMAE, Offshore Technology.

[24] Lee, C.-H. and Zhu, X., 1993, "Second-order diffraction and radiation solutions on floating bodies." $8th$ International Workshop on Water Waves and Floating Bodies, Newfoundland, Canada.

[25] Lee, C.-H., Maniar, H., Newman, J. N., Zhu, X., 1996, "Computations of wave loads using a B-spline panel method." $21th$ Symposium on Naval Hydrodynamics, Trondheim, Norway.

[26] Malenica, S. and Molin, B., 1995, "Third order wave diffraction by a vertical cylinder." *J. Fluid Mech.*, **302**, 203-229.

[27] Maniar, H., 1995, "A three dimensional higher order panel method based on B-splines." Ph.D. thesis, Department of Ocean Engineering, Massachusetts Institute of Technology.

[28] Molin, B. and Chen X. B., 1990, "Calculation of second order sum frequency loads on TLP hulls." Internal report, Institut Francais du Petrole.

[29] Mei, C.C., 1883, "The applied dynamics of ocean waves," Wiley.

[30] Newman, J. N., 1977, "Marine hydrodynamics." The MIT Press.

[31] Newman, J. N., 1985, "Algorithms for the free surface Green function." *J. Eng. Math.*, **19**, 57-67.

[32] Newman, J. N., 1986, "Distributions of sources and normal dipoles over a quadrilateral panel." *J. Eng. Math.*, **20**, 113-126.

[33] Newman, J. N. and Sclavounos, P. D., 1988, "The computational wave loads on large offshore structures." BOSS, Trondheim, Norway.

[34] Newman, J. N., 1990, "Second-harmonic wave diffraction at large depths." *J. Fluid Mech.*, **213**, 59-70.

[35] Newman, J. N. and Lee, C.-H., 1992, "Sensitivity of wave loads to the discretization of bodies." BOSS, London, UK.

[36] Newman, J. N., 1993, "Wave-drift damping of floating bodies." *J. Fluid Mech.*, **249**, 241-259.

[37] Newman, J. N., 1994, "Nonlinear scattering of long waves by a vertical cylinder." Symposium on Waves and Nonlinear Processes in Hydrodynamics, Oslo, Norway.

[38] Newman, J. N., 1996, "The second-order wave force on a vertical cylinder." *J. Fluid Mech.*, **320**, 417-443.

[39] Ogilvie, T. F., 1964, "Recent progress toward the understanding and prediction of ship motions." 5th Symposium on naval hydrodynamics, 3-128. Washington, D.C.

[40] Ogilvie, T. F., 1983, "Second-order hydrodynamic effects on ocean platforms." International Workshop on Ship and Platform Motions, Berkeley.

[41] Reiney, R. C. T., 1989, "A new equation for wave loads on offshore structures." *J. Fluid Mech.* **204**, 295-324.

[42] Sclavounos, P. D. and Kim Y.-H. "Third-order diffraction of surface waves by a time-domain rankine panel method." $10th$ International Workshop on Water Waves and Floating Bodies, Oxford, UK.

[43] Stansberg, C. T., Huse, E., Krokstad, J. R., and Lehn, E., 1995, "Experimental study of non-linear loads on vertical cylinders in steep random waves." ISOPE, the Hague, the Netherlands.

[44] Wehausen, J. V. and Laitone, E. V, 1960, "Surface Waves." Handbuch der Physik, pp 446-778, Springer.

[45] Zhao, R. and Faltinsen, O., 1989, "A discussion of the m_j-terms in the wave-current body interaction problem." 4th International Workshop on Water Waves and Floating Body, Øystese.

[46] Zhu, X., 1994, "Irregular frequency removal from the boundary integral equation for the wave-body problem." M.S. thesis, Department of Ocean Engineering, Massachusetts Institute of Technology.